

Multimaterial topology optimization for finite strain elastoplasticity: theory, methods, and applications

Yingqi Jia^a, Xiaojia Shelly Zhang^{a,b,c,*}

^aDepartment of Civil and Environmental Engineering, University of Illinois Urbana-Champaign, Urbana, IL 61801, USA

^bDepartment of Mechanical Science and Engineering, University of Illinois Urbana-Champaign, Urbana, IL 61801, USA

^cNational Center for Supercomputing Applications, Urbana, IL 61801, USA

Abstract

Plasticity is inherent to many engineering materials such as metals. While it can degrade the load-carrying capacity of structures via material yielding, it can also protect structures through plastic energy dissipation. To fully harness plasticity, here we present the theory, method, and application of a topology optimization framework that simultaneously optimizes structural geometries and material phases to customize the stiffness, strength, and structural toughness of designs experiencing finite strain elastoplasticity. The framework accurately predicts structural responses by employing a rigorous, mechanics-based elastoplasticity theory that ensures isochoric plastic flow. It also effectively identifies optimal material phase distributions using a gradient-based optimizer, where gradient information is obtained via a reversed adjoint method to address history dependence, along with automatic differentiation to compute the complex partial derivatives. We demonstrate the framework's capabilities by optimizing a range of 2D and 3D multimaterial elastoplastic structures with real-world applications, including energy-dissipating dampers, load-carrying beams, impact-resisting bumpers, and cold working profiled sheets. These optimized multimaterial structures reveal important mechanisms for improving design performance under large deformation, such as the transition from kinematic to isotropic hardening with increasing displacement amplitudes and the formation of twisted regions that concentrate stress, enhancing plastic energy dissipation. Through the superior performance of these optimized designs, we demonstrate the framework's effectiveness in tailoring elastoplastic responses across various spatial configurations, material types, hardening behaviors, and combinations of candidate materials. This work offers a systematic approach for optimizing next-generation multimaterial structures with elastoplastic behaviors under large deformations.

Keywords: Plasticity; Finite strain; Isochoric plastic flow; Topology optimization; Multimaterial; Energy dissipation

1. Introduction

Plasticity is a fundamental physical phenomenon describing the permanent deformation of solids (Chaboche, 2008) — a trait that transcends elasticity and is inherent to critical materials such as metals, woods, foams, and soils. These materials form the backbone of engineering structures. The irreversible nature of plasticity holds two faces: it can cause undesirable deformations and a loss of structural load-carrying capacity or enable the formation of desired geometries and the dissipation of energy. In addition, plasticity is an inherently complex behavior, involving history-dependent stress-strain responses, material hardening, and large deformations that interact across multiple scales. Thus, there is a need for innovative methods to design and control plasticity at will.

To harness material plasticity, topology optimization (Bendsøe and Kikuchi, 1988; Bendsoe and Sigmund, 2003; Wang et al., 2021) as a form of computational morphogenesis offers great promise. This approach strategically distributes limited materials to optimize structural responses under given constraints.

*Corresponding author.

Therefore, it is naturally suited for controlling mechanical responses such as displacement fields (Jia et al., 2024b,c), stress distributions (Jia et al., 2024a), and fracture nucleation and propagation (Jia et al., 2023).

In light of its potential for controlling mechanical responses, topology optimization has recently achieved notable progress in tailoring plastic behaviors under the assumption of infinitesimal strains. For instance, employing a single material type with restricted usage, researchers have shown success in limiting plastic yielding (Amir, 2017; Zhang et al., 2023; Li et al., 2024), maximizing end compliance/force (Boissier et al., 2021; Desai et al., 2021), and maximizing energy (Maute et al., 1998; Zhang et al., 2017; Li et al., 2017b,a; Li and Khandelwal, 2017; Alberdi and Khandelwal, 2017, 2019b). Furthermore, studies have explored maximizing both compliance and energy (Abueidda et al., 2021) and fitting target stress–strain responses (Kim and Yun, 2020). Beyond single-material strategies, Nakshatrala and Tortorelli (2015) minimized energy propagation by filling distinct materials into fixed geometries, while Li et al. (2021) optimized end force in similar setups.

Despite these significant advances in controlling structural plasticity under small deformations, optimizing finite strain plastic responses remains in its infancy. Only a few pioneering studies have tackled this challenge in the past decade. For example, Wallin et al. (2016) and Ivarsson et al. (2018, 2020) focused on optimizing structural geometries to improve system energy by specifying a single candidate material. Similarly, Ivarsson et al. (2021) maximized compliance while constraining plastic work through single-material topology optimization. In addition, Alberdi and Khandelwal (2019a) employed two candidate materials in fixed geometries to maximize plastic work. More recently, Han et al. (2024) separately optimized structural geometries and material phases in different design cases to enhance stiffness and plastic hardening.

A review of past efforts highlights a key limitation: most studies either optimize structural geometries while fixing material types or optimize material phases while fixing structural geometries. To fully leverage topology optimization’s potential and further improve structural performance, simultaneous optimization of structural geometries and material phases is desired. Such an approach would enable the creation of free-form, multimaterial structures with optimized plastic responses. Recently, Jia et al. (2025) pursued this goal and demonstrated preliminary success for infinitesimal strain plasticity; however, simultaneous optimization for finite strain plasticity remains under-explored.

In this study, we propose a multimaterial topology optimization framework for finite strain elastoplasticity. As illustrated in Fig. 1(a), our goal is to *concurrently* optimize structural geometries and material phases to maximize stiffness, strength (end force), and total energy (effective structural toughness) of structures undergoing finite strain plasticity. To achieve this goal, we present a multimaterial optimization approach in Fig. 1(b), which addresses two major challenges — accurate prediction of finite strain elastoplastic responses and path-dependent sensitivity analysis. To precisely predict plastic behaviors, we adopt a rigorous mechanics-based elastoplasticity theory from Simo (1988a,b), which accounts for large deformations. We further adapt it to enforce isochoric plastic flow, accommodating a wide range of plastic materials including metals. To handle the path-dependent sensitivity analysis necessary for updating design variables, we employ the reversed adjoint method (Alberdi et al., 2018; Jia et al., 2025) to address history dependency and leverage automatic differentiation to effortlessly compute the required partial derivatives. By resolving these challenges, the framework establishes a closed-loop process that enables the creation of freeform, multimaterial optimized elastoplastic structures.

Based on the proposed framework, we optimize a spectrum of representative multimaterial elastoplastic structures with real-world applications (Fig. 1(c)) and uncover the mechanisms behind their optimized behaviors. For example, we design two-dimensional (2D) metallic yielding dampers with maximized energy dissipation for vibration mitigation under cyclic loadings, revealing a shift in dominance from kinematic to isotropic hardening as displacement amplitudes increase. We also explore the synergistic use of hyperelastic and elastoplastic materials to achieve various stiffness–strength balances in load-carrying beams. Extending the design to three dimensions (3D), we maximize the crashworthiness of impact-resisting bumpers, uncovering the formation of X-shaped structures in the middle to shorten the load path and enhance elastic energy absorption, as well as twisted regions aside to concentrate stress and increase plastic energy dissipation. Finally, we present optimized cold working profiled sheets undergoing ultra-large plastic deformations, demonstrating the simultaneous optimization of metal-forming and load-carrying stages while incorporating

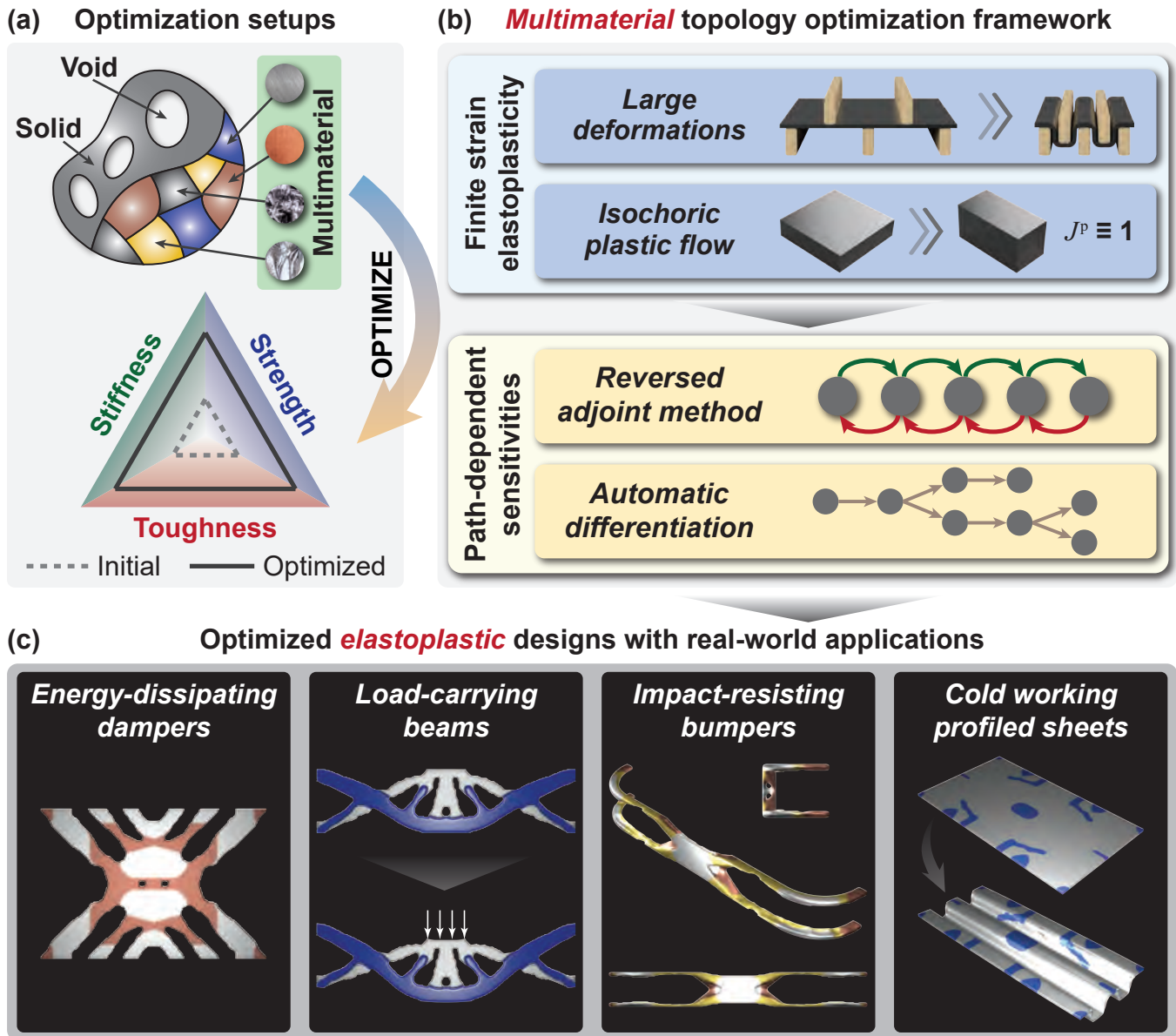


Figure 1: Multimaterial and multiobjective topology optimization for finite strain elastoplasticity. (a) Optimization setups. (b) Multimaterial topology optimization framework. The variable J^p is the determinant of the plastic part of the deformation gradient. (c) Optimized elastoplastic designs with real-world applications.

practical constraints such as cost, lightweight, and sustainability (Kundu and Zhang, 2025).

The optimized designs showcase the effectiveness of the proposed framework in freely controlling elastoplastic responses under large deformations in 2D and 3D, across different material types (elastic/plastic/mixed), various hardening behaviors (perfect/isotropic/kinematic/combined and linear/nonlinear), and arbitrary numbers of candidate materials (single-material/bi-material/multimaterial). Ultimately, the framework can provide a systematic tool for designing the next generation of multimaterial elastoplastic structures.

The remaining parts of this study are organized as follows. Section 2 recaps the finite strain elastoplasticity theory presented in Simo (1988a,b), with additional emphasis on enforcing isochoric plastic flow. Building on this theory, Section 3 introduces the proposed multimaterial topology optimization framework for tailoring structural elastoplastic responses. To demonstrate the framework’s effectiveness, Section 4 presents a broad spectrum of optimized elastoplastic designs with real-world applications. Finally, Section 5 provides concluding remarks.

This study is further supplemented by six appendices. Appendix A derives the proposed updating formulae for the internal variable to ensure isochoric plastic flow. Appendix B presents the derivation of the second elastoplastic moduli, a key component of the elastoplasticity theory for a quadratic convergence rate. Appendix C verifies the accuracy of the theory and implementation by comparing it to analytical solutions. Appendix D investigates the convergence, precision, and computational time of the finite element analysis (FEA). Appendix E details the derivation and verification of the path-dependent sensitivity analysis. Finally, Appendix F examines the consistency of elastoplastic responses across various mesh and finite element combinations for the optimized designs.

2. Finite strain elastoplasticity: theory and implementation

In this section, we provide a recap of the finite strain elastoplasticity theory from Simo (1988a,b) and outline its numerical implementation. We begin with an overview of the fundamentals of finite strain deformation and strain tensors, followed by a presentation of the local governing equations. Lastly, we introduce the global governing equations for finite strain elastoplasticity. The detailed explanations are presented below.

2.1. Prerequisites: finite strain deformation and strain tensors

We consider an open bounded domain ($\Omega_0 \subset \mathbb{R}^3$) occupied by a piece of undeformed material. For any material point $\mathbf{X} \in \Omega_0$, we define its displacement field as $\mathbf{u}(\mathbf{X})$ and the total deformation gradient as $\mathbf{F}(\mathbf{X}) = \mathbf{I} + \nabla \mathbf{u}(\mathbf{X})$. We also define the left and right Cauchy–Green deformation tensors as

$$\mathbf{b}(\mathbf{X}) = \mathbf{F}(\mathbf{X})\mathbf{F}^\top(\mathbf{X}) \quad \text{and} \quad \mathbf{C}(\mathbf{X}) = \mathbf{F}^\top(\mathbf{X})\mathbf{F}(\mathbf{X}),$$

respectively. Additionally, we define the Lagrangian strain tensor as

$$\mathbf{E}(\mathbf{X}) = \frac{1}{2}(\mathbf{C} - \mathbf{I}). \tag{1}$$

Based on the multiplicative decomposition, the total deformation gradient can be split as

$$\mathbf{F}(\mathbf{X}) = \mathbf{F}^e(\mathbf{X})\mathbf{F}^p(\mathbf{X})$$

where $\mathbf{F}^e(\mathbf{X})$ and $\mathbf{F}^p(\mathbf{X})$ are the elastic and plastic parts of $\mathbf{F}(\mathbf{X})$, respectively, with \mathbf{F}^p corresponding to stress-free plastic deformation. For later use, we further define the elastic part of $\mathbf{b}(\mathbf{X})$ as

$$\mathbf{b}^e(\mathbf{X}) = \mathbf{F}^e(\mathbf{X})\mathbf{F}^{e\top}(\mathbf{X}) \tag{2}$$

and the plastic part of $\mathbf{C}(\mathbf{X})$ as

$$\mathbf{C}^p(\mathbf{X}) = \mathbf{F}^{p\top}(\mathbf{X})\mathbf{F}^p(\mathbf{X}). \tag{3}$$

The relationships among these deformation tensors are illustrated in Fig. 2. At load step n , the undeformed configuration (Ω_0) is mapped to the intermediate configuration (Ξ_n) through plastic deformation (\mathbf{F}_n^p or \mathbf{C}_n^p), and further to the deformed configuration (Ω_n) via elastic deformation (\mathbf{F}_n^e or \mathbf{b}_n^e). Alternatively, Ω_0 can be directly mapped to Ω_n through the total deformation (\mathbf{F}_n). Similarly, at the next load step $n+1$, Ω_0 maps to the intermediate configuration (Ξ_{n+1}) through \mathbf{F}_{n+1}^p or \mathbf{C}_{n+1}^p , and subsequently to the deformed configuration (Ω_{n+1}) via \mathbf{F}_{n+1}^e or \mathbf{b}_{n+1}^e . Note that Ω_0 can also directly map to Ω_{n+1} through \mathbf{F}_{n+1} . Additionally, Ω_n can be mapped to Ω_{n+1} using the relative deformation gradient expressed as

$$\mathbf{f}_{n+1} = \mathbf{F}_{n+1} \mathbf{F}_n^{-1}.$$

Finally, for later use, we define the volume-preserving parts of these deformation and strain tensors as

$$\bar{\mathbf{F}} = J^{-1/3} \mathbf{F}, \quad \bar{\mathbf{b}}^e = (J^e)^{-2/3} \mathbf{b}^e, \quad \text{and} \quad \bar{\mathbf{f}} = J_f^{-1/3} \mathbf{f},$$

and express the determinants as

$$J = \det(\mathbf{F}), \quad J^e = \det(\mathbf{F}^e), \quad J^p = \det(\mathbf{F}^p), \quad \text{and} \quad J_f = \det(\mathbf{f}).$$

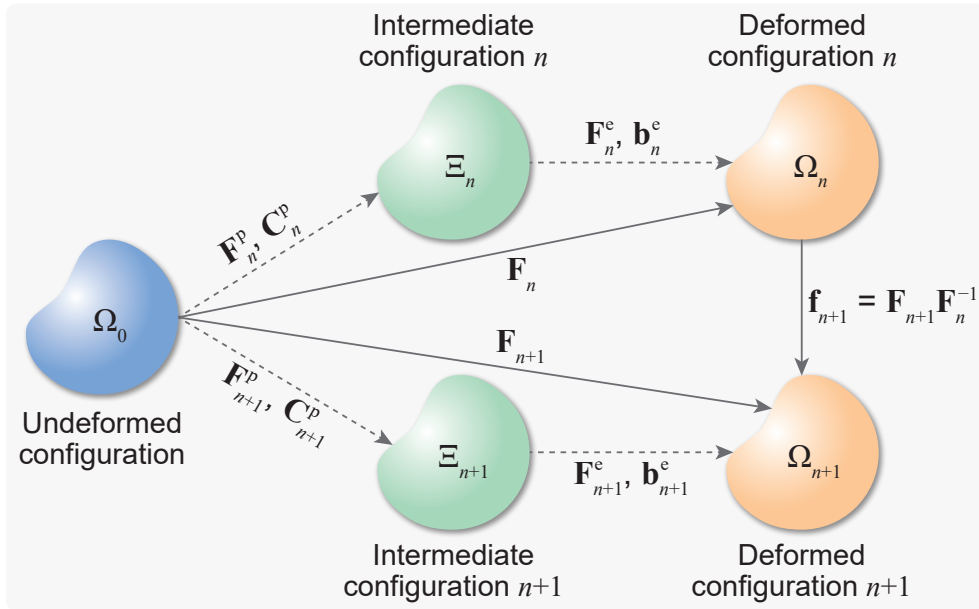


Figure 2: Relationships among the deformation tensors used in the finite strain elastoplasticity theory.

2.2. Local governing equations for finite strain elastoplasticity

In this subsection, we introduce the local governing equations for finite strain elastoplasticity, including the constitutive relationships, flow rules, hardening laws, and yield conditions. Combining these principles, we conclude with the radial return mapping scheme, which is employed to determine the elastoplastic response of a material point.

2.2.1. Constitutive relationships

We consider a hyperelastic material with a strain energy density function expressed as

$$W(J^e, \bar{\mathbf{b}}^e) = U(J^e) + \bar{W}(\bar{\mathbf{b}}^e), \quad (4)$$

which is characterized by separable volumetric (U) and deviatoric (\bar{W}) parts. One classical choice of such function reads as (Simo and Hughes, 2006)

$$U(J^e) = \frac{\kappa}{2} \left\{ \frac{1}{2} [(J^e)^2 - 1] - \ln J^e \right\} \quad \text{and} \quad \bar{W}(\bar{\mathbf{b}}^e) = \frac{\mu}{2} [\text{tr}(\bar{\mathbf{b}}^e) - 3], \quad (5)$$

where μ and κ are the initial shear and bulk moduli, respectively. Based on the strain energy density function in (4), we derive the Kirchhoff stress tensor as

$$\hat{\boldsymbol{\tau}} = \frac{\partial W}{\partial \mathbf{F}^e} \mathbf{F}^{e\top} = \boldsymbol{\tau}^{\text{vol}} + \hat{\mathbf{s}} = J^e U'(J^e) \mathbf{I} + \mu \operatorname{dev}(\bar{\mathbf{b}}^e), \quad (6)$$

where we separate $\hat{\boldsymbol{\tau}}$ into the volumetric ($\boldsymbol{\tau}^{\text{vol}} = J^e U'(J^e) \mathbf{I}$) and deviatoric ($\hat{\mathbf{s}} = \mu \operatorname{dev}(\bar{\mathbf{b}}^e)$) parts. Finally, we define the net stress tensor as

$$\boldsymbol{\xi} = \hat{\mathbf{s}} - \operatorname{dev}(\bar{\boldsymbol{\beta}}) \quad \text{with} \quad \bar{\boldsymbol{\beta}} = J^{-2/3} \boldsymbol{\beta}$$

where $\boldsymbol{\beta}$ is the back stress tensor triggered by the kinematic hardening of materials.

2.2.2. Flow rules and kinematic hardening laws

After defining the deformation and strain tensors as well as the constitutive relationships, we proceed with the flow rules and hardening laws. In the context of the finite strain elastoplasticity (Simo, 1988a,b), we present the flow rules as

$$\mu J^{-2/3} \operatorname{dev}(\mathcal{L}_v \mathbf{b}^e) = -2\bar{\bar{\mu}} \gamma \mathbf{n} \quad \text{and} \quad \operatorname{tr}(\mathcal{L}_v \mathbf{b}^e) = 0, \quad (7)$$

and Prager–Ziegler-type kinematic hardening laws as

$$\mu J^{-2/3} \operatorname{dev}(\mathcal{L}_v \boldsymbol{\beta}) = \frac{2}{3} h \bar{\bar{\mu}} \gamma \mathbf{n} \quad \text{and} \quad \operatorname{tr}(\mathcal{L}_v \boldsymbol{\beta}) = 0. \quad (8)$$

Here, h is the kinematic hardening modulus of materials, and $\gamma \geq 0$ is a consistency parameter that will be determined later. The variable \mathbf{n} is a unit tensor defined as $\mathbf{n} = \boldsymbol{\xi} / \|\boldsymbol{\xi}\|$ where $\|\boldsymbol{\xi}\| = \sqrt{\boldsymbol{\xi} : \boldsymbol{\xi}}$. The parameter $\bar{\bar{\mu}}$ is defined as

$$\bar{\bar{\mu}} = \bar{\mu} - \frac{1}{3} \operatorname{tr}(\bar{\boldsymbol{\beta}}) \quad \text{with} \quad \bar{\mu} = \frac{\mu}{3} J^{-2/3} \operatorname{tr}(\mathbf{b}^e).$$

Additionally, the operator \mathcal{L}_v in (7)–(8) is the Lie time derivative defined as

$$\mathcal{L}_v \mathbf{T} = \varphi_* \left[\frac{\partial}{\partial t} \varphi^*(\mathbf{T}) \right]$$

for a dummy tensor \mathbf{T} where t represents the time. The symbols φ^* and φ_* are the pull-back and push-forward operators expressed as

$$\varphi^*(\mathbf{T}) = \mathbf{F}^{-1} \mathbf{T} \mathbf{F}^{-\top} \quad \text{and} \quad \varphi_*(\mathbf{T}) = \mathbf{F} \mathbf{T} \mathbf{F}^\top,$$

respectively.

2.2.3. Yield criterion and isotropic hardening laws

To account for the yielding of materials, we adopt the classical von Mises yield criterion defined as

$$f(\boldsymbol{\xi}, \alpha) = \|\boldsymbol{\xi}\| - \sqrt{\frac{2}{3}} k(\alpha) \leq 0 \quad (9)$$

where $f(\boldsymbol{\xi}, \alpha) < 0$ represents that the material deforms elastically, and $f(\boldsymbol{\xi}, \alpha) = 0$ denotes the onset of yielding. To enforce the yield criterion of $f(\boldsymbol{\xi}, \alpha) \leq 0$, we apply the Kuhn–Tucker conditions expressed as

$$\gamma \geq 0 \quad \text{and} \quad \gamma f(\boldsymbol{\xi}, \alpha) = 0. \quad (10)$$

In the above equations, the non-decreasing variable α is the equivalent plastic strain, whose evolution is governed by (Simo, 1988a,b)

$$\frac{\partial \alpha}{\partial t} = \sqrt{\frac{2}{3}} \gamma. \quad (11)$$

The function $k(\alpha)$ in (9) determines the radius of the yield surface and characterizes the isotropic hardening of materials, which can follow either a linear or nonlinear form. For linear isotropic hardening, we set

$$k(\alpha) = \sigma_y + K\alpha \quad (12)$$

where σ_y is the initial yield strength of the material, and K is the isotropic hardening modulus. For nonlinear isotropic hardening, we adopt a classical expression as (Simo, 1988b)

$$k(\alpha) = \sigma_y + K\alpha + (\sigma_\infty - \sigma_y)(1 - e^{-\delta\alpha}) \quad (13)$$

where σ_∞ is the residual yield strength, and $\delta > 0$ is a saturation exponent.

2.2.4. Radial return mapping scheme

In previous discussions, we have established the constitutive relationship in (6), flow rules in (7), kinematic hardening laws in (8), yield criterion in (9), Kuhn–Tucker conditions in (10), the evolution of the equivalent plastic strain in (11), and isotropic hardening laws in (12)–(13). A collection of these requirements fully governs the finite strain elastoplastic responses of any material point $\mathbf{X} \in \Omega_0$. To reconcile these governing equations and solve for the material elastoplastic responses, we adopt a canonical radial return mapping scheme (Wilkins et al., 1969; Krieg and Krieg, 1977) as follows.

Applying a backward Euler difference scheme to the above local governing equations, we derive their time-discretized versions as

$$\left\{ \begin{array}{l} \bar{\mathbf{b}}_{n+1}^e = \bar{\mathbf{f}}_{n+1} \bar{\mathbf{b}}_n^e \bar{\mathbf{f}}_{n+1}^\top - \frac{2\bar{\mu}_{n+1}}{\mu} \hat{\gamma}_{n+1} \mathbf{n}_{n+1}, \quad \bar{\boldsymbol{\beta}}_{n+1} = \bar{\mathbf{f}}_{n+1} \bar{\boldsymbol{\beta}}_n \bar{\mathbf{f}}_{n+1}^\top + \frac{2h\bar{\mu}_{n+1}}{3\mu} \hat{\gamma}_{n+1} \mathbf{n}_{n+1}, \\ \alpha_{n+1} = \alpha_n + \sqrt{\frac{2}{3}} \hat{\gamma}_{n+1}, \quad \hat{\mathbf{s}}_{n+1} = \mu \operatorname{dev}(\bar{\mathbf{b}}_{n+1}^e), \quad \boldsymbol{\xi}_{n+1} = \hat{\mathbf{s}}_{n+1} - \operatorname{dev}(\bar{\boldsymbol{\beta}}_{n+1}), \\ \mathbf{n}_{n+1} = \boldsymbol{\xi}_{n+1} / \|\boldsymbol{\xi}_{n+1}\|, \quad \bar{\mu}_{n+1} = \frac{\mu}{3} \operatorname{tr}(\bar{\mathbf{b}}_{n+1}^e), \quad \bar{\bar{\mu}}_{n+1} = \bar{\mu}_{n+1} - \frac{1}{3} \operatorname{tr}(\bar{\boldsymbol{\beta}}_{n+1}), \\ f_{n+1} = \|\boldsymbol{\xi}_{n+1}\| - \sqrt{\frac{2}{3}} k(\alpha_{n+1}) \leq 0, \quad \hat{\gamma}_{n+1} \geq 0, \quad \hat{\gamma}_{n+1} f_{n+1} = 0. \end{array} \right. \quad (14)$$

In these expressions, we recall that $\mathbf{f}_{n+1} = \mathbf{F}_{n+1} \mathbf{F}_n^{-1}$ is the relative deformation gradient between load steps n and $n+1$, and $\bar{\mathbf{f}}_{n+1} = (J_{n+1}^f)^{-1/3} \mathbf{f}_{n+1}$ is its volume-preserving part with $J_{n+1}^f = \det(\mathbf{f}_{n+1})$. The variable $\hat{\gamma}_{n+1}$ is shorted for $\Delta t \gamma_{n+1}$, and Δt is the time interval.

Remark 1. For the derivation of $\bar{\mathbf{b}}_{n+1}^e$ and $\bar{\mu}_{n+1}$ in (14) and all subsequent analyses, we adopt the assumption of isochoric plastic flow ($J_n^p = J_{n+1}^p = 1$). This assumption is commonly accepted and even required (Weber and Anand, 1990; Simo, 1992; Simo and Miehe, 1992; Wang et al., 2017) for many elastoplastic materials such as metals, and it implies that the volume of the material does not change during plastic deformation.

To solve (14) with given $\bar{\mathbf{b}}_n^e, \bar{\boldsymbol{\beta}}_n, \alpha_n, \mathbf{F}_n$, and \mathbf{F}_{n+1} , we *temporarily* assume no new plastic flow ($\hat{\gamma}_{n+1} = 0$) and define the trial variables as

$$\left\{ \begin{array}{l} \bar{\mathbf{b}}_{n+1}^{e, \text{tr}} = \bar{\mathbf{f}}_{n+1} \bar{\mathbf{b}}_n^e \bar{\mathbf{f}}_{n+1}^\top, \quad \bar{\boldsymbol{\beta}}_{n+1}^{\text{tr}} = \bar{\mathbf{f}}_{n+1} \bar{\boldsymbol{\beta}}_n \bar{\mathbf{f}}_{n+1}^\top, \quad \alpha_{n+1}^{\text{tr}} = \alpha_n, \\ \mathbf{s}_{n+1}^{\text{tr}} = \mu \operatorname{dev}(\bar{\mathbf{b}}_{n+1}^{e, \text{tr}}), \quad \boldsymbol{\xi}_{n+1}^{\text{tr}} = \mathbf{s}_{n+1}^{\text{tr}} - \operatorname{dev}(\bar{\boldsymbol{\beta}}_{n+1}^{\text{tr}}), \quad \mathbf{n}_{n+1}^{\text{tr}} = \boldsymbol{\xi}_{n+1}^{\text{tr}} / \|\boldsymbol{\xi}_{n+1}^{\text{tr}}\|, \\ \bar{\mu}_{n+1}^{\text{tr}} = \frac{\mu}{3} \operatorname{tr}(\bar{\mathbf{b}}_{n+1}^{e, \text{tr}}), \quad \bar{\bar{\mu}}_{n+1}^{\text{tr}} = \bar{\mu}_{n+1}^{\text{tr}} - \frac{1}{3} \operatorname{tr}(\bar{\boldsymbol{\beta}}_{n+1}^{\text{tr}}), \quad f_{n+1}^{\text{tr}} = \|\boldsymbol{\xi}_{n+1}^{\text{tr}}\| - \sqrt{\frac{2}{3}} k(\alpha_{n+1}^{\text{tr}}). \end{array} \right. \quad (15)$$

Next, we correct $\bar{\boldsymbol{\beta}}_{n+1}$ and α_{n+1} with

$$\bar{\boldsymbol{\beta}}_{n+1} = \bar{\boldsymbol{\beta}}_{n+1}^{\text{tr}} + \frac{2h\bar{\mu}_{n+1}^{\text{tr}}}{3\mu} \hat{\gamma}_{n+1} \mathbf{n}_{n+1} \quad \text{and} \quad \alpha_{n+1} = \alpha_{n+1}^{\text{tr}} + \sqrt{\frac{2}{3}} \hat{\gamma}_{n+1} \quad (16)$$

based on (14)_{2,3} and Proposition 1 and correct $\bar{\mathbf{b}}_{n+1}^e$ with

$$\left\{ \begin{array}{l} \bar{\mathbf{b}}_{n+1}^e = \text{dev}(\bar{\mathbf{b}}_{n+1}^e) + \frac{1}{3}\mathcal{I}_1\mathbf{I}, \\ \text{dev}(\bar{\mathbf{b}}_{n+1}^e) = \text{dev}(\bar{\mathbf{b}}_{n+1}^{e,\text{tr}}) - \frac{2\bar{\mu}_{n+1}^{\text{tr}}}{\mu}\hat{\gamma}_{n+1}\mathbf{n}_{n+1}, \\ \mathcal{I}_1 = \begin{cases} \left(-\frac{\mathcal{Q}}{2} + \sqrt{-\Delta}\right)^{1/3} + \left(-\frac{\mathcal{Q}}{2} - \sqrt{-\Delta}\right)^{1/3}, & \text{if } \Delta < 0; \\ \max\left\{\frac{3\mathcal{Q}}{\mathcal{P}}, -\frac{3\mathcal{Q}}{2\mathcal{P}}\right\}, & \text{if } \Delta = 0; \\ \mathcal{S}_1, & \text{if } \Delta > 0, \left(\bar{\mathbf{b}}_{n+1}^e\right)_{11} > 0, \text{ and } \mathcal{B} > 0; \\ \mathcal{S}_2, & \text{otherwise.} \end{cases} \end{array} \right. \quad (17)$$

Here, the related variables are defined as

$$\left\{ \begin{array}{l} \mathcal{P} = -\mathcal{J}_2 \leq 0, \quad \mathcal{Q} = \mathcal{J}_3 - 1, \quad \Delta = -\left(\frac{\mathcal{P}^3}{27} + \frac{\mathcal{Q}^2}{4}\right), \\ \mathcal{J}_2 = \frac{1}{2}\left\|\text{dev}(\bar{\mathbf{b}}_{n+1}^e)\right\|^2, \quad \mathcal{J}_3 = \det\left[\text{dev}(\bar{\mathbf{b}}_{n+1}^e)\right], \\ \mathcal{B} = \left(\bar{\mathbf{b}}_{n+1}^e\right)_{11}\left(\bar{\mathbf{b}}_{n+1}^e\right)_{22} - \left(\bar{\mathbf{b}}_{n+1}^e\right)_{12}\left(\bar{\mathbf{b}}_{n+1}^e\right)_{21}. \end{array} \right.$$

Additionally, we define \mathcal{S}_1 and \mathcal{S}_2 as the largest and second to largest values among r_1 , r_2 , and r_3 with r_k defined as

$$r_k = 2\sqrt{-\frac{\mathcal{P}}{3}}\cos\left[\frac{1}{3}\arccos\left(\frac{3\mathcal{Q}}{2\mathcal{P}}\sqrt{-\frac{3}{\mathcal{P}}}\right) - \frac{2k\pi}{3}\right] \quad \text{for } k = 1, 2, 3. \quad (18)$$

Proposition 1. The variables $\bar{\mu}$ and $\bar{\bar{\mu}}$ satisfy $\bar{\mu}_{n+1} = \bar{\mu}_{n+1}^{\text{tr}}$ and $\bar{\bar{\mu}}_{n+1} = \bar{\bar{\mu}}_{n+1}^{\text{tr}}$, respectively.

Proof. Applying the backward Euler difference on (7)₂ derives

$$0 = \text{tr}\left[\mathbf{F}_{n+1}\left(\mathbf{F}_{n+1}^{-1}\mathbf{b}_{n+1}^e\mathbf{F}_{n+1}^{-\top} - \mathbf{F}_n^{-1}\mathbf{b}_n^e\mathbf{F}_n^{-\top}\right)\mathbf{F}_{n+1}^\top\right] = \text{tr}(\mathbf{b}_{n+1}^e) - \text{tr}(\mathbf{f}_{n+1}\mathbf{b}_n^e\mathbf{f}_{n+1}^\top).$$

Note that

$$J_{n+1}^{-2/3}\mathbf{b}_{n+1}^e = (J_{n+1}^e)^{-2/3}\mathbf{b}_{n+1}^e = \bar{\mathbf{b}}_{n+1}^e$$

and

$$J_{n+1}^{-2/3}\mathbf{f}_{n+1}\mathbf{b}_n^e\mathbf{f}_{n+1}^\top = \left(J_{n+1}^f J_n^e\right)^{-2/3}\mathbf{f}_{n+1}\mathbf{b}_n^e\mathbf{f}_{n+1}^\top = \bar{\mathbf{f}}_{n+1}\bar{\mathbf{b}}_n^e\bar{\mathbf{f}}_{n+1}^\top = \bar{\mathbf{b}}_{n+1}^{e,\text{tr}}.$$

We then prove

$$\text{tr}(\bar{\mathbf{b}}_{n+1}^e) = \text{tr}(\bar{\mathbf{b}}_{n+1}^{e,\text{tr}}) \quad \Rightarrow \quad \bar{\mu}_{n+1} = \frac{\mu}{3}\text{tr}(\bar{\mathbf{b}}_{n+1}^e) = \frac{\mu}{3}\text{tr}(\bar{\mathbf{b}}_{n+1}^{e,\text{tr}}) = \bar{\mu}_{n+1}^{\text{tr}}.$$

Similarly, applying the backward Euler difference on (8)₂ derives

$$\text{tr}(\boldsymbol{\beta}_{n+1}) = \text{tr}(\mathbf{f}_{n+1}\boldsymbol{\beta}_n\mathbf{f}_{n+1}^\top) \quad \Rightarrow \quad \text{tr}(\bar{\boldsymbol{\beta}}_{n+1}) = \text{tr}(\bar{\boldsymbol{\beta}}_{n+1}^{\text{tr}}),$$

and we prove

$$\bar{\bar{\mu}}_{n+1} = \bar{\mu}_{n+1} - \frac{1}{3}\text{tr}(\bar{\boldsymbol{\beta}}_{n+1}) = \bar{\mu}_{n+1}^{\text{tr}} - \frac{1}{3}\text{tr}(\bar{\boldsymbol{\beta}}_{n+1}^{\text{tr}}) = \bar{\bar{\mu}}_{n+1}^{\text{tr}}.$$

□

Remark 2. The updating formulae for $\bar{\mathbf{b}}_{n+1}^e$ in (17) is different from (14)₁ as used in Simo (1988a,b). It is because the expression in (14)₁ is a necessary but *insufficient* condition of the isochoric plastic flow ($J_{n+1}^p = 1$). As pointed out in Wang et al. (2017) and demonstrated in Appendix C.2, the violation of the isochoric plastic flow leads to incorrect stress prediction, especially during the unloading stage. Many remedies such as the exponential map algorithm (Simo, 1992; Miehe, 1996) can fix this issue. In the current work, we propose the updating formulae in (17) that require minimum modifications to the original theory (Simo, 1988a,b), and this formula is essentially a generalized version compared to the one used in Simo and Miehe (1992). The derivation of (17) is presented in Appendix A. A comparison between the resultant FEA prediction and the analytical solution is shown in Appendix C, where we observe that the isochoric plastic flow is enforced precisely.

We emphasize that the updating formulae in (16) and (17) are fully explicit up to the unit tensor (\mathbf{n}_{n+1}) and consistency parameter ($\hat{\gamma}_{n+1}$), and we proceed to determine them. To derive the unit tensor (\mathbf{n}_{n+1}), we utilize (14)₄, (15)₄, and (17)₂ and yield

$$\mathbf{s}_{n+1} = \mu \operatorname{dev}(\bar{\mathbf{b}}_{n+1}^{e, \operatorname{tr}}) - 2\bar{\mu}_{n+1}^{\operatorname{tr}} \hat{\gamma}_{n+1} \mathbf{n}_{n+1} = \mathbf{s}_{n+1}^{\operatorname{tr}} - 2\bar{\mu}_{n+1}^{\operatorname{tr}} \hat{\gamma}_{n+1} \mathbf{n}_{n+1} \quad (19)$$

by noticing \mathbf{n}_{n+1} is deviatoric. Based on (14)₂, (15)_{2,5}, and (19), we rewrite (14)₅ as

$$\boldsymbol{\xi}_{n+1} = \mathbf{s}_{n+1} - \operatorname{dev}(\bar{\boldsymbol{\beta}}_{n+1}) = \boldsymbol{\xi}_{n+1}^{\operatorname{tr}} - 2\bar{\mu}_{n+1}^{\operatorname{tr}} \left(1 + \frac{h}{3\mu}\right) \hat{\gamma}_{n+1} \mathbf{n}_{n+1},$$

which further renders

$$\|\boldsymbol{\xi}_{n+1}\| \mathbf{n}_{n+1} = \|\boldsymbol{\xi}_{n+1}^{\operatorname{tr}}\| \mathbf{n}_{n+1}^{\operatorname{tr}} - 2\bar{\mu}_{n+1}^{\operatorname{tr}} \left(1 + \frac{h}{3\mu}\right) \hat{\gamma}_{n+1} \mathbf{n}_{n+1}$$

and implies

$$\|\boldsymbol{\xi}_{n+1}\| + 2\bar{\mu}_{n+1}^{\operatorname{tr}} \left(1 + \frac{h}{3\mu}\right) \hat{\gamma}_{n+1} = \|\boldsymbol{\xi}_{n+1}^{\operatorname{tr}}\| \quad \text{and} \quad \mathbf{n}_{n+1} = \mathbf{n}_{n+1}^{\operatorname{tr}} \quad (20)$$

under the assumption of $\bar{\mu}_{n+1}^{\operatorname{tr}} > 0$ and due to $\|\mathbf{n}_{n+1}\| = \|\mathbf{n}_{n+1}^{\operatorname{tr}}\| = 1$.

Finally, to compute the consistency parameter ($\hat{\gamma}_{n+1}$), we discuss the signs of the trial yield indicator, $f_{n+1}^{\operatorname{tr}}$. In the case of $f_{n+1}^{\operatorname{tr}} \leq 0$, the yield criterion is satisfied ($f_{n+1} < 0$ and $\hat{\gamma}_{n+1} = 0$) with $\bar{\mathbf{b}}_{n+1}^{e, \operatorname{tr}}$, $\bar{\boldsymbol{\beta}}_{n+1}^{\operatorname{tr}}$, and $\alpha_{n+1}^{\operatorname{tr}}$. We then use them to update the internal variables at load step $n + 1$ as

$$\bar{\mathbf{b}}_{n+1}^e = \bar{\mathbf{b}}_{n+1}^{e, \operatorname{tr}}, \quad \bar{\boldsymbol{\beta}}_{n+1} = \bar{\boldsymbol{\beta}}_{n+1}^{\operatorname{tr}}, \quad \text{and} \quad \alpha_{n+1} = \alpha_{n+1}^{\operatorname{tr}}.$$

In the case of $f_{n+1}^{\operatorname{tr}} > 0$, the yield criterion is violated ($f_{n+1} > 0$) with $\bar{\mathbf{b}}_{n+1}^{e, \operatorname{tr}}$, $\bar{\boldsymbol{\beta}}_{n+1}^{\operatorname{tr}}$, and $\alpha_{n+1}^{\operatorname{tr}}$. We need to make them “return” along the \mathbf{n}_{n+1} direction with a distance determined by $\hat{\gamma}_{n+1} > 0$. To figure out $\hat{\gamma}_{n+1}$, we enforce the yield criterion

$$0 = f_{n+1} = \|\boldsymbol{\xi}_{n+1}\| - \sqrt{\frac{2}{3}} k(\alpha_{n+1}) = \|\boldsymbol{\xi}_{n+1}^{\operatorname{tr}}\| - 2\bar{\mu}_{n+1}^{\operatorname{tr}} \left(1 + \frac{h}{3\mu}\right) \hat{\gamma}_{n+1} - \sqrt{\frac{2}{3}} k \left(\alpha_{n+1}^{\operatorname{tr}} + \sqrt{\frac{2}{3}} \hat{\gamma}_{n+1}\right) := \mathcal{G}(\hat{\gamma}_{n+1}) \quad (21)$$

based on (16)₂ and (20)₁. The expression in (21) is an algebraic equation of $\hat{\gamma}_{n+1}$. For the linear isotropic hardening law in (12), we analytically solve (21) for $\hat{\gamma}_{n+1}$ as

$$\hat{\gamma}_{n+1} = \frac{1}{2\bar{\mu}_{n+1}^{\operatorname{tr}}} \left(1 + \frac{h}{3\mu} + \frac{K}{3\bar{\mu}_{n+1}^{\operatorname{tr}}}\right)^{-1} \left[\|\boldsymbol{\xi}_{n+1}^{\operatorname{tr}}\| - \sqrt{\frac{2}{3}} (\sigma_y + K \alpha_{n+1}^{\operatorname{tr}}) \right]. \quad (22)$$

For the nonlinear hardening law in (13), we adopt the Newton’s method to iteratively solve $\hat{\gamma}_{n+1}$ as

$$\hat{\gamma}_{n+1}^{(k+1)} = \hat{\gamma}_{n+1}^{(k)} - \mathcal{G}(\hat{\gamma}_{n+1}^{(k)}) / \mathcal{G}'(\hat{\gamma}_{n+1}^{(k)}) \quad (23)$$

with

$$\mathcal{G}'(\hat{\gamma}_{n+1}^{(k)}) = -2\bar{\mu}_{n+1}^{\text{tr}} \left(1 + \frac{h}{3\mu} \right) - \frac{2}{3}k' \left(\alpha_{n+1}^{\text{tr}} + \sqrt{\frac{2}{3}}\hat{\gamma}_{n+1}^{(k)} \right).$$

After computing the unit tensor (\mathbf{n}_{n+1}) with (20)₂ and the consistency parameter ($\hat{\gamma}_{n+1}$) with (22) or (23), we send them back to (16) and (17) for correcting $\bar{\mathbf{b}}_{n+1}^e$, $\bar{\boldsymbol{\beta}}_{n+1}$, and α_{n+1} . This entire prediction–correction procedure forms a closed loop and is typically referred to as the return mapping scheme for elastoplasticity. For the reader’s convenience, we present the implementation of this scheme in Algorithm 1 and the relationships between the primary state variables at load steps n and $n + 1$ in Fig. 3.

Algorithm 1: Return mapping scheme for finite strain elastoplasticity

- 1 **Inputs:**
 - 2 Volume-preserving part of the elastic left Cauchy–Green deformation tensor, $\bar{\mathbf{b}}_n^e$;
 - 3 “Volume-preserving” part of the back stress tensor, $\bar{\boldsymbol{\beta}}_n$;
 - 4 Equivalent plastic strain, α_n ;
 - 5 Deformation gradients at load steps n and $n + 1$, \mathbf{F}_n and \mathbf{F}_{n+1} , respectively;
 - 6 **Prediction stage:**
 - 7 Compute the relative deformation gradient as $\mathbf{f}_{n+1} = \mathbf{F}_{n+1}\mathbf{F}_n^{-1}$;
 - 8 Compute the volume-preserving part of \mathbf{f}_{n+1} as $\bar{\mathbf{f}}_{n+1} = \left(J_{n+1}^f \right)^{-1/3} \mathbf{f}_{n+1}$;
 - 9 Compute the trial version of $\bar{\mathbf{b}}_{n+1}^e$ as $\bar{\mathbf{b}}_{n+1}^{e, \text{tr}} = \bar{\mathbf{f}}_{n+1} \bar{\mathbf{b}}_n^e \bar{\mathbf{f}}_{n+1}^\top$;
 - 10 Compute the trial version of $\bar{\boldsymbol{\beta}}_{n+1}$ as $\bar{\boldsymbol{\beta}}_{n+1}^{\text{tr}} = \bar{\mathbf{f}}_{n+1} \bar{\boldsymbol{\beta}}_n \bar{\mathbf{f}}_{n+1}^\top$;
 - 11 Compute the trial version of α_{n+1} as $\alpha_{n+1}^{\text{tr}} = \alpha_n$;
 - 12 Compute the trial deviatoric Kirchhoff stress tensor as $\mathbf{s}_{n+1}^{\text{tr}} = \mu \operatorname{dev} \left(\bar{\mathbf{b}}_{n+1}^{e, \text{tr}} \right)$;
 - 13 Compute the trial net stress tensor as $\boldsymbol{\xi}_{n+1}^{\text{tr}} = \mathbf{s}_{n+1}^{\text{tr}} - \operatorname{dev} \left(\bar{\boldsymbol{\beta}}_{n+1}^{\text{tr}} \right)$;
 - 14 Compute the unit tensor as $\mathbf{n}_{n+1} = \mathbf{n}_{n+1}^{\text{tr}} = \boldsymbol{\xi}_{n+1}^{\text{tr}} / \|\boldsymbol{\xi}_{n+1}^{\text{tr}}\|$;
 - 15 Compute the parameters $\bar{\mu}_{n+1}^{\text{tr}} = \mu \operatorname{tr} \left(\bar{\mathbf{b}}_{n+1}^{e, \text{tr}} \right) / 3$ and $\bar{\mu}_{n+1}^{\text{tr}} = \bar{\mu}_{n+1}^{\text{tr}} - \operatorname{tr} \left(\bar{\boldsymbol{\beta}}_{n+1}^{\text{tr}} \right) / 3$;
 - 16 Compute the trial yield indicator as $f_{n+1}^{\text{tr}} = \|\boldsymbol{\xi}_{n+1}^{\text{tr}}\| - \sqrt{2/3}k \left(\alpha_{n+1}^{\text{tr}} \right)$;
 - 17 **Correction stage:**
 - 18 **if** $f_{n+1}^{\text{tr}} \leq 0$ **then**
 - 19 | Set the consistency parameter as $\hat{\gamma}_{n+1} = 0$;
 - 20 **else**
 - 21 | **if** the isotropic hardening law ($k(\alpha)$) is linear **then**
 - 22 | | Compute $\hat{\gamma}_{n+1} > 0$ with (22);
 - 23 | **else**
 - 24 | | Compute $\hat{\gamma}_{n+1} > 0$ with (23);
 - 25 | **end**
 - 26 **end**
 - 27 Compute \mathcal{I}_1 based on (17)₃;
 - 28 Update $\bar{\mathbf{b}}_{n+1}^e$ as $\bar{\mathbf{b}}_{n+1}^e = \operatorname{dev} \left(\bar{\mathbf{b}}_{n+1}^{e, \text{tr}} \right) - 2 \left(\bar{\mu}_{n+1}^{\text{tr}} / \mu \right) \hat{\gamma}_{n+1} \mathbf{n}_{n+1} + \mathcal{I}_1 \mathbf{I} / 3$;
 - 29 Update $\bar{\boldsymbol{\beta}}_{n+1}$ as $\bar{\boldsymbol{\beta}}_{n+1} = \bar{\boldsymbol{\beta}}_{n+1}^{\text{tr}} + 2h/3 \left(\bar{\mu}_{n+1}^{\text{tr}} / \mu \right) \hat{\gamma}_{n+1} \mathbf{n}_{n+1}$;
 - 30 Update α_{n+1} as $\alpha_{n+1} = \alpha_{n+1}^{\text{tr}} + \sqrt{2/3} \hat{\gamma}_{n+1}$;
-

2.3. Global governing equations for finite strain elastoplasticity

We remark again that the return mapping scheme in Section 2.2.4 pertains to the elastoplastic response of a single material point ($\mathbf{X} \in \Omega_0$). To predict the elastoplastic response of the entire structure defined on Ω_0 , we derive the global governing equations as follows.

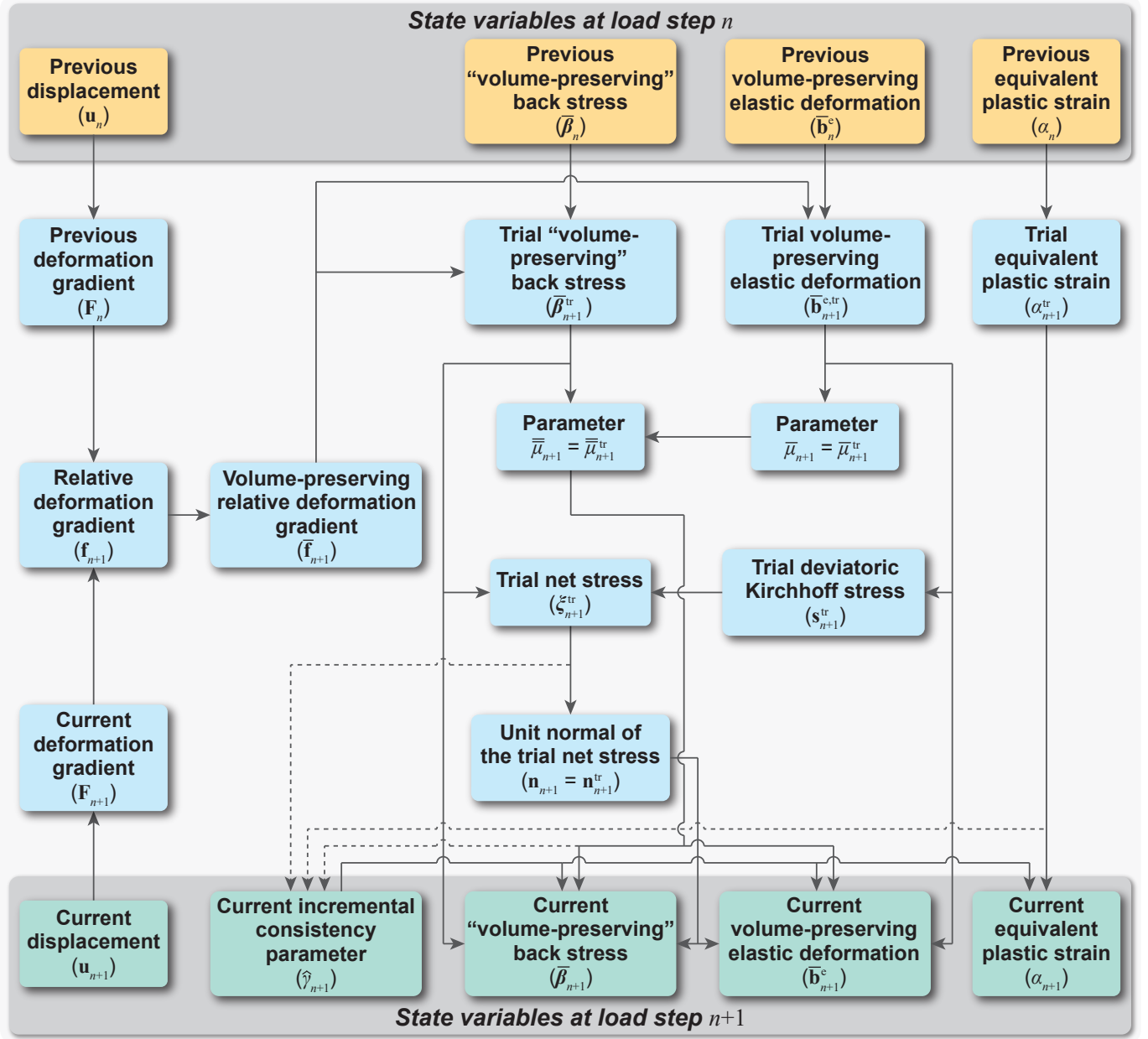


Figure 3: Relationships between the primary state variables at load steps n and $n+1$. The dashed arrows signify that $\hat{\gamma}_{n+1}$ generally does not admit to an explicit expression and needs to be numerically solved from (21) with (23).

2.3.1. Stress measures and algorithmic tangent moduli

Substituting (19) into (6) reformulates the Kirchhoff stress tensor ($\boldsymbol{\tau}_{n+1}$) at load step $n+1$ as

$$\boldsymbol{\tau}_{n+1} = \boldsymbol{\tau}_{n+1}^{\text{vol}} + \mathbf{s}_{n+1}^{\text{tr}} - 2\bar{\bar{\mu}}_{n+1}^{\text{tr}} \hat{\gamma}_{n+1} \mathbf{n}_{n+1}.$$

Accordingly, we compute the first Piola–Kirchhoff stress tensor (\mathbf{P}_{n+1}) as

$$\mathbf{P}_{n+1} = \boldsymbol{\tau}_{n+1} \mathbf{F}_{n+1}^{-\top} = \left(\boldsymbol{\tau}_{n+1}^{\text{vol}} + \mathbf{s}_{n+1}^{\text{tr}} - 2\bar{\bar{\mu}}_{n+1}^{\text{tr}} \hat{\gamma}_{n+1} \mathbf{n}_{n+1} \right) \mathbf{F}_{n+1}^{-\top} \quad (24)$$

and the second Piola–Kirchhoff stress tensor (\mathbf{S}_{n+1}) as

$$\mathbf{S}_{n+1} = \varphi^*(\boldsymbol{\tau}_{n+1}) = \varphi^*(\boldsymbol{\tau}_{n+1}^{\text{vol}}) + \varphi^*(\mathbf{s}_{n+1}^{\text{tr}}) - 2\bar{\bar{\mu}}_{n+1}^{\text{tr}} \hat{\gamma}_{n+1} \varphi^*(\mathbf{n}_{n+1}). \quad (25)$$

Based on the second Piola–Kirchhoff stress tensor (\mathbf{S}_{n+1}), we compute the second *algorithmic* tangent moduli as

$$\mathbb{C}_{n+1} = \frac{\partial \mathbf{S}_{n+1}}{\partial \mathbf{E}_{n+1}} = \begin{cases} \mathbb{C}_{n+1}^{\text{el}}, & \text{if } f_{n+1}^{\text{tr}} \leq 0 \ (\hat{\gamma}_{n+1} = 0; \text{ hyperelastic}); \\ \mathbb{C}_{n+1}^{\text{ep}}, & \text{if } f_{n+1}^{\text{tr}} > 0 \ (\hat{\gamma}_{n+1} > 0; \text{ elastoplastic}). \end{cases} \quad (26)$$

Here, the variable $\mathbb{C}_{n+1}^{\text{el}}$ is the second elastic moduli given as

$$\begin{aligned} \mathbb{C}_{n+1}^{\text{el}} = \frac{\partial \varphi^*(\hat{\boldsymbol{\tau}}_{n+1})}{\partial \mathbf{E}_{n+1}} &= (2\bar{\mu}_{n+1} - 2J_{n+1}U'_{n+1}) \mathbb{I}_{\mathbf{C}_{n+1}^{-1}} + \left[J_{n+1}(J_{n+1}U'_{n+1})' - \frac{2\bar{\mu}_{n+1}}{3} \right] \mathbf{C}_{n+1}^{-1} \otimes \mathbf{C}_{n+1}^{-1} \\ &\quad - \frac{2}{3} [\varphi^*(\hat{\mathbf{s}}_{n+1}) \otimes \mathbf{C}_{n+1}^{-1} + \mathbf{C}_{n+1}^{-1} \otimes \varphi^*(\hat{\mathbf{s}}_{n+1})] \end{aligned} \quad (27)$$

where we define

$$\left(\mathbb{I}_{\mathbf{C}_{n+1}^{-1}} \right)_{ijkl} = \frac{1}{2} \left[(C_{n+1}^{-1})_{ik} (C_{n+1}^{-1})_{jl} + (C_{n+1}^{-1})_{il} (C_{n+1}^{-1})_{jk} \right].$$

The variable $\mathbb{C}_{n+1}^{\text{ep}}$ is the second elastoplastic moduli (see Appendix B for derivation) expressed as

$$\begin{aligned} \mathbb{C}_{n+1}^{\text{ep}} &= \left(2\bar{\mu}_{n+1}^{\text{tr}} - 2c_1 \bar{\bar{\mu}}_{n+1}^{\text{tr}} - 2J_{n+1}U'_{n+1} \right) \mathbb{I}_{\mathbf{C}_{n+1}^{-1}} + \left[J_{n+1}(J_{n+1}U'_{n+1})' - \frac{2\bar{\mu}_{n+1}^{\text{tr}}}{3} + \frac{2c_1 \bar{\bar{\mu}}_{n+1}^{\text{tr}}}{3} \right] \mathbf{C}_{n+1}^{-1} \otimes \mathbf{C}_{n+1}^{-1} \\ &\quad - \frac{2}{3} [\varphi^*(\mathbf{s}_{n+1}^{\text{tr}}) \otimes \mathbf{C}_{n+1}^{-1} + \mathbf{C}_{n+1}^{-1} \otimes \varphi^*(\mathbf{s}_{n+1}^{\text{tr}})] + \frac{2c_1}{3} [\varphi^*(\boldsymbol{\xi}_{n+1}^{\text{tr}}) \otimes \mathbf{C}_{n+1}^{-1} + \mathbf{C}_{n+1}^{-1} \otimes \varphi^*(\boldsymbol{\xi}_{n+1}^{\text{tr}})] \\ &\quad - c_3 \varphi^*(\mathbf{n}_{n+1}) \otimes \varphi^*(\mathbf{n}_{n+1}) - \frac{c_4}{2} \{ \varphi^*(\mathbf{n}_{n+1}) \otimes \varphi^* [\text{dev}(\mathbf{n}_{n+1}^2)] + \varphi^* [\text{dev}(\mathbf{n}_{n+1}^2)] \otimes \varphi^*(\mathbf{n}_{n+1}) \} \end{aligned} \quad (28)$$

where we define

$$\begin{cases} c_0 = 1 + \frac{h}{3\mu} + \frac{k'}{3\bar{\mu}_{n+1}^{\text{tr}}}, & c_1 = \frac{2\bar{\mu}_{n+1}^{\text{tr}} \hat{\gamma}_{n+1}}{\|\boldsymbol{\xi}_{n+1}^{\text{tr}}\|}, & c_2 = \frac{1}{c_0} - c_1, \\ c_3 = 2c_2 \bar{\bar{\mu}}_{n+1}^{\text{tr}} - \left[\frac{1}{c_0} \left(1 + \frac{h}{3\mu} \right) - 1 \right] \frac{4}{3} \hat{\gamma}_{n+1} \|\boldsymbol{\xi}_{n+1}^{\text{tr}}\|, & c_4 = 2c_2 \|\boldsymbol{\xi}_{n+1}^{\text{tr}}\|. \end{cases} \quad (29)$$

By examining the second elastic moduli ($\mathbb{C}_{n+1}^{\text{el}}$) in (27) and elastoplastic moduli ($\mathbb{C}_{n+1}^{\text{ep}}$) in (28), we reformulate the second algorithmic tangent moduli (\mathbb{C}_{n+1}) in (26) into a compact form as

$$\begin{aligned} \mathbb{C}_{n+1} &= \left(2\bar{\mu}_{n+1}^{\text{tr}} - 2\theta c_1 \bar{\bar{\mu}}_{n+1}^{\text{tr}} - 2J_{n+1}U'_{n+1} \right) \mathbb{I}_{\mathbf{C}_{n+1}^{-1}} + \left[J_{n+1}(J_{n+1}U'_{n+1})' - \frac{2\bar{\mu}_{n+1}^{\text{tr}}}{3} + \frac{2\theta c_1 \bar{\bar{\mu}}_{n+1}^{\text{tr}}}{3} \right] \mathbf{C}_{n+1}^{-1} \otimes \mathbf{C}_{n+1}^{-1} \\ &\quad - \frac{2}{3} [\varphi^*(\mathbf{s}_{n+1}^{\text{tr}}) \otimes \mathbf{C}_{n+1}^{-1} + \mathbf{C}_{n+1}^{-1} \otimes \varphi^*(\mathbf{s}_{n+1}^{\text{tr}})] + \frac{2\theta c_1}{3} [\varphi^*(\boldsymbol{\xi}_{n+1}^{\text{tr}}) \otimes \mathbf{C}_{n+1}^{-1} + \mathbf{C}_{n+1}^{-1} \otimes \varphi^*(\boldsymbol{\xi}_{n+1}^{\text{tr}})] \\ &\quad - \theta c_3 \varphi^*(\mathbf{n}_{n+1}) \otimes \varphi^*(\mathbf{n}_{n+1}) - \frac{\theta c_4}{2} \{ \varphi^*(\mathbf{n}_{n+1}) \otimes \varphi^* [\text{dev}(\mathbf{n}_{n+1}^2)] + \varphi^* [\text{dev}(\mathbf{n}_{n+1}^2)] \otimes \varphi^*(\mathbf{n}_{n+1}) \} \end{aligned} \quad (30)$$

with

$$\theta = \frac{1}{2} \frac{f_{n+1}^{\text{tr}} + |f_{n+1}^{\text{tr}}|}{f_{n+1}^{\text{tr}}} = \begin{cases} 0, & \text{if } f_{n+1}^{\text{tr}} \leq 0 \ (\text{hyperelastic}); \\ 1, & \text{if } f_{n+1}^{\text{tr}} > 0 \ (\text{elastoplastic}). \end{cases} \quad (31)$$

2.3.2. Governing equations

Based on the stress measures and tangent moduli defined above, we present the global governing equations in an incremental form as

$$\left\{ \begin{array}{l} \int_{\Omega_0} \nabla \mathbf{v} : \widehat{\mathbb{C}}_{n+1}^{(k)} : \nabla \delta \mathbf{u}_{n+1}^{(k)} \, d\mathbf{X} = \int_{\Omega_0} \bar{\mathbf{q}}_{n+1} \cdot \mathbf{v} \, d\mathbf{X} + \int_{\partial\Omega_0^{\mathcal{N}}} \bar{\mathbf{t}}_{n+1} \cdot \mathbf{v} \, d\mathbf{X} - \int_{\Omega_0} \mathbf{P}_{n+1}^{(k)} : \nabla \mathbf{v} \, d\mathbf{X}, \\ \delta \mathbf{u}_{n+1}^{(k)} = \bar{\mathbf{u}}_{n+1} - \mathbf{u}_{n+1}^{(k)} \quad \text{for } \mathbf{X} \in \partial\Omega_0^{\mathcal{D}}, \\ \mathbf{u}_{n+1}^{(k+1)} = \mathbf{u}_{n+1}^{(k)} + l_{n+1}^{(k)} \delta \mathbf{u}_{n+1}^{(k)} \quad \text{for } \mathbf{X} \in \bar{\Omega}_0. \end{array} \right. \quad (32)$$

Here, the variable $\delta \mathbf{u}_{n+1}$ is the incremental displacement field, and \mathbf{v} is the test displacement field. The variables $\bar{\mathbf{q}}_{n+1}$, $\bar{\mathbf{t}}_{n+1}$, and $\bar{\mathbf{u}}_{n+1}$ are the prescribed body force, traction, and displacement, respectively. The symbol $l_{n+1} \in (0, 1]$ represents a line search parameter such that the updated displacement field reduces the absolute residual (right-hand side of (32)₁). The superscript (k) of a variable represents the value evaluated at Newton iteration k . The symbol $\bar{\Omega}_0$ is the closed bounded domain in its undeformed configuration with Neumann ($\partial\Omega_0^{\mathcal{N}}$) and Dirichlet ($\partial\Omega_0^{\mathcal{D}}$) boundaries. The variable $\widehat{\mathbb{C}}_{n+1}$ is the first algorithmic tangent moduli, which can be computed from \mathbf{S}_{n+1} in (25) and \mathbb{C}_{n+1} in (30) and expressed in indicial notation as

$$(\widehat{\mathbb{C}}_{n+1})_{rjssl} = (F_{n+1})_{ri} (F_{n+1})_{sk} (\mathbb{C}_{n+1})_{ijkl} + \delta_{rs} (S_{n+1})_{jl}.$$

After some tensor algebra, we write out the integrand of the left-hand side in (32)₁ as

$$\begin{aligned} \nabla \mathbf{v} : \widehat{\mathbb{C}} : \nabla \delta \mathbf{u} = & \left(2\bar{\mu}^{\text{tr}} - 2\theta c_1 \bar{\bar{\mu}}^{\text{tr}} - 2JU' \right) (\mathcal{U})^{\text{sym}} : \mathcal{V} + \left[J(JU')' - \frac{2\bar{\mu}^{\text{tr}}}{3} + \frac{2\theta c_1 \bar{\bar{\mu}}^{\text{tr}}}{3} \right] \text{tr}(\mathcal{U}) \text{tr}(\mathcal{V}) \\ & - \frac{2}{3} [\text{tr}(\mathcal{U}) \mathbf{s}^{\text{tr}} : \mathcal{V} + \text{tr}(\mathcal{V}) \mathbf{s}^{\text{tr}} : \mathcal{U}] + \frac{2\theta c_1}{3} [\text{tr}(\mathcal{U}) \boldsymbol{\xi}^{\text{tr}} : \mathcal{V} + \text{tr}(\mathcal{V}) \boldsymbol{\xi}^{\text{tr}} : \mathcal{U}] \\ & - \theta c_3 (\mathbf{n} : \mathcal{V}) (\mathbf{n} : \mathcal{U}) - \frac{\theta c_4}{2} \{ (\mathbf{n} : \mathcal{V}) [\text{dev}(\mathbf{n}^2) : \mathcal{U}] + [\text{dev}(\mathbf{n}^2) : \mathcal{V}] (\mathbf{n} : \mathcal{U}) \} + (\nabla \delta \mathbf{u} \, \mathbf{S}) : \nabla \mathbf{v} \end{aligned} \quad (33)$$

by defining

$$\mathcal{U} = \nabla \delta \mathbf{u} \, \mathbf{F}^{-1} \quad \text{and} \quad \mathcal{V} = \nabla \mathbf{v} \, \mathbf{F}^{-1}$$

where we temporarily drop the subscript $n+1$ and superscript (k) for conciseness. We remark that (32) are explicit, linear equations of $\delta \mathbf{u}_{n+1}^{(k)}$, where all coefficients can be predetermined by $\bar{\mathbf{b}}_n^e$, $\bar{\boldsymbol{\beta}}_n$, α_n , \mathbf{u}_n , and $\mathbf{u}_{n+1}^{(k)}$. Consequently, we can iteratively solve $\delta \mathbf{u}_{n+1}^{(k)}$ from (32) and update $\mathbf{u}_{n+1}^{(k+1)}$ until convergence.

For the reader's convenience, we outline the solution scheme in Algorithm 2. To enhance the convergence of the highly non-convex elastoplasticity problem, we incorporate an adaptive line search scheme (Algorithm 3), which iteratively reduces the line search parameter ($l_{n+1}^{(k)}$) until the residual starts to decrease. Furthermore, we employ an adaptive loading scheme (Algorithm 4) that dynamically adjusts the applied boundary values ($\bar{\mathbf{q}}$, $\bar{\mathbf{t}}$, and $\bar{\mathbf{u}}$) in cases where Newton iterations diverge occasionally. With the combination of Algorithms 1–4, we successfully obtain converged FEA solutions for all examples introduced in Section 4. The convergence, precision, and computational time of FEA for a sample design case are demonstrated in Appendix D.

3. Topology optimization framework for finite strain elastoplasticity

Built upon the finite strain elastoplasticity theory in Section 2, we now present the topology optimization framework for optimizing elastoplastic structures undergoing large deformations. This framework comprises design space parameterization, material property interpolation, topology optimization formulation, and sensitivity analysis and verification. This section details the first three components while the sensitivity analysis and verification are provided in Appendix E.

Algorithm 2: Overall solution scheme for finite strain elastoplasticity

```

1 Inputs: Initial state variables,  $\bar{\mathbf{b}}_0^e \leftarrow \mathbf{I}$ ,  $\bar{\boldsymbol{\beta}}_0 \leftarrow \mathbf{0}$ ,  $\alpha_0 \leftarrow 0$ , and  $\mathbf{u}_0 \leftarrow \mathbf{0}$ ; Prescribed body force ( $\bar{\mathbf{q}}$ ),
   traction ( $\bar{\mathbf{t}}$ ), and displacement ( $\bar{\mathbf{u}}$ ); Prescribed time steps,  $\{t_1, t_2, \dots, t_{M-1}, t_M\}$ ; Maximum Newton
   iterations,  $N^{\text{iter}}$ ; Absolute and relative tolerances of Newton iterations,  $\varepsilon^{\text{abs}}$  and  $\varepsilon^{\text{rel}}$ , respectively;
2 Initialize the converged time step,  $t^{\text{conv}} \leftarrow 0$ ;
3 Initialize the time step count,  $m \leftarrow 1$ , load step count,  $n \leftarrow 0$ , and try count,  $r \leftarrow 0$ ;
4 while  $m \leq M$  do
5   Initialize the current time step,  $t^{\text{now}} \leftarrow t_m$ ;
6   while  $t^{\text{conv}} < t_m$  do
7     Update the boundary values,  $\bar{\mathbf{q}}_{n+1} \leftarrow t^{\text{now}} \bar{\mathbf{q}}$ ,  $\bar{\mathbf{t}}_{n+1} \leftarrow t^{\text{now}} \bar{\mathbf{t}}$ , and  $\bar{\mathbf{u}}_{n+1} \leftarrow t^{\text{now}} \bar{\mathbf{u}}$ ;
8     Compute the previous deformation gradient,  $\mathbf{F}_n \leftarrow \mathbf{I} + \nabla \mathbf{u}_n$ ;
9     Initialize the displacement field at load step  $n + 1$  and Newton iteration 0,  $\mathbf{u}_{n+1}^{(0)} \leftarrow \mathbf{u}_n$ ;
10    Compute the absolute residual (right-hand side of (32)1),  $a_{n+1}^{(0)}$ ;
11    Initialize the convergence flag, convergence  $\leftarrow$  false;
12    Initialize the Newton iteration count,  $k \leftarrow 0$ ;
13    while  $k < N^{\text{iter}}$  do
14      Compute the current deformation gradient,  $\mathbf{F}_{n+1}^{(k)} \leftarrow \mathbf{I} + \nabla \mathbf{u}_{n+1}^{(k)}$ ;
15      Compute  $\alpha_{n+1}^{\text{tr},(k)}$ ,  $\mathbf{s}_{n+1}^{\text{tr},(k)}$ ,  $\boldsymbol{\xi}_{n+1}^{\text{tr},(k)}$ ,  $\mathbf{n}_{n+1}^{\text{tr},(k)}$ ,  $\bar{\mu}_{n+1}^{\text{tr},(k)}$ ,  $\overline{\mu}_{n+1}^{\text{tr},(k)}$ ,  $f_{n+1}^{\text{tr},(k)}$ , and  $\hat{\gamma}_{n+1}^{(k)}$  by providing
        Algorithm 1 with  $\bar{\mathbf{b}}_n^e$ ,  $\bar{\boldsymbol{\beta}}_n$ ,  $\alpha_n$ ,  $\mathbf{F}_n$ , and  $\mathbf{F}_{n+1}^{(k)}$ ;
16      Compute  $\mathbf{P}_{n+1}^{(k)}$  in (24) and  $\mathbf{S}_{n+1}^{(k)}$  in (25) based on  $\mathbf{F}_{n+1}^{(k)}$ ,  $\mathbf{s}_{n+1}^{\text{tr},(k)}$ ,  $\mathbf{n}_{n+1}^{\text{tr},(k)}$ ,  $\overline{\mu}_{n+1}^{\text{tr},(k)}$ , and  $\hat{\gamma}_{n+1}^{(k)}$ ;
17      Compute  $c_1$ ,  $c_3$ , and  $c_4$  in (29) based on  $\alpha_{n+1}^{\text{tr},(k)}$ ,  $\boldsymbol{\xi}_{n+1}^{\text{tr},(k)}$ ,  $\overline{\mu}_{n+1}^{\text{tr},(k)}$ , and  $\hat{\gamma}_{n+1}^{(k)}$ ;
18      Compute  $\theta$  in (31) based on  $f_{n+1}^{(k)}$ ;
19      Compute  $\nabla \mathbf{v} : \hat{\mathbf{C}}_{n+1}^{(k)} : \nabla \delta \mathbf{u}_{n+1}^{(k)}$  in (33) (as a function of  $\delta \mathbf{u}_{n+1}^{(k)}$  and  $\mathbf{v}$ ) based on  $\mathbf{F}_{n+1}^{(k)}$ ,
         $\mathbf{s}_{n+1}^{\text{tr},(k)}$ ,  $\boldsymbol{\xi}_{n+1}^{\text{tr},(k)}$ ,  $\mathbf{n}_{n+1}^{\text{tr},(k)}$ ,  $\bar{\mu}_{n+1}^{\text{tr},(k)}$ ,  $\overline{\mu}_{n+1}^{\text{tr},(k)}$ ,  $c_1$ ,  $c_3$ ,  $c_4$ , and  $\theta$ ;
20      Solve  $\delta \mathbf{u}_{n+1}^{(k)}$  from (32)1,2 based on  $\nabla \mathbf{v} : \hat{\mathbf{C}}_{n+1}^{(k)} : \nabla \delta \mathbf{u}_{n+1}^{(k)}$ ,  $\mathbf{P}_{n+1}^{(k)}$ ,  $\bar{\mathbf{q}}_{n+1}$ ,  $\bar{\mathbf{t}}_{n+1}$ , and  $\bar{\mathbf{u}}_{n+1}$ ;
21      Compute  $\mathbf{u}_{n+1}^{(k+1)}$  and  $a_{n+1}^{(k+1)}$  by providing  $\mathbf{u}_{n+1}^{(k)}$ ,  $a_{n+1}^{(k)}$ , and  $\delta \mathbf{u}_{n+1}^{(k)}$  to the line search
        scheme in Algorithm 3;
22      Compute the relative residual,  $r_{n+1}^{(k+1)} \leftarrow a_{n+1}^{(k+1)} / a_{n+1}^{(1)}$ ;
23      Update the Newton iteration count,  $k \leftarrow k + 1$ ;
24      if  $a_{n+1}^{(k)} \leq \varepsilon^{\text{abs}}$  or  $r_{n+1}^{(k)} \leq \varepsilon^{\text{rel}}$  then
25        | Update the convergence flag, convergence  $\leftarrow$  true;
26        | Break the Newton iterations due to convergence;
27      end
28    end
29    Update the current state variables,  $\bar{\mathbf{b}}_{n+1}^e$ ,  $\bar{\boldsymbol{\beta}}_{n+1}$ ,  $\alpha_{n+1}$ ,  $\hat{\gamma}_{n+1}$ , and  $\mathbf{u}_{n+1}$ , by providing  $\bar{\mathbf{b}}_n^e$ ,  $\bar{\boldsymbol{\beta}}_n$ ,
         $\alpha_n$ ,  $\mathbf{F}_n$ ,  $\mathbf{u}_{n+1}^{(k)}$ ,  $t^{\text{conv}}$ ,  $t^{\text{now}}$ ,  $t_m$ ,  $n$ , and  $r$  to the adaptive loading scheme in Algorithm 4;
30  end
31  Update the time step count,  $m \leftarrow m + 1$ ;
32 end

```

Algorithm 3: Adaptive line search scheme

1 **Inputs:** Displacement and absolute residual from previous Newton iteration, $\mathbf{u}_{n+1}^{(k)}$ and $a_{n+1}^{(k)}$, respectively; Incremental displacement, $\delta\mathbf{u}_{n+1}^{(k)}$; Maximum iterations and tolerance for line search, N^{search} and $\varepsilon^{\text{search}} \in (0, 1]$, respectively;

2 Initialize the line search parameter, $l_{n+1}^{(k)} \leftarrow 1$;

3 Initialize the iteration count for linear search, $s \leftarrow 1$;

4 **for** $s \leq N^{\text{search}}$ **do**

5 Update $\mathbf{u}_{n+1}^{(k+1)}$ in (32)₃ based on $\mathbf{u}_{n+1}^{(k)}$, $\delta\mathbf{u}_{n+1}^{(k)}$, and $l_{n+1}^{(k)}$;

6 Compute the absolute residual, $a_{n+1}^{(k+1)}$;

7 **if** $a_{n+1}^{(k+1)} < \varepsilon^{\text{search}} a_{n+1}^{(k)}$ **then**

8 | Break the line search due to convergence;

9 **else**

10 | Shrink the line search parameter, $l_{n+1}^{(k)} \leftarrow l_{n+1}^{(k)}/2$;

11 | Update the line search count, $s \leftarrow s + 1$;

12 **end**

13 **end**

Algorithm 4: Adaptive loading scheme

1 **Inputs:** Convergence flag, **convergence**; Internal variables from the previous load step, $\bar{\mathbf{b}}_n^e$, $\bar{\beta}_n$, and α_n ; Deformation gradient from the previous load step, \mathbf{F}_n ; Displacement in the current Newton iteration, $\mathbf{u}_{n+1}^{(k)}$; Maximum tries of the adaptive loading, N^{try} ; Converged, current, and target time steps, t^{conv} , t^{now} , and t_m , respectively; Load step count, n ; Try count, r ;

2 **if** **convergence** is **false** and $r \leq N^{\text{try}}$ **then**

3 | Shrink the current time step, $t^{\text{now}} \leftarrow (t^{\text{conv}} + t^{\text{now}})/2$;

4 | Update the try count, $r \leftarrow r + 1$;

5 **else**

6 | Reset the try count, $r \leftarrow 0$;

7 | Update the converged time step, $t^{\text{conv}} \leftarrow t^{\text{now}}$;

8 | Update the current time step, $t^{\text{now}} \leftarrow t_m$;

9 | Update the current incremental consistency parameter, $\hat{\gamma}_{n+1} \leftarrow \hat{\gamma}_{n+1}^{(k)}$, and displacement field, $\mathbf{u}_{n+1} \leftarrow \mathbf{u}_{n+1}^{(k)}$;

10 | Update the current internal variables, $\bar{\mathbf{b}}_{n+1}^e$, $\bar{\beta}_{n+1}$, and α_{n+1} , by providing Algorithm 1 with $\bar{\mathbf{b}}_n^e$, $\bar{\beta}_n$, α_n , \mathbf{F}_n , and $\mathbf{F}_{n+1} \leftarrow \mathbf{I} + \nabla\mathbf{u}_{n+1}$;

11 | Update the load step count, $n \leftarrow n + 1$;

12 **end**

3.1. Design space parameterization

Before proceeding with topology optimization, one prerequisite is to identify suitable design variables that parameterize the large design space of structural geometries and material phases. Following the blueprint of topology optimization for infinitesimal strain elastoplasticity (Jia et al., 2025), we start by defining one density variable, $\rho(\mathbf{X}) : \Omega_0 \mapsto [0, 1]$, and $N^\xi \geq 1$ material variables, $\xi_1(\mathbf{X}), \xi_2(\mathbf{X}), \dots, \xi_{N^\xi}(\mathbf{X}) : \Omega_0 \mapsto [0, 1]$. To reduce the mesh dependence and avoid the checkerboard patterns of designs, we apply a linear filter (Bourdin, 2001) on all design variables and derive their filtered versions as

$$\tilde{\zeta}(\mathbf{X}) = \frac{\int_{\Omega_0} w_\zeta(\mathbf{X}, \mathbf{X}') \zeta(\mathbf{X}') d\mathbf{X}'}{\int_{\Omega_0} w_\zeta(\mathbf{X}, \mathbf{X}') d\mathbf{X}'} \quad \text{for } \zeta \in \{\rho, \xi_1, \xi_2, \dots, \xi_{N^\xi}\}.$$

Here, $w_\zeta(\mathbf{X}, \mathbf{X}') = \max\{0, R_\zeta - \|\mathbf{X} - \mathbf{X}'\|_2\}$ is a weighting factor, and $R_\zeta \geq 0$ is the filter radius.

To promote pure solid-void designs with discrete material interfaces, we further apply a Heaviside projection (Bendsoe and Sigmund, 2003) on the filtered design variables, $\tilde{\rho}(\mathbf{X}), \tilde{\xi}_1(\mathbf{X}), \tilde{\xi}_2(\mathbf{X}), \dots, \tilde{\xi}_{N^\xi}(\mathbf{X}) : \Omega_0 \mapsto [0, 1]$, and derive their projected versions as

$$\hat{\zeta}(\mathbf{X}) = \frac{\tanh(\beta_\zeta \theta_\zeta) + \tanh(\beta_\zeta (\tilde{\zeta}(\mathbf{X}) - \theta_\zeta))}{\tanh(\beta_\zeta \theta_\zeta) + \tanh(\beta_\zeta (1 - \theta_\zeta))} \quad \text{for } \zeta \in \{\rho, \xi_1, \xi_2, \dots, \xi_{N^\xi}\}, \quad (34)$$

where β_ζ is a sharpness parameter, and θ_ζ is the projection threshold. Based on the projected density variable, $\hat{\rho}(\mathbf{X}) : \Omega_0 \mapsto [0, 1]$, we define the physical density variable as $\bar{\rho}(\mathbf{X}) \equiv \hat{\rho}(\mathbf{X}) : \Omega_0 \mapsto [0, 1]$. Here, $\bar{\rho}(\mathbf{X}) = 1$ represents that material point \mathbf{X} is occupied by the solid material, and $\bar{\rho}(\mathbf{X}) = 0$ signifies the void.

As for the projected material variables, $\hat{\xi}_1(\mathbf{X}), \hat{\xi}_2(\mathbf{X}), \dots, \hat{\xi}_{N^\xi}(\mathbf{X}) : \Omega_0 \mapsto [0, 1]$, we further apply a modified version of the hypercube-to-simplex-projection (HSP) (Zhou et al., 2018) as

$$\begin{cases} \bar{\xi}_n(\mathbf{X}) = \sum_{k=1}^{2^{N^\xi}} b_{nk} \left\{ (-1)^{N^\xi + \sum_{l=1}^{N^\xi} c_{kl}} \prod_{m=1}^{N^\xi} (\hat{\xi}_m(\mathbf{X}) + c_{km} - 1) \right\} & \text{for } n = 1, 2, \dots, N^\xi, \\ \bar{\xi}_{N^{\text{mat}}}(\mathbf{X}) = 1 - \sum_{n=1}^{N^\xi} \bar{\xi}_n(\mathbf{X}), \end{cases}$$

to ensure that the summation of the physical material variables, $\bar{\xi}_1(\mathbf{X}), \bar{\xi}_2(\mathbf{X}), \dots, \bar{\xi}_{N^{\text{mat}}}(\mathbf{X}) : \Omega_0 \mapsto [0, 1]$, is equal to one ($\sum_{n=1}^{N^{\text{mat}}} \bar{\xi}_n(\mathbf{X}) = 1$). Here, the parameter $N^{\text{mat}} = N^\xi + 1$ represents the number of candidate materials. The parameter $c_{kl} \in \{0, 1\}$ is the l th coordinate component of the k th vertex of a unit hypercube in the $N^{\text{mat}} - 1$ dimensional space. The parameter b_{nk} is computed as

$$b_{nk} = \begin{cases} \frac{c_{nk}}{\sum_l c_{nl}}, & \text{if } \sum_l c_{nl} \geq 1; \\ 0, & \text{otherwise.} \end{cases}$$

Note that for a material point with $\bar{\rho}(\mathbf{X}) = 1$, the expression $\bar{\xi}_n(\mathbf{X}) = 1$ for $n = 1, 2, \dots, N^{\text{mat}}$ signifies that material n is used. Consequently, we can use the physical density ($\bar{\rho}(\mathbf{X})$) and material ($\bar{\xi}_1(\mathbf{X}), \bar{\xi}_2(\mathbf{X}), \dots, \bar{\xi}_{N^{\text{mat}}}(\mathbf{X})$) variables to describe the structural geometries and material phases in the design domain (Ω_0), respectively.

3.2. Material property interpolation

After design space parameterization, one immediate next step is to interpolate the elasticity- and plasticity-related material constants/functions for various values of physical design variables, $\bar{\rho}(\mathbf{X}) \in [0, 1]$

and $\bar{\xi}_n(\mathbf{X}) \in [0, 1]$ for $n = 1, 2, \dots, N^{\text{mat}}$. Following [Jia et al. \(2025\)](#), we interpolate the initial bulk modulus (κ), initial shear modulus (μ), isotropic hardening function (k), and kinematic hardening modulus (h) as

$$\bar{\chi}(\mathbf{X}) = [\varepsilon_\rho + (1 - \varepsilon_\rho)\bar{\rho}^{p_\chi}(\mathbf{X})] \sum_{n=1}^{N^{\text{mat}}} \bar{\xi}_n^{p_\chi}(\mathbf{X})\chi_n \quad \text{for } \chi \in \{\kappa, \mu, k, h\}. \quad (35)$$

Here, the variables $\bar{\kappa}(\mathbf{X})$, $\bar{\mu}(\mathbf{X})$, $\bar{k}(\mathbf{X})$, and $\bar{h}(\mathbf{X})$ are the interpolated material constants/functions. The material constant $\chi_n \in \{\kappa_n, \mu_n, k_n, h_n\}$ for $n = 1, 2, \dots, N^{\text{mat}}$ represents the property/function of candidate material n . The parameters $p_\kappa = p_\mu$, p_k , and p_h penalize the intermediate values of the physical density variable, $\bar{\rho}(\mathbf{X}) \in (0, 1)$, and p_ξ penalizes the intermediate values of the physical material variables, $\bar{\xi}_n(\mathbf{X}) \in (0, 1)$ for $n = 1, 2, \dots, N^{\text{mat}}$. The parameter ε_ρ is a small positive number to prevent the singularity of the stiffness of void materials.

In addition to the interpolation rules in (35) for material constants/functions, it is essential to interpolate the constitutive laws across the range of the physical density variable, $\bar{\rho} \in [0, 1]$. This consideration arises because many topology optimization problems involving finite strain analysis ([Li et al., 2023](#)) encounter divergence in FEA solutions. Such issues are typically caused by the excessive distortion of elements filled with void materials when subjected to large deformations. To address this challenge, a widely adopted and effective strategy for hyperelastic designs ([Wang et al., 2014](#)) assumes that void materials exhibit linear elastic behavior while solid materials retain their hyperelastic characteristics.

In the context of finite strain elastoplasticity, we propose to interpolate the first Piola–Kirchhoff stress tensor as

$$\check{\mathbf{P}}(\mathbf{F}, \check{\mathbf{F}}; \phi) = \phi \mathbf{P}(\check{\mathbf{F}}) - \phi \boldsymbol{\sigma}^1(\boldsymbol{\epsilon}(\check{\mathbf{F}})) + \boldsymbol{\sigma}^1(\boldsymbol{\epsilon}(\mathbf{F})). \quad (36)$$

The variable $\check{\mathbf{F}}$ is the interpolated total deformation gradient defined as

$$\check{\mathbf{F}} = \mathbf{F}(\phi \mathbf{u}) = \mathbf{I} + \phi \nabla \mathbf{u} = (1 - \phi)\mathbf{I} + \phi \mathbf{F}(\mathbf{u})$$

with

$$\phi(\mathbf{X}) = \frac{\tanh(\beta_\phi \theta_\phi) + \tanh(\beta_\phi (\bar{\rho}^{p_\kappa}(\mathbf{X}) - \theta_\phi))}{\tanh(\beta_\phi \theta_\phi) + \tanh(\beta_\phi (1 - \theta_\phi))}$$

where we assume $\phi(\mathbf{X})$ is element-wise constant and therefore $\nabla \phi(\mathbf{X}) = 0$ at the integration points. The parameters $\beta_\phi = 500$ and $\theta_\phi = 0.1$ are similar to β_ζ and θ_ζ in (34), respectively. The variable $\boldsymbol{\sigma}^1$ is the infinitesimal stress tensor (associated with W in (4)) expressed as

$$\boldsymbol{\sigma}^1(\boldsymbol{\epsilon}) = \bar{\kappa} \text{tr}(\boldsymbol{\epsilon})\mathbf{I} + 2\bar{\mu} \text{dev}(\boldsymbol{\epsilon}),$$

and $\boldsymbol{\epsilon}$ is the infinitesimal strain tensor defined as

$$\boldsymbol{\epsilon}(\mathbf{F}) = \frac{1}{2} (\mathbf{F} + \mathbf{F}^\top) - \mathbf{I}.$$

Remark 3. The physical meaning of $\check{\mathbf{P}}$ in (36) merits explicit clarification. For solid materials where $\bar{\rho}(\mathbf{X}) = 1$ and therefore $\phi(\mathbf{X}) = 1$, the variable $\check{\mathbf{P}}$ reduces to \mathbf{P} in (24) for elastoplastic materials exactly. For void materials where $\bar{\rho}(\mathbf{X}) = 0$ and therefore $\phi(\mathbf{X}) = 0$, the variable $\check{\mathbf{P}}$ reduces to $\boldsymbol{\sigma}^1$ for linear elastic materials exactly without any large deformations and yield behaviors (as in the air). This linear elasticity assumption for void materials brings negligible errors (as verified in [Appendix F](#)) due to the tiny stiffness of void materials compared to solid ones.

Corresponding to the interpolated first Piola–Kirchhoff stress ($\check{\mathbf{P}}$) in (36), we compute the interpolated first elastoplastic moduli as

$$\check{\mathbf{C}} = \frac{\partial \check{\mathbf{P}}}{\partial \mathbf{F}} = \phi^2 \hat{\mathbf{C}}(\check{\mathbf{F}}) + (1 - \phi^2) \mathbf{C}^1,$$

where \mathbb{C}^1 represents the tangent moduli of the associated linear elastic material expressed as

$$\mathbb{C}^1 \equiv \bar{\kappa} \mathbf{I} \otimes \mathbf{I} + 2\bar{\mu} \left(\mathbb{I} - \frac{1}{3} \mathbf{I} \otimes \mathbf{I} \right).$$

Consequently, the integrand of the left-hand side of the global incremental equilibrium equation in (32)₁ becomes as

$$\nabla \mathbf{v} : \check{\mathbb{C}} : \nabla \delta \mathbf{u} = \phi^2 \nabla \mathbf{v} : \hat{\mathbb{C}}(\check{\mathbf{F}}) : \nabla \delta \mathbf{u} + (1 - \phi^2) \nabla \mathbf{v} : \mathbb{C}^1 : \nabla \delta \mathbf{u}. \quad (37)$$

Note that one can effortlessly compute $\nabla \mathbf{v} : \hat{\mathbb{C}}(\check{\mathbf{F}}) : \nabla \delta \mathbf{u}$ by replacing \mathbf{F} with $\check{\mathbf{F}}$ in (33). As for the second term in (37), we write out

$$\nabla \mathbf{v} : \mathbb{C}^1 : \nabla \delta \mathbf{u} = \left(\bar{\kappa} - \frac{2\bar{\mu}}{3} \right) \text{tr}(\nabla \delta \mathbf{u}) \text{tr}(\nabla \mathbf{v}) + 2\bar{\mu} (\nabla \delta \mathbf{u})^{\text{sym}} : \nabla \mathbf{v}.$$

Finally, substituting the interpolation rules in (35), (36), and (37) into (32) yields the parameterized global equilibrium equations, from which one can solve for the structural elastoplastic responses with various structural geometries and material phases.

3.3. Topology optimization formulation

Once deriving the parameterized global equilibrium equations, we can present the topology optimization formulation as

$$\left\{ \begin{array}{l} \text{maximize:} \\ \rho, \xi_1, \dots, \xi_{N^{\text{mat}}} \end{array} \right. J(\bar{\rho}, \bar{\xi}_1, \dots, \bar{\xi}_{N^{\text{mat}}}; \mathbf{u}_1, \dots, \mathbf{u}_N; \bar{\mathbf{b}}_1^e, \dots, \bar{\mathbf{b}}_N^e; \bar{\beta}_1, \dots, \bar{\beta}_N; \alpha_1, \dots, \alpha_N; \hat{\gamma}_1, \dots, \hat{\gamma}_N);$$

$$\left\{ \begin{array}{l} \text{subject to:} \\ \left\{ \begin{array}{l} g_{V0} = \frac{1}{|\Omega_0|} \int_{\Omega_0} \bar{\rho}(\mathbf{X}) d\mathbf{X} - \bar{V} \leq 0; \\ g_{Vn} = \frac{1}{|\Omega_0|} \int_{\Omega_0} \bar{\rho}(\mathbf{X}) \bar{\xi}_n(\mathbf{X}) d\mathbf{X} - \bar{V}_n \leq 0 \quad \text{for } n = 1, 2, \dots, N^{\text{mat}}; \\ g_{\Psi} = \frac{1}{|\Omega_0|} \int_{\Omega_0} \bar{\rho}(\mathbf{X}) \sum_{n=1}^{N^{\text{mat}}} [\bar{\xi}_n(\mathbf{X}) \Psi_n] d\mathbf{X} - \bar{\Psi} \leq 0 \quad \text{for } \Psi \in \{P, M, C\}; \\ \rho(\mathbf{X}), \xi_1(\mathbf{X}), \dots, \xi_{N^{\text{mat}}}(\mathbf{X}) \in [0, 1]; \end{array} \right. \end{array} \right. \quad (38)$$

$$\left\{ \begin{array}{l} \text{with:} \\ \left\{ \begin{array}{l} \text{Updating formulae for } \bar{\beta}_1, \dots, \bar{\beta}_N \text{ and } \alpha_1, \dots, \alpha_N \text{ in (16)}; \\ \text{Updating formulae for } \bar{\mathbf{b}}_1^e, \dots, \bar{\mathbf{b}}_N^e \text{ in (17)}; \\ \text{Kuhn-Tucker condition for } \hat{\gamma}_1, \dots, \hat{\gamma}_N \text{ in (21)}; \\ \text{Global equilibrium equations for } \mathbf{u}_1, \dots, \mathbf{u}_N \text{ in (32)}. \end{array} \right. \end{array} \right.$$

In these expressions, the variable J represents a general objective function to be maximized, with its detailed formulation to be introduced later. The parameter N represents the maximum load steps in FEA. The constraints g_{V0} and g_{Vn} , for $n = 1, 2, \dots, N^{\text{mat}}$, correspond to the total material volume fraction (with an upper bound $\bar{V} \in (0, 1]$) and the volume fraction of material n (with an upper bound $\bar{V}_n \in [0, \bar{V}]$), respectively. Additionally, the constraints g_P , g_M , and g_C impose limits on price, mass density, and CO₂ footprint, respectively, with \bar{P} , \bar{M} , and \bar{C} representing their respective upper bounds. The parameters P_n , M_n , and C_n denote the price, mass density, and CO₂ footprint of material n , respectively.

In this study, we aim to optimize the structural performance metrics of stiffness, strength, and effective structural toughness (through total energy). Following the footprint of Jia et al. (2023, 2025), we design a comprehensive multi-objective function for finite strain elastoplasticity as

$$J = w_{\text{stiff}} J_{\text{stiff}} + w_{\text{force}} J_{\text{force}} + w_{\text{energy}} J_{\text{energy}}. \quad (39)$$

Here, w_{stiff} , w_{force} , and $w_{\text{energy}} \in [0, 1]$ are weighting factors subject to $w_{\text{stiff}} + w_{\text{force}} + w_{\text{energy}} = 1$. The energy-type variables J_{stiff} , J_{force} , and J_{energy} represent stiffness, strength (end force), and structural toughness (total energy), respectively, and are defined as

$$\begin{cases} J_{\text{stiff}} = \frac{1}{2} \int_{\Omega_0} \check{\mathbf{P}}_1 : \nabla \mathbf{u}_1 d\mathbf{X}, & J_{\text{force}} = \int_{\Omega_0} \check{\mathbf{P}}_N : \nabla \mathbf{u}_N d\mathbf{X}, \\ J_{\text{energy}} = \frac{1}{2} \sum_{n=1}^N \int_{\Omega_0} (\check{\mathbf{P}}_n + \check{\mathbf{P}}_{n-1}) : (\nabla \mathbf{u}_n - \nabla \mathbf{u}_{n-1}) d\mathbf{X}. \end{cases} \quad (40)$$

Recall that \mathbf{u}_n and $\check{\mathbf{P}}_n$ for $n = 1, 2, \dots, N$ are the displacement and interpolated first Piola–Kirchhoff stress at load step n , respectively. The terms J_{stiff} , J_{force} , and J_{energy} in (40) are interpreted as follows.

- The variable J_{stiff} represents the strain energy at the first load step, where plasticity has not yet evolved. Under displacement loading, J_{stiff} is positively correlated with the initial stiffness of the structure. Therefore, maximizing J_{stiff} enhances structural stiffness.
- The variable J_{force} corresponds to the product of force and displacement at the final load step, also known as the “end compliance” for hyperelastic structures. Under displacement loading, maximizing J_{force} increases the final reaction force.
- Finally, the variable J_{energy} captures the total energy absorption and dissipation of the structure, equivalent to the area enclosed by its force–displacement curve.

Remark 4. In the multi-objective function in (39), we opt to use the (interpolated) first Piola–Kirchhoff stress ($\check{\mathbf{P}}$) as the primary measure in contrast to the Kirchhoff stress ($\hat{\boldsymbol{\tau}}$) in Section 2. It is because $\check{\mathbf{P}}$ is the easiest stress measure (Kumar and Lopez-Pamies, 2020) to gauge practically. However, we note that the multi-objective function in (39) is general, and one can effortlessly replace $\check{\mathbf{P}}$ with any other stress measures if desired.

Remark 5. The proposed topology optimization formulation in (38) equipped with the general multi-objective function in (39) can be simplified to recover several special cases that have demonstrated success. For example, setting $w_{\text{stiff}} = w_{\text{energy}} = 0$ and $w_{\text{force}} = 1$ yields $J = J_{\text{force}}$, which mainly maximizes the “end compliance” as in Ivarsson et al. (2021). Similarly, setting $w_{\text{stiff}} = w_{\text{force}} = 0$ and $w_{\text{energy}} = 1$ derives $J = J_{\text{energy}}$, which primarily maximizes the energy of structures as in Wallin et al. (2016). Additionally, employing $w_{\text{stiff}} = 0$ and $w_{\text{force}} = w_{\text{energy}} = 0.5$ generates $J = 0.5J_{\text{force}} + 0.5J_{\text{energy}}$ as in Abueidda et al. (2021). As illustrated in Section 4, utilizing the comprehensive multi-objective function in (39) enables the generation of optimized structures exhibiting diverse and tailored elastoplastic responses under large deformations.

4. Optimized elastoplastic designs with real-world applications

In this section, we present optimized elastoplastic designs with real-world applications through four representative examples. These examples demonstrate the effectiveness of the proposed multimaterial topology optimization framework (Section 3) in optimizing structural elastoplastic responses under large deformations. Additionally, we provide mechanical insights into achieving these optimized behaviors.

In the first example, we optimize the energy dissipation of multi-alloy dampers subjected to various cyclic loadings. This investigation reveals that employing multiple materials enhances energy dissipation compared to single-material ones under large deformations. Additionally, we demonstrate the transition from the kinematic hardening dominance to the isotropic hardening dominance, which improves energy dissipation as applied displacements increase. We also show that optimized dampers exhibit superior energy dissipation across multiple loading cycles compared to an intuitive design.

In the second example, we optimize the initial stiffness and end force of double-clamped beams. This example demonstrates the versatility of the proposed topology optimization framework in handling multiple

design objectives for structures made of purely hyperelastic, purely elastoplastic, and mixed materials. We also explore the synergistic use of hyperelastic and elastoplastic materials to achieve various stiffness–strength interplays in composite structures.

In the third example, we maximize the crashworthiness of impact-resisting bumpers. Extending the optimization task to 3D geometries, we consider scenarios with more than two candidate materials. Through this example, we show that the proposed optimization framework applies to various spatial dimensions and an arbitrary number of candidate materials.

Finally, we optimize the end force of cold working profiled sheets accounting for both the processing (metal-forming) and service (load-carrying) stages, which involve ultra-large elastoplastic deformations. This example introduces multi-stage topology optimization, which incorporates both intra-stage and inter-stage history dependencies. Additionally, we integrate practical constraints — cost, lightweight, and sustainability — into the design and optimization of elastoplastic structures, bridging the gap between mechanical designs and non-mechanical considerations.

We remark that these examples span a spectrum of material properties, as summarized in Table 1. For most examples, we consistently use titanium, bronze, nickel–chromium, and stainless steel, which exhibit perfect plasticity, linear isotropic hardening, nonlinear isotropic hardening, and kinematic hardening, respectively. Importantly, these four materials can be joined together using 3D printing techniques, as reported in Wei et al. (2020, 2022). In the double-clamped beam example, we utilize elastoplastic lithium, characterized by combined isotropic and kinematic hardening, alongside hyperelastic PCL, modeled by assigning a sufficiently large yield strength of $\sigma_y = 25$ MPa.

Table 1: Material properties used in numerical examples

| Materials | Titanium (Ti–6Al–4V) | Bronze (CuSn10) | Nickel –chromium (INCONEL 718) | Stainless steel (AISI 316L) | Lithium (commercial purity) | PCL (polycapro- -lactone) |
|--------------------------------------------------|-------------------------|----------------------------|----------------------------------------------------|--------------------------------|-----------------------------------|---------------------------------|
| Features | Perfect plasticity | Linear isotropic hardening | Nonlinear isotropic hardening | Kinematic hardening | Combined hardening | Near hyperelasticity |
| Bulk moduli, κ (GPa) | 115.6 | 88.9 | 165.0 | 141.3 | 5.8 | 0.3880 |
| Shear moduli, μ (GPa) | 41.4 | 29.6 | 76.2 | 76.8 | 1.8 | 0.0157 |
| Young’s moduli, E (GPa) | 111.0 | 80.0 | 198.0 | 195.0 | 4.9 | 0.0466 |
| Poisson’s ratios, ν | 0.34 | 0.35 | 0.30 | 0.27 | 0.36 | 0.48 |
| Kinematic hardening moduli, h (MPa) | 0.0 | 0.0 | 0.0 | 1339.1 | 2.5 | 0.0 |
| Isotropic hardening moduli, K (MPa) | 0.0 | 952.0 | 129.0 | 0.0 | 2.5 | 0.0 |
| Initial yield strengths, σ_y (MPa) | 853.0 | 145.0 | 450.0 | 226.0 | 1.0 | 25.0 |
| Residual yield strengths, σ_∞ (MPa) | 853.0 | 145.0 | 715.0 | 226.0 | 1.0 | 25.0 |
| Saturation exponents, δ | 0.0 | 0.0 | 16.9 | 0.0 | 0.0 | 0.0 |
| Isotropic hardening functions, $k(\alpha)$ (MPa) | 853.0 | $145.0 + 952.0\alpha$ | $450.0 + 129.0\alpha + 265.0(1 - e^{-16.9\alpha})$ | 226.0 | $1.0 + 2.5\alpha$ | 25.0 |
| Price (USD/kg) | 24.4 | 13.3 | 25.2 | 6.6 | 127.0 | 6.8 |
| Mass densities (10^3 kg/m ³) | 4.4 | 8.8 | 8.2 | 8.0 | 0.5 | 1.1 |
| CO ₂ footprint (kg/kg) | 40.4 | 6.0 | 16.6 | 7.4 | 79.6 | 2.3 |

To implement the proposed topology optimization framework, we adapt the open-source software¹ (Jia et al., 2024d) to incorporate finite strain elastoplasticity. The software efficiently computes partial derivatives using automatic differentiation and accelerates computations through parallel processing. To ensure high solution precision, we utilize a direct solver with lower–upper factorization to solve the global equilibrium equations in (32) and the adjoint equations in (E.4)–(E.5). Additionally, to determine the optimal design variables, we employ the well-established gradient-based optimizer, the method of moving asymptotes (Svanberg, 1987). This optimizer utilizes the sensitivity analysis presented in Appendix E and efficiently updates the design variables until convergence. The optimized elastoplastic structures and the mechanisms enabling these design objectives are detailed below.

4.1. Metallic yielding dampers with maximized hysteretic energy

4.1.1. Single-alloy versus multi-alloy dampers

In this subsection, we optimize the energy dissipation of metallic dampers (Zhang et al., 2018; Jia et al., 2022), which are typically used in structural engineering to suppress vibrations induced by earthquakes or winds. Through these optimized dampers, we aim to demonstrate the effectiveness of the proposed topology optimization framework in optimizing structural elastoplastic responses under large deformations. Additionally, we highlight the necessity of employing multiple alloys to achieve greater energy dissipation.

To achieve these goals, we revisit the damper optimization problem in Jia et al. (2025). As shown in Fig. 4(a), the design domain is a rectangle subjected to simple shear loadings under the plane strain condition. We aim to optimally distribute the bronze and steel materials, whose Kirchhoff stress–Lagrangian strain (τ_{11} – E_{11}) curves are shown in Fig. 4(b), to maximize the total hysteretic energy (Fig. 4(c)). Notably, the current setup incorporates non-monotonic, cyclic loadings and accounts for large deformations, representing a more complex scenario compared to the original problem in Jia et al. (2025).

To solve this problem, we employ the following FEA and optimization strategies. The design domain is discretized using a structured mesh consisting of 15,000 first-order quadrilateral elements. The filter radius is set to $R_\zeta = 10$ mm for $\zeta \in \{\rho, \xi_1, \dots, \xi_{N_\xi}\}$. The Heaviside sharpness parameter, β_ζ , is initially set to 1 and is doubled every 40 optimization iterations starting from iteration 41, until it reaches a maximum value of $\beta_\zeta = 512$. The penalty parameters for the density variable are fixed at $p_\kappa = p_\mu = p_h = 3$ and $p_k = 2.5$, while the penalty parameter for the material variables, p_ξ , starts at 1 and increases by 0.25 every 40 optimization iterations from iteration 41, up to a maximum of $p_\xi = 3$. The weighting factors in (39) are set as $w_{\text{stiff}} = w_{\text{force}} = 0$ and $w_{\text{energy}} = 1$. The constraint is defined by the total material volume, $g_{V0} \leq 0$, with an upper bound of $\bar{V} = 0.5$. The maximum number of optimization iterations is set to 500. During the topology optimization process, we use 32 non-uniform load steps in the FEA. Following optimization, we refine the analysis by using 44 load steps to evaluate the elastoplastic responses of all designs.

The damper designs under half-cycle loadings, along with the hysteretic energy (Π in kN·m), are illustrated in Fig. 4(d). As a baseline, we include one intuitive composite design that uses the same material volume fraction ($\bar{V} = 0.5$) as the three optimized designs. These optimized designs are tailored for bronze, steel, and multiple materials, respectively. Compared to the intuitive composite design, the three optimized dampers achieve greater hysteretic energy, with increases of 4.58%, 3.19%, and 10.15%, respectively. These improvements highlight the effectiveness of the proposed topology optimization framework in enhancing elastoplastic responses under large deformations. Moreover, the optimized composite design naturally favors the use of two materials and achieves higher energy dissipation than the two single-material optimized designs. This performance gain aligns with the infinitesimal strain scenario in Jia et al. (2025) and reinforces the benefit of using multiple materials to improve design performance under large deformations.

To understand the performance gains, we present the normalized equivalent plastic strain ($\alpha/\max(\alpha)$) for all dampers in Fig. 4(e). In the intuitive composite design, plastic strain is confined to the central region, whereas the three optimized designs distribute plastic deformation more evenly, allowing a greater portion of the material to effectively contribute to total energy dissipation. Further, by examining the Kirchhoff

¹Available in GitHub at <https://github.com/missionlab/fenitop>.

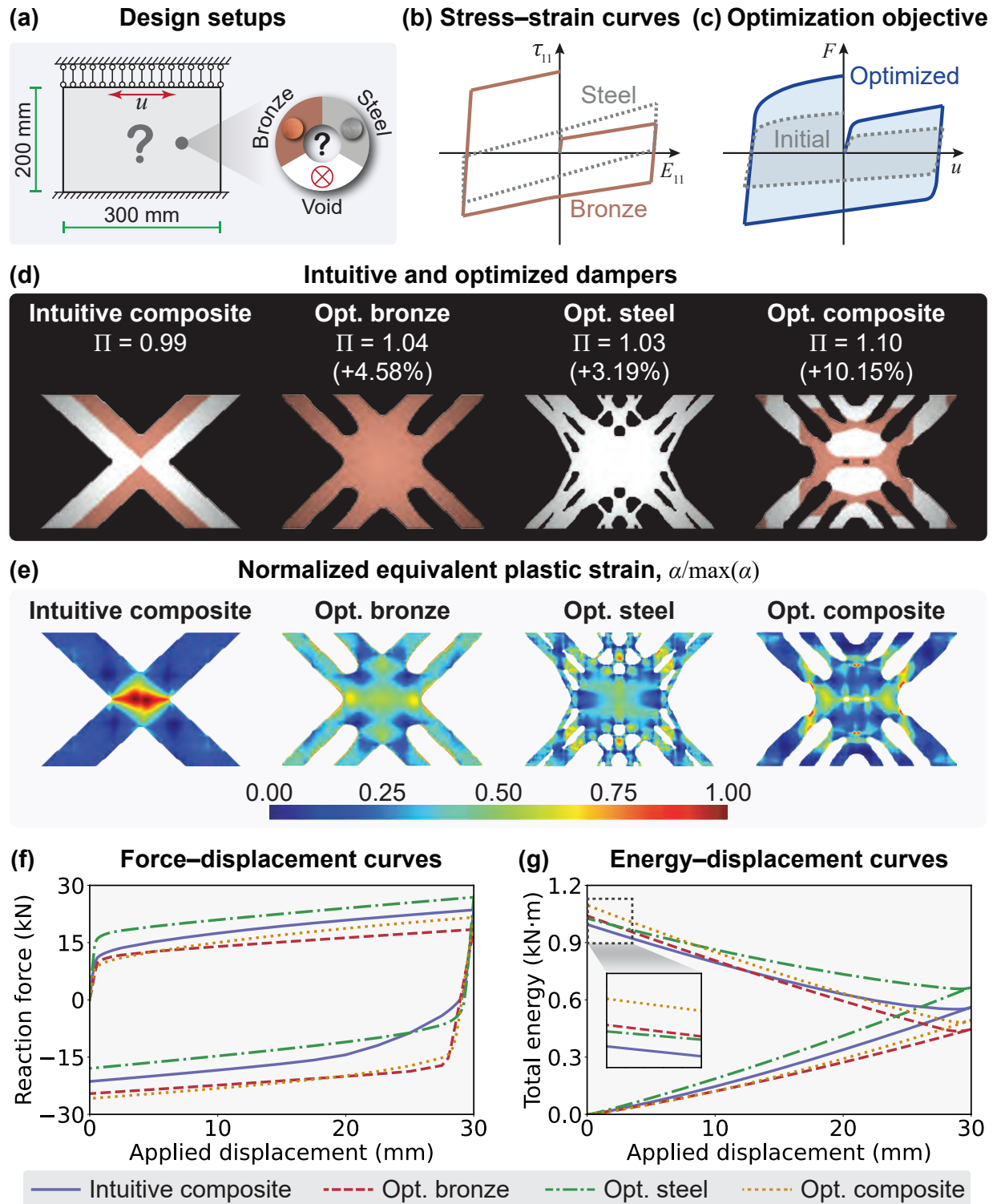


Figure 4: Design and optimization of metallic yielding dampers. (a) Design setups: the design domain, boundary conditions, and candidate materials (bronze, steel, and void). The variable u is the applied displacement. (b) Uniaxial Kirchhoff stress–Lagrangian strain (τ_{11} – E_{11}) curves of candidate materials. (c) Optimization objective: maximizing the total energy of dampers. The variable F is the reaction force. (d) Intuitive and optimized dampers. The total energy (Π) is in $\text{kN}\cdot\text{m}$. The percentages are the total energy increments compared to the intuitive design. (e) Normalized equivalent plastic strain ($\alpha/\max(\alpha)$). (f) Force–displacement (F – u) curves. (g) Energy–displacement (Π – u) curves.

stress–Lagrangian strain (τ_{11} – E_{11}) curves in Fig. 4(b), we observe that the steel material dissipates more energy during the first quadrant (loading stage), while the bronze material dissipates more energy during the fourth quadrant (unloading stage). This difference in energy dissipation between materials is manifested in the dissimilar hysteretic loops of the force–displacement (F – u) curves for the optimized bronze and steel designs (Fig. 4(f)). In contrast, the optimized composite damper effectively utilizes both materials to balance energy dissipation during the loading and unloading stages, forming the largest hysteresis loop, which ultimately results in the highest total energy dissipation shown in Fig. 4(g).

4.1.2. Dampers under complete cyclic loadings with increasing displacement amplitudes

Having demonstrated the effectiveness of the topology optimization framework and the necessity of employing multiple materials, we now evaluate the performance of optimized composite dampers under complete cyclic loadings with increasing displacement amplitudes. As shown in Fig. 5(a), we present three optimized dampers with applied displacement amplitudes of $u_{\max} = 10, 20,$ and 30 mm, respectively. For each optimized damper, we report the total energy (Π) and its increment compared to the intuitive design in Fig. 4(d). All three optimized dampers demonstrate performance gains — 20.25%, 17.28%, and 18.60%, respectively — relative to the intuitive design. These gains are attributed to the optimized dampers’ ability to engage more materials in energy dissipation, as evidenced by the normalized total energy density ($W/\max(W)$) in Fig. 5(c). Notably, these performance improvements exceed the 10.15% gain achieved by the optimized composite damper under half-cycle loadings (Fig. 4(d)). This enhanced performance is due to the full-cycle optimized designs achieving significant energy increases in the second quadrant (reloading stage), despite slight energy decreases in the first quadrant (loading stage) for $u_{\max} = 20$ and 30 mm, as shown in Fig. 5(b) and (c).

A comparison among the three optimized designs in Fig. 5(a) further reveals the influence of displacement amplitude (u_{\max}) on material distribution. As displacement amplitudes increase, the optimized dampers increasingly favor the use of bronze over steel. This trend can be explained by the material behaviors illustrated in the Kirchhoff stress–Lagrangian strain (τ_{11} – E_{11}) curves in Fig. 4(b). The steel material, which exhibits kinematic hardening, produces a hysteretic loop approximating a parallelogram. Its total energy density is expressed as

$$W^s \approx 4\sigma_y^s E_{\max} \quad (41)$$

where σ_y^s is the yield strength of steel and E_{\max} is the Lagrangian strain amplitude. In contrast, the hysteretic loop of the bronze material expands with larger strains due to isotropic hardening, with its total energy density given by

$$W^b \approx 2E_{\max} [\sigma_y^b + (\sigma_y^b + 4E_t^b E_{\max})] = 8E_t^b E_{\max}^2 + 4\sigma_y^b E_{\max} \quad (42)$$

where σ_y^b and $E_t^b > 0$ are the yield strength and average plastic tangent modulus of bronze, respectively. At small strains, W^b is dominated by the linear term, with $W^b \rightarrow 4\sigma_y^b E_{\max} < W^s$ as $E_{\max} \rightarrow 0$. At larger strains, W^b is dominated by the quadratic term, with $W^b \rightarrow 8E_t^b E_{\max}^2 > W^s$ as $E_{\max} \rightarrow \infty$. Consequently, as E_{\max} (and u_{\max}) increases, the optimized dampers gradually favor bronze over steel.

We also note that these findings are specific to the context of large deformations, where both the materials (Fig. 4(b)) and structures (Fig. 5(b)) yield immediately upon loading. Therefore, the transition from kinematic to isotropic hardening — rather than the stiffness-to-strength transition observed in the infinitesimal strain scenario (Jia et al., 2025) — dominates the material distribution in the optimized dampers.

4.1.3. Dampers under multiple-cycle loadings

Practically, energy-dissipating dampers are subjected to multiple-cycle loadings with non-constant displacement amplitudes (Zhang et al., 2018; Jia et al., 2019, 2021, 2022). In this subsection, we apply such complex loading conditions and evaluate the total energy of the optimized damper. As shown in Fig. 6(a), we compare the intuitive design from Fig. 4(d) with a damper optimized under multiple-cycle loadings. The optimized design exhibits an organic material distribution and achieves a total energy increase of 32.84%, rising from 4.45 kN·m in the intuitive design to 5.91 kN·m.

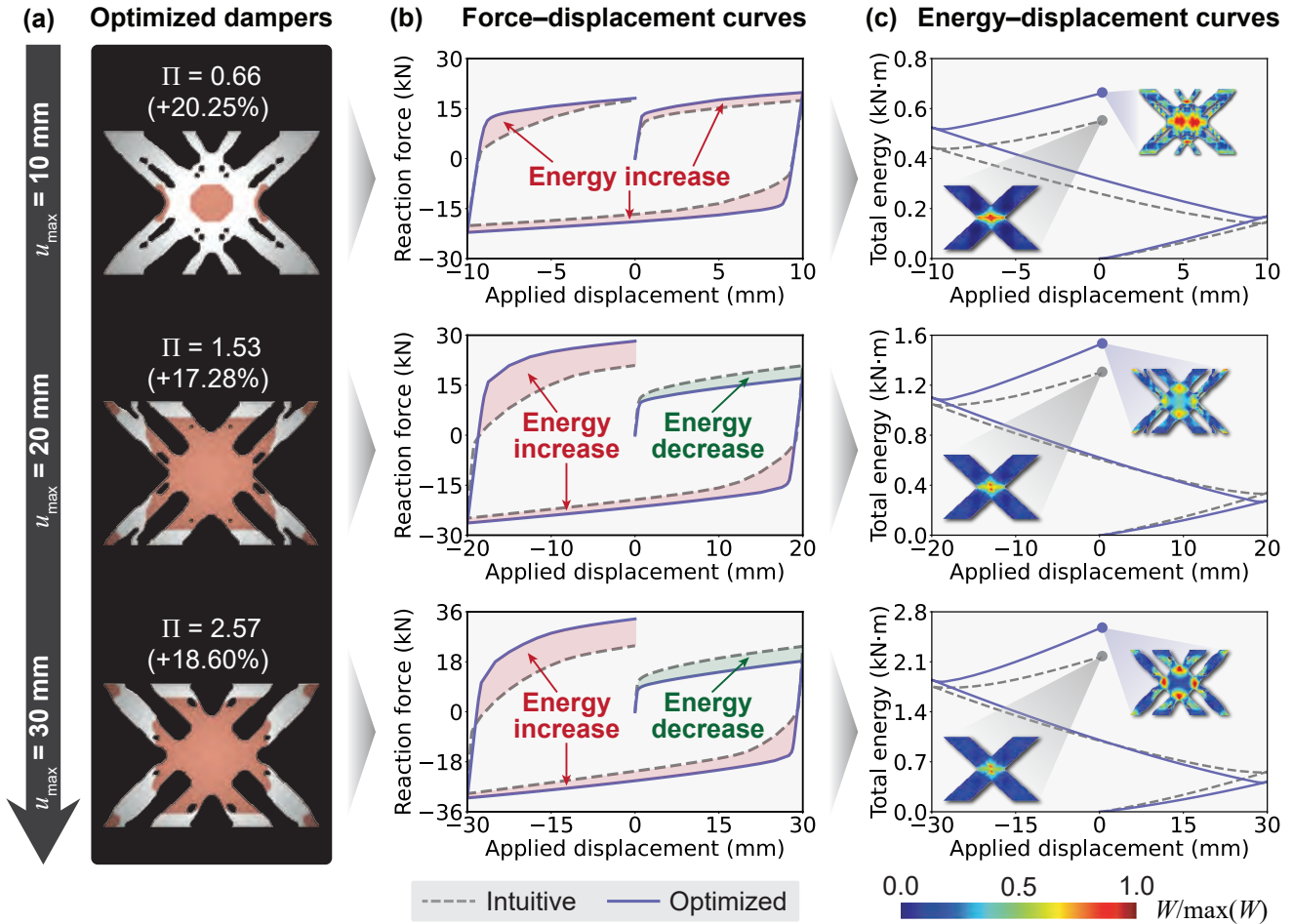


Figure 5: Optimized dampers under increasing applied displacements. (a) Optimized dampers. The total energy (Π) is in kN·m, and the percentages are the total energy increments compared to the intuitive design in Fig. 4(d). (b) Force-displacement ($F-u$) curves. (c) Energy-displacement ($\Pi-u$) curves. The insets are the normalized total energy density ($W/\max(W)$) at the final load step.

The force–displacement (F – u) and energy–displacement (Π – u) curves of the two designs are shown in Fig. 6(b) and (c), respectively. In Fig. 6(b), each force–displacement curve consists of 166 non-uniform load steps and spans three cycles with increasing displacement amplitudes of 10, 20, and 30 mm. Compared to the intuitive design, the optimized damper demonstrates a slightly smaller hysteresis loop during the first cycle but more expanded loops in the second and third cycles. Here is why.

Based on (41), the total energy densities of steel during the three cycles are expressed as

$$W_1^s \approx 4\sigma_y^s E_{1,\max}, \quad W_2^s \approx 4\sigma_y^s E_{2,\max}, \quad \text{and} \quad W_3^s \approx 4\sigma_y^s E_{3,\max}$$

where W_i^s for $i = 1, 2, 3$ is the total energy density of steel during cycle i , and $E_{i,\max}$ is the strain amplitude of that cycle. Similarly, based on (42), the total energy densities of bronze during the three cycles are

$$\left\{ \begin{array}{l} W_1^b \approx 2E_{1,\max} [\sigma_y^b + (\sigma_y^b + 4E_t^b E_{1,\max})] = 8E_t^b E_{1,\max}^2 + 4\sigma_y^b E_{1,\max} \\ W_2^b \approx 2E_{2,\max} \{(\sigma_y^b + 4E_t^b E_{1,\max}) + [\sigma_y^b + 4E_t^b (E_{1,\max} + E_{2,\max})]\} \\ \quad = 8E_t^b E_{2,\max}^2 + 4\sigma_y^b E_{2,\max} + 16E_t^b E_{1,\max} E_{2,\max} \\ W_3^b \approx 2E_{3,\max} \{[\sigma_y^b + 4E_t^b (E_{1,\max} + E_{2,\max})] + [\sigma_y^b + 4E_t^b (E_{1,\max} + E_{2,\max} + E_{3,\max})]\} \\ \quad = 8E_t^b E_{3,\max}^2 + 4\sigma_y^b E_{3,\max} + 16E_t^b E_{1,\max} E_{3,\max} + 16E_t^b E_{2,\max} E_{3,\max} \end{array} \right.$$

where W_i^b for $i = 1, 2, 3$ is the total energy density of bronze during cycle i . Given that $E_{1,\max} < E_{2,\max} < E_{3,\max}$, we observe $W_1^s < W_2^s < W_3^s$ and $W_1^b < W_2^b < W_3^b$. This progression indicates that the total energy contributions increase across successive cycles. Consequently, the optimized damper contracts the force–displacement curve and sacrifices the total energy during the first cycle. However, it compensates by expanding the force–displacement curves and increasing total energy during the second and third cycles. Eventually, the optimized damper shows greater end energy than the intuitive design (Fig. 6(c)), demonstrating its superior performance under multiple-cycle loading.

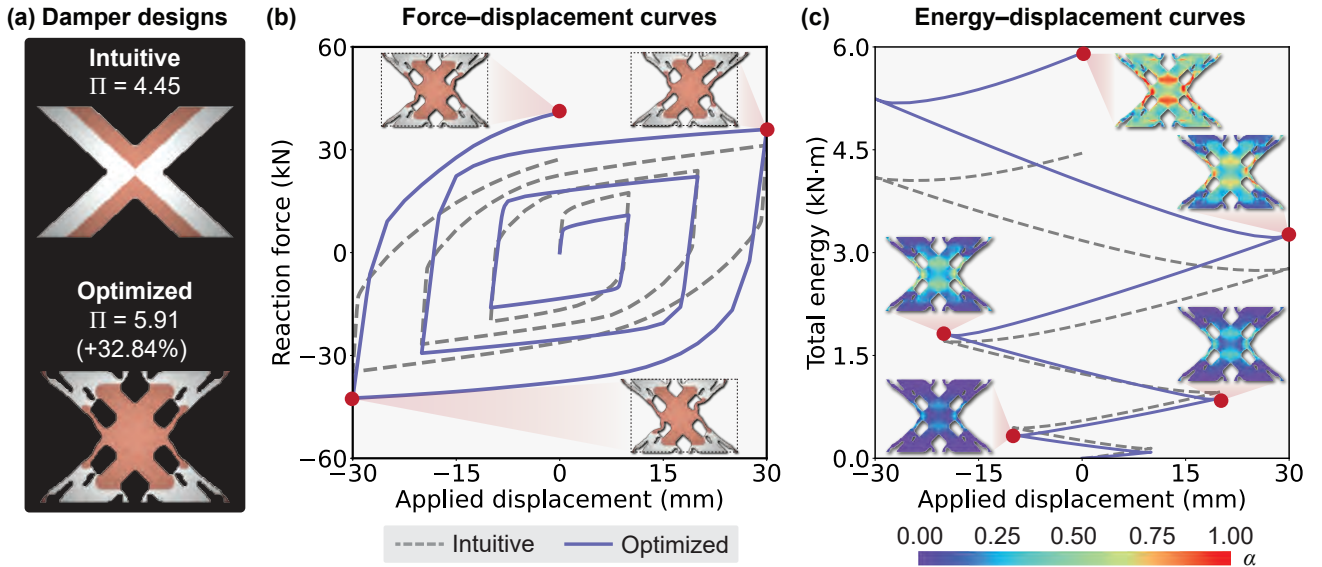


Figure 6: Dampers under multiple cycles of loadings. (a) Damper designs. The total energy (Π) is in kN·m, and the percentage is the total energy increment compared to the intuitive design. (b) Force–displacement (F – u) curves. The insets are the deformed configurations of the optimized damper. (c) Energy–displacement (Π – u) curves. The insets are the equivalent plastic strains (α), and the values above 1 are plotted as 1 for better visualization.

Through this example of optimizing metallic yielding dampers, we numerically prove the effectiveness of the proposed multimaterial topology optimization framework in enhancing elastoplastic responses of structures under large deformations. Exploiting this framework, we present a series of optimized dampers with superior energy dissipation compared to an intuitive design, irrespective of the applied loading conditions,

including half-cycle, complete-cycle, and multiple-cycle loadings. Furthermore, we highlight the necessity of employing multiple materials to improve the energy dissipation of the optimized dampers. Our analysis also reveals key phenomena, such as the transition from kinematic to isotropic hardening under complete-cycle loadings with increasing displacement amplitudes and the dominance of later cycles over initial cycles in multiple-cycle loadings. Together with the framework for infinitesimal strain elastoplasticity in [Jia et al. \(2025\)](#), this study completes a comprehensive narrative for optimizing energy-dissipating devices.

4.2. Hyperelastic–elastoplastic composite structures with tailored stiffness–strength balance

In this example, we design and optimize composite structures composed of both hyperelastic and elastoplastic materials. These optimized designs showcase various stiffness–strength interplays by harnessing the complementary properties of elasticity and plasticity. Additionally, we demonstrate the versatility of the proposed topology optimization framework in optimizing material distributions across a range of configurations, including purely hyperelastic, purely elastoplastic, and mixed-material systems.

The design setups are shown in Fig. 7(a). We optimize a double-clamped beam, where the top middle edge is subjected to a downward displacement, u . The design objective is to distribute hyperelastic PCL and elastoplastic lithium, whose Kirchhoff stress–Lagrangian strain (τ_{11} – E_{11}) curves are shown in Fig. 7(b), to simultaneously maximize the initial stiffness and end force of the structures (Fig. 7(c)).

To achieve the design objective, we employ the following FEA and optimization treatments. The design domain is discretized using a structured mesh of 14,400 first-order quadrilateral elements. The filter radius is set to $R_\rho = 1$ mm for the density variable (ρ) and $R_\zeta = 3$ mm for $\zeta \in \{\xi_1, \dots, \xi_{N\xi}\}$. The Heaviside sharpness parameter (β_ζ) is initialized at 1 and doubled every 20 optimization iterations starting from iteration 21 until it reaches a maximum value of $\beta_\zeta = 512$. The penalty parameters for the density variable are fixed at $p_\kappa = p_\mu = p_h = p_k = 3$, while the penalty parameter for the material variables (p_ξ) starts at 1 and increases by 0.25 every 20 optimization iterations from iteration 21, up to a maximum of $p_\xi = 5$. The constraint is defined by the total material volume ($g_{V0} \leq 0$) with an upper bound of $\bar{V} = 0.5$. The maximum number of optimization iterations is set to 500. For performance evaluation using FEA, we consistently apply 18 non-uniform load steps across all designs.

The optimized beams and their deformations are shown in Fig. 7(d). We present four optimized bi-material designs (Dsgs. 2–5) with decreasing weighting ratios of initial stiffness ($w_{\text{stiff}} = 0.30, 0.25, 0.20,$ and 0.05 , respectively) and increasing weighting ratios of end force ($w_{\text{force}} = 0.70, 0.75, 0.80,$ and 0.95 , respectively). Additionally, two single-material designs are included as references: a lithium design (Dsg. 1) optimized for initial stiffness and a PCL design (Dsg. 6) optimized for the end force.

A comparison of Dsgs. 2–5 reveals a gradual shift in material preference as w_{stiff} decreases and w_{force} increases. The optimized designs progressively favor the hyperelastic PCL over the elastoplastic lithium. This trend is driven by the inherent properties of the materials: while metals like lithium are stiffer than polymers like PCL, lithium yields immediately under large deformations, with its Kirchhoff stress confined by the yield surface (Figs. 7(b) and (d)). In contrast, PCL’s hyperelastic behavior allows its Kirchhoff stress to increase rapidly under deformation. Consequently, lithium contributes more to stiffness and is preferred when w_{stiff} is larger, whereas PCL contributes more to the end force and is favored when w_{force} is larger.

These material contributions are further verified by the force–displacement curves in Fig. 7(e). As w_{stiff} decreases and w_{force} increases from Dsg. 2 to Dsg. 5, the initial stiffness diminishes while the peak force increases due to the greater incorporation of PCL in the optimized designs. Notably, the stiffness and peak force of the bi-material designs (Dsgs. 2–5) are bounded by the stiffness of the optimized lithium design (Dsg. 1) and the peak force of the optimized PCL design (Dsg. 6), respectively. Through these optimized designs, we demonstrate the generality of the proposed framework in optimizing structures composed of hyperelastic and/or elastoplastic materials under finite deformations. This generality enables tailoring stiffness–strength (end force) interplay for composite structures (Fig. 7(f)).

4.3. Front bumpers with maximized crashworthiness

In this subsection, we extend the optimization framework to 3D by maximizing the crashworthiness of impact-resisting front bumpers ([Patel et al., 2009](#); [Sun et al., 2018](#); [Wang et al., 2018](#); [Ren et al., 2020](#);

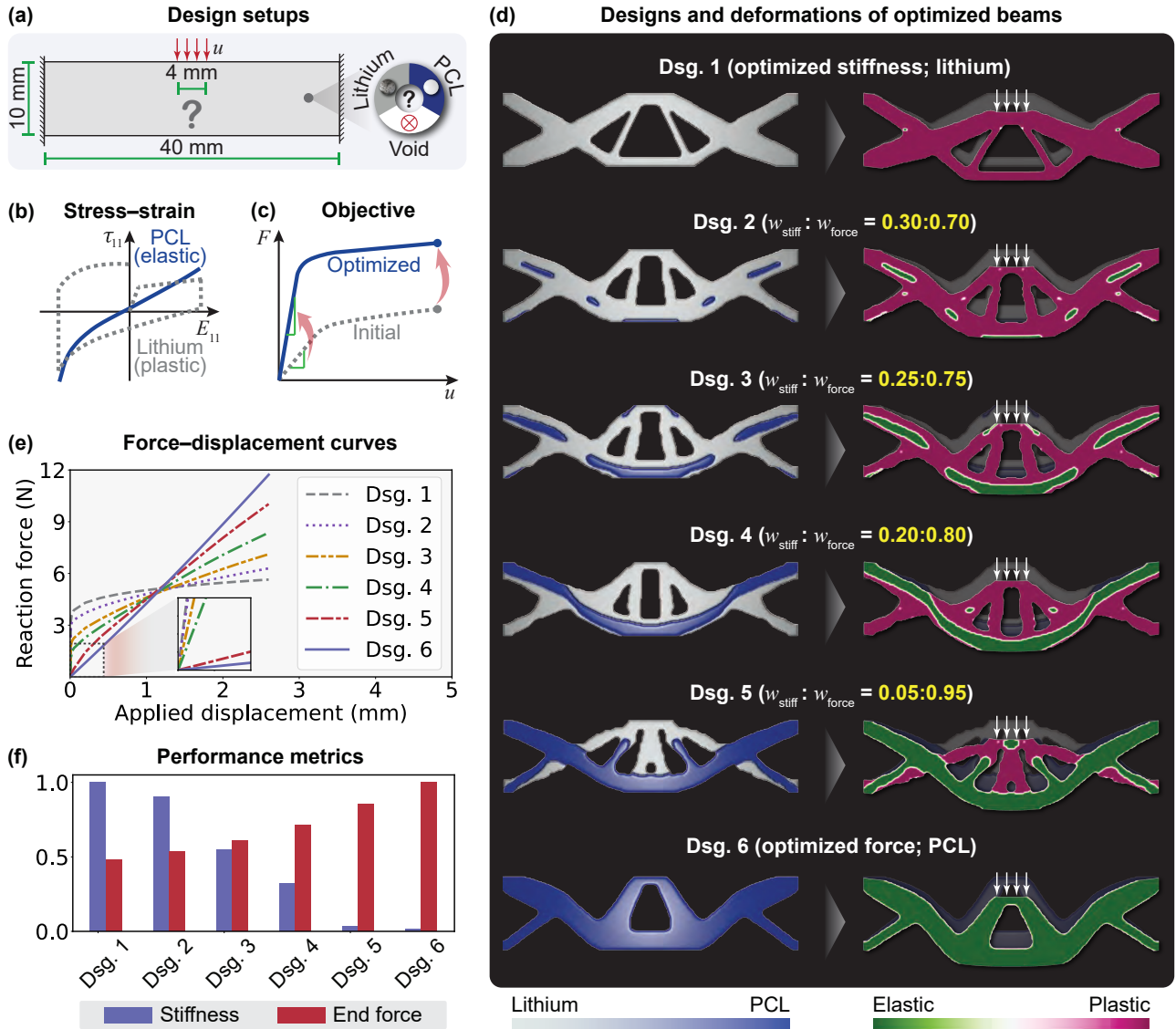


Figure 7: Design and optimization of double-clamped beams. (a) Design setups: the design domain, boundary conditions, and candidate materials (lithium, PCL, and void). The variable u is the applied displacement. (b) Uniaxial Kirchhoff stress–Lagrangian strain (τ_{11} – E_{11}) curves of candidate materials. (c) Optimization objective: maximizing the initial stiffness and end force of beams. The variable F is the reaction force. (d) Designs and deformations of optimized beams. The deformed configurations also show the elastic/plastic regions. (e) Force–displacement (F – u) curves. (f) Performance metrics of the initial stiffness and end force. The two metrics are normalized by the maxima of all designs, respectively.

Wang and Xie, 2020) and demonstrate its capability to handle more than two candidate materials.

4.3.1. Bi-material bumpers in 3D

As shown in Fig. 8(a), we consider an arch-shaped design domain with four fixed corners, subjected to quasi-static displacement loading (u). The design objective is to optimally distribute titanium, bronze, nickel–chromium, and steel, whose Kirchhoff stress–Lagrangian strain (τ_{11} – E_{11}) curves are shown in Fig. 8(b), to maximize the total energy — encompassing both elastic energy absorption and plastic energy dissipation — as shown in Fig. 8(c).

We begin by optimizing bi-material (titanium and bronze) bumpers in 3D, and FEA and optimization setups are as follows. The design domain is discretized using an unstructured mesh consisting of 138,400 first-order hexahedral elements. The filter radius is set to $R_\zeta = 40$ mm for $\zeta \in \{\rho, \xi_1, \dots, \xi_{N\xi}\}$. The Heaviside sharpness parameter, β_ζ , is initially set to 1 and is doubled every 40 optimization iterations starting from iteration 41 until it reaches a maximum value of $\beta_\zeta = 512$. The penalty parameters for the density variable are fixed at $p_\kappa = p_\mu = p_h = 3$ and $p_k = 2.5$, while the penalty parameter for the material variables, p_ξ , starts at 1 and increases by 0.25 every 40 optimization iterations from iteration 41, up to a maximum of $p_\xi = 3$. The weighting factors in (39) are set as $w_{\text{stiff}} = w_{\text{force}} = 0$ and $w_{\text{energy}} = 1$. The constraints include the total material volume ($g_{V0} \leq 0$) with an upper bound of $\bar{V} = 0.2$, and individual material volumes ($g_{V1} \leq 0$ and $g_{V2} \leq 0$) with upper bounds $\bar{V}_1 = \bar{V}_2 = 0.1$ to account for material availability. The maximum number of optimization iterations is set to 600. During the topology optimization process, we use 10 uniform load steps in the FEA. Following optimization, we refine the analysis by using 50 load steps to evaluate the elastoplastic responses of all designs.

The bi-material bumper designs are illustrated in Fig. 8(d). For comparison, we include an intuitive design as a reference, which shares the same total and individual material volumes as the optimized bumper. The comparison reveals that the optimized design favors an X-shaped part in the middle, in contrast to the I-shaped structure in the intuitive design. This X-shaped topology shortens load paths, thereby increasing structural stiffness and enhancing elastic energy absorption. Additionally, compared to the smooth members of the intuitive design, the optimized bumper features non-smooth, twisted regions that effectively concentrate stress, promoting localized material yielding and greater plastic energy dissipation.

Beyond the advantageous structural geometries, the optimized bumper also strategically distributes the material phases. By analyzing the material distribution in Fig. 8(d) alongside the elastic/plastic regions shown in Fig. 8(f), it is evident that the optimized design positions titanium primarily in elastic regions and bronze in plastic regions. This distribution aligns with the material properties illustrated in Fig. 8(b). Titanium, with its higher yield strength, remains in the elastic deformation regime, providing substantial elastic energy absorption. In contrast, bronze, with its lower yield strength, undergoes plastic deformation. Despite its lower initial strength, bronze exhibits isotropic hardening, allowing its Kirchhoff stress to increase progressively under loading. This behavior contrasts with the perfect plasticity (no hardening) of titanium, enabling bronze to dissipate certain plastic energy.

The combined effects of tailored structural geometries and material phases contribute to the better performance of the optimized bumper compared to the intuitive design. As shown in Fig. 8(e), the optimized bumper achieves a 105.41% increase in total energy (Π), rising from 1.74 to 3.57 kN·m, and a 129.24% improvement in end force, increasing from 44.49 to 101.98 kN. These performance gains are a direct result of the simultaneous optimization of density and material variables enabled by the proposed framework.

4.3.2. Tri-material and four-material bumpers

After demonstrating the effectiveness of the proposed framework in optimizing bi-material bumpers in 3D, we now extend the approach to optimize bumpers with more than two candidate materials. Specifically, we optimize tri-material bumpers composed of titanium, bronze, and nickel–chromium. The constraints include the total material volume ($g_{V0} \leq 0$) with an upper bound of $\bar{V} = 0.2$, and individual material volumes ($g_{V1} \leq 0$, $g_{V2} \leq 0$, and $g_{V3} \leq 0$) with equal upper bounds of $\bar{V}_1 = \bar{V}_2 = \bar{V}_3 = \bar{V}/3$.

The intuitive and optimized tri-material bumper designs are illustrated in Fig. 9(a). Similar to the optimized bi-material design shown in Fig. 8(d), the optimized tri-material bumper retains the X-shaped

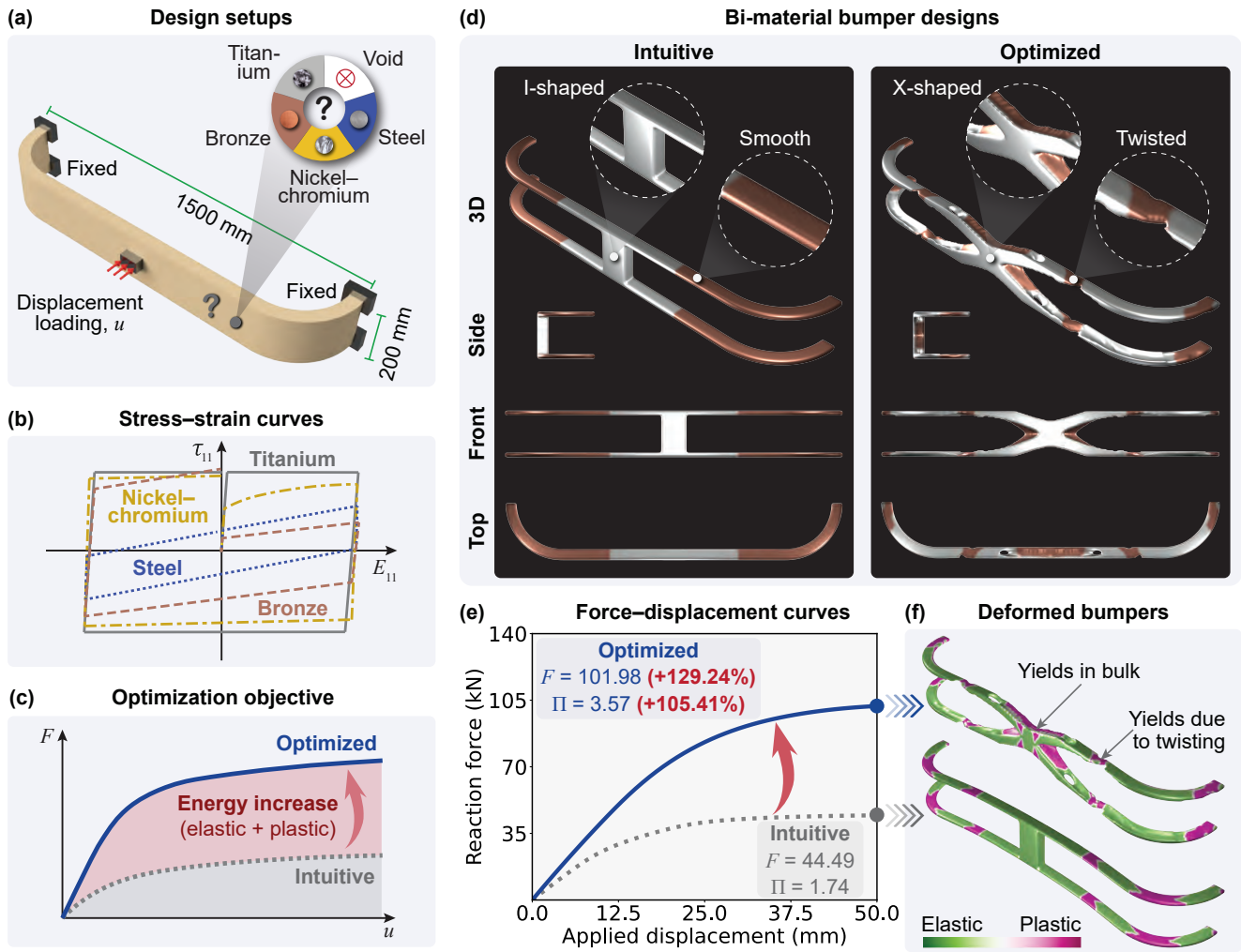


Figure 8: Design and optimization of 3D bumpers. (a) Design setups: the design domain, boundary conditions, and candidate materials (titanium, bronze, nickel-chromium, steel, and void). The variable u is the applied displacement. (b) Uniaxial Kirchhoff stress-Lagrangian strain (τ_{11} - E_{11}) curves of candidate materials. (c) Optimization objective: maximizing the total energy. The variable F is the reaction force. (d) Various views of the intuitive and optimized bi-material bumper designs. (e) Force-displacement (F - u) curves. The force (F) is in kN, and the total energy (Π) is in kN-m. The percentages are the improved values compared to the intuitive design. (f) Elastic/plastic regions in the deformed configuration at the final load step.

structure in the middle, which shortens load paths to enhance structural stiffness. It also exhibits twisted regions that concentrate on plastic deformation. These features enhance both elastic energy absorption and plastic energy dissipation, contributing to the lifted force–displacement ($F-u$) curve in Fig. 9(b) and energy–displacement ($\Pi-u$) curve in Fig. 9(c). Ultimately, the optimized design achieves a 159.72% increase in end force and a 160.49% increase in total energy compared to the intuitive design.

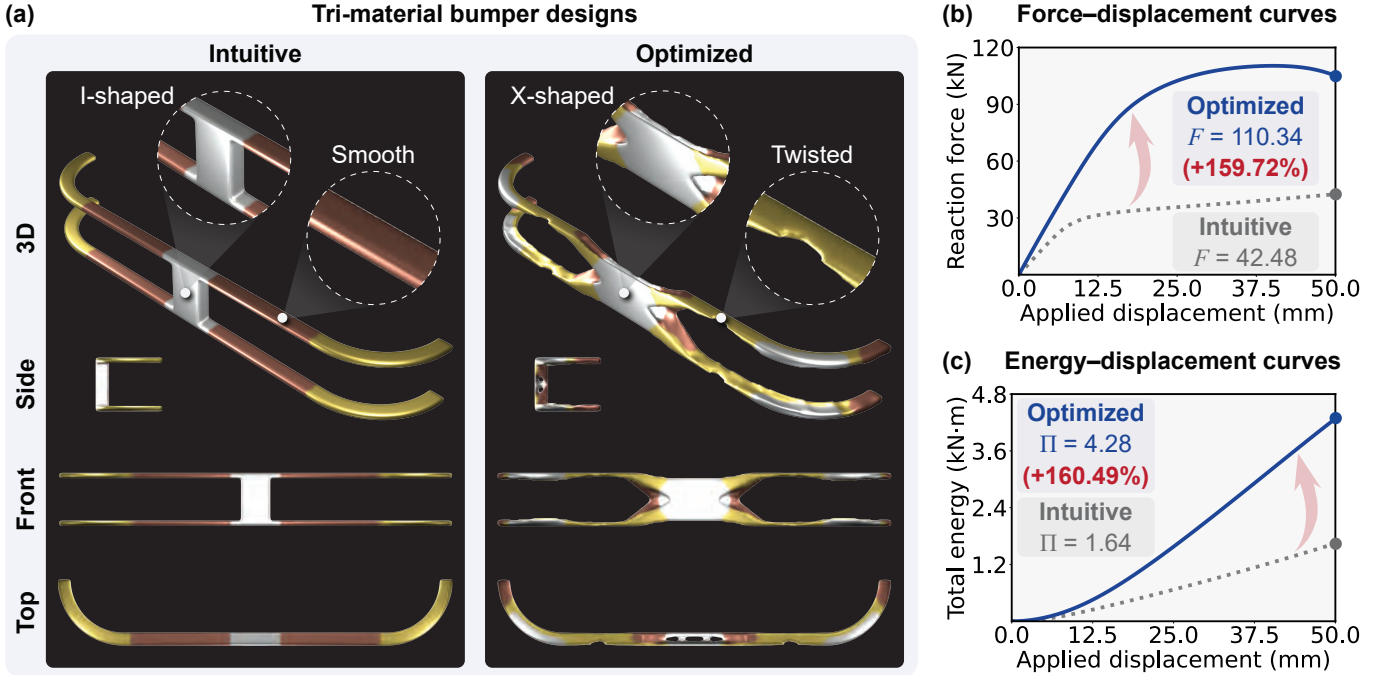


Figure 9: Design and optimization of tri-material bumpers. (a) Various views of the intuitive and optimized designs. (b)–(c) Force–displacement ($F-u$) and energy–displacement ($\Pi-u$) curves, respectively. The force (F) is in kN, and the total energy (Π) is in kN·m. The percentages are the improved values compared to the intuitive design.

We now optimize a four-material bumper by incorporating steel in addition to titanium, bronze, and nickel–chromium. The constraints include the total material volume ($g_{V0} \leq 0$) with an upper bound of $\bar{V} = 0.2$, and individual material volumes ($g_{V1} \leq 0$, $g_{V2} \leq 0$, $g_{V3} \leq 0$, and $g_{V4} \leq 0$) with equal upper bounds of $\bar{V}_1 = \bar{V}_2 = \bar{V}_3 = \bar{V}_4 = 0.05$. The intuitive and optimized designs are shown in Fig. 10(a), which share the same usage for each material. Compared to the intuitive design, the optimized four-material bumper features a bulky structure in the middle, connected to four twisted regions. This highly non-intuitive configuration strategically exploits material properties: bulk steel material yields around the displacement loading area, while bronze yields near the fixed ends (similar to the elastic/plastic distribution shown in Fig. 8(f)), which provide most plastic energy dissipation. Meanwhile, titanium and nickel–chromium primarily deform elastically (except in the twisted regions) due to their higher yield strengths, which mainly contribute to elastic energy absorption. Eventually, as shown in Figs. 10(b) and (c), the end force of the optimized bumper increases by 300.27% compared to the intuitive design, while the total energy improves by 259.31%.

Taking a broader view of the optimized bi-material, tri-material, and four-material bumpers, we draw several observations as follows. First, the proposed topology optimization framework is highly versatile, accommodating a wide range of design problems involving finite strain elastoplasticity, regardless of dimensionality, material hardening types, or the number of candidate materials. Second, as the number of materials increases and the design space expands, it is increasingly difficult to create effective elastoplastic structures based on intuition or experience alone. This is evident from the progressively larger total energy increments achieved by the optimized designs compared to the intuitive ones — 105.41% in the bi-material case, 160.49% in the tri-material case, and 259.31% in the four-material case. In contrast, the proposed topology optimization framework consistently delivers high-performance designs by leveraging

rigorous mechanics-based elastoplastic analysis and gradient-based optimization, effectively navigating the complexities of large design spaces.

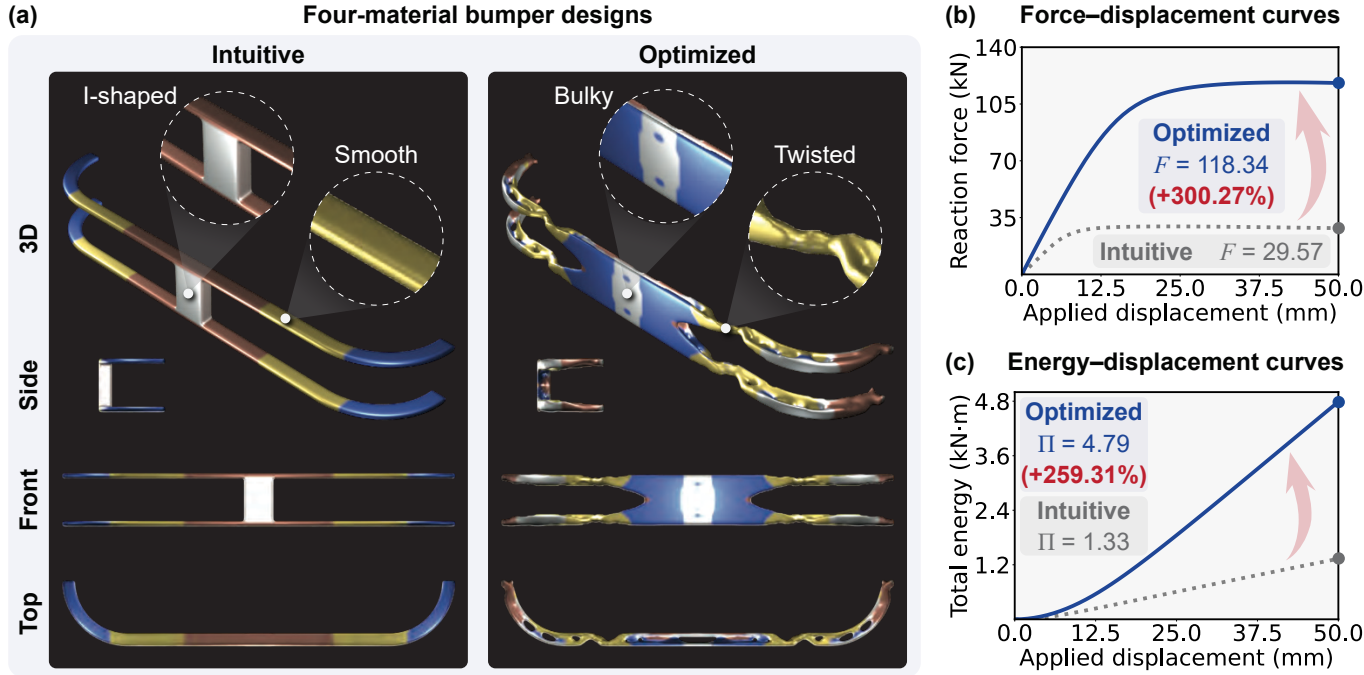


Figure 10: Design and optimization of four-material bumpers. (a) Various views of the intuitive and optimized designs. (b)–(c) Force–displacement (F – u) and energy–displacement (Π – u) curves, respectively. The force (F) is in kN, and the total energy (Π) is in kN·m. The percentages are the improved values compared to the intuitive design.

4.4. Cold working profiled sheets with maximized load-bearing capacity and multiple engineering constraints

In this final example, we highlight the full potential of the proposed framework in optimizing elastoplastic responses involving ultra-large deformations and complex load histories. Furthermore, we demonstrate the versatility and generality of the framework in bridging the gap between mechanical design and practical considerations such as cost, lightweight, and sustainability.

4.4.1. Multi-stage topology optimization of profiled sheets

To illustrate the optimization of large elastoplastic deformations and complex load histories, we design profiled sheets as depicted in Fig. 11. These sheets are manufactured by bending a flat metallic plate at room temperature, a process commonly known as cold working or metal-forming (Gearing et al., 2001; Cvitanic et al., 2008). The resulting corrugated shapes of the profiled sheets provide both mechanical (e.g., increased area moment of inertia and enhanced material strength due to strain hardening) and non-mechanical (e.g., improved rainwater drainage and better architectural aesthetics) advantages. These attributes make profiled sheets widely applicable in various domains (Wright et al., 1987), such as rooftops and walls in structural engineering.

To design such profiled sheets, we begin with a raw flat sheet, as shown in Fig. 11(a). Our goal is to optimally distribute titanium, bronze, nickel–chromium, and steel (material properties are provided in Table 1 and Fig. 8(b)) in the processing (metal-forming) stage while maximizing the end force during the service (load-carrying) stage (Fig. 11(b)).

The processing and service stages of the profiled sheets are detailed in Fig. 11(c). During the processing stage, the flat metallic sheet is bent along the short edge to achieve the desired corrugated profile. In the service stage, the sheet undergoes bending along its long edge under new boundary conditions to simulate practical usage. These stages together form the whole-life analysis of the profiled sheet. Notably, unlike

traditional topology optimization problems where design variables and objectives belong to the same stage, in this case, the design variables (material distribution) are defined in the processing stage, while the design objective (maximizing load-carrying capacity) belongs to the service stage. Additionally, the irreversible nature of elastoplasticity introduces history dependence both within each stage (where only boundary values, $\bar{\mathbf{q}}$, $\bar{\mathbf{t}}$, and $\bar{\mathbf{u}}$, are updated) and across the stages (where Dirichlet and Neumann boundaries, $\partial\Omega_0^D$ and $\partial\Omega_0^N$, respectively, are updated).

To address this complex design problem, we propose a multi-stage topology optimization approach. Within each optimization iteration, boundary conditions are updated to account for different stages of the profiled sheet — process and service stages; or more precisely, raw, cold-worked, undeformed, and deformed stages in Fig. 11(c). Note that the initial state variables (\mathbf{u} , $\bar{\mathbf{b}}^e$, $\bar{\boldsymbol{\beta}}$, and α) of each stage inherit the converged values from the previous stage to capture history dependence. This multi-stage topology optimization approach is naturally accessible through the proposed framework thanks to the comprehensive history-dependent sensitivity analysis in Appendix E. Consequently, no modifications to the framework are required, and we proceed directly to solving the design problem using the following FEA and optimization parameters.

The design domain is discretized using a structured mesh consisting of 28,800 first-order hexahedral elements. The filter radius is set to $R_\zeta = 20$ mm for $\zeta \in \{\rho, \xi_1, \dots, \xi_{N\xi}\}$. The Heaviside sharpness parameter, β_ζ , is initially set to 1 and doubles every 40 optimization iterations starting from iteration 41 until it reaches a maximum value of $\beta_\zeta = 256$. The penalty parameters for the density variable are fixed at $p_\kappa = p_\mu = p_h = p_k = 3$, while the penalty parameter for the material variables, p_ξ , starts at 1 and increases by 0.5 every 60 optimization iterations from iteration 41, up to a maximum of $p_\xi = 4$. The weighting factors in (39) are set as $w_{\text{stiff}} = w_{\text{energy}} = 0$ and $w_{\text{force}} = 1$. The constraints include the individual material volumes ($g_{V1} \leq 0$, $g_{V2} \leq 0$, $g_{V3} \leq 0$, and $g_{V4} \leq 0$) with equal upper bounds $\bar{V}_1 = \bar{V}_2 = \bar{V}_3 = \bar{V}_4 = 0.25$ to account for material availability. The maximum number of optimization iterations is set to 400.

During the topology optimization process, 12 non-uniform load steps are used for the processing stage, 16 uniform load steps for the service stage, and 13 steps for transitioning from the processing to service stages to simulate the removal of support and load blocks and restore the sheet to a stress-free state. Following optimization, refined analyses are conducted with 40 load steps for the processing stage, 61 load steps for the service stage, and 13 load steps for the transition stage.

After multi-stage topology optimization, we present the optimized profiled sheet in Fig. 11(d), alongside an intuitive design with identical material usage for reference. For each design, four snapshots are shown, corresponding to the key stages depicted in Fig. 11(c). Unlike the serial arrangement of the four candidate materials in the intuitive design, the optimized profiled sheet features an intertwined material distribution that leverages the complementary properties of the materials shown in Fig. 8(b). Additionally, both designs exhibit large deformations in two directions, which necessitates the proposed framework to account for finite strain elastoplasticity — an advancement beyond the reach of the infinitesimal strain version in Jia et al. (2025).

The force–displacement (F – u) curves for both processing and service stages are compared in Fig. 11(e). In the processing stage, the force–displacement curves of the two designs are similar; however, in the service stage, the optimized structure exhibits a force–displacement curve that surpasses the intuitive design, achieving a 75.56% increase in the end force. This performance improvement remarks the effectiveness of the proposed framework in tackling optimization challenges involving large elastoplastic deformations and multiple stages of loading.

4.4.2. Optimized profiled sheets with practical constraints

Despite the superior mechanical performance of the optimized profiled sheet endowed by the proposed framework, practical constraints — such as cost, lightweight, and sustainability — typically need to be integrated to create a useful mechanical product (Kundu and Zhang, 2025). In this case study, we incorporate these practical constraints into the framework, thereby bridging the gap between elastoplastic design optimization and broader real-world considerations.

To achieve this goal, we replace the individual material volume constraints ($g_{V1} \leq 0$, $g_{V2} \leq 0$, $g_{V3} \leq 0$,

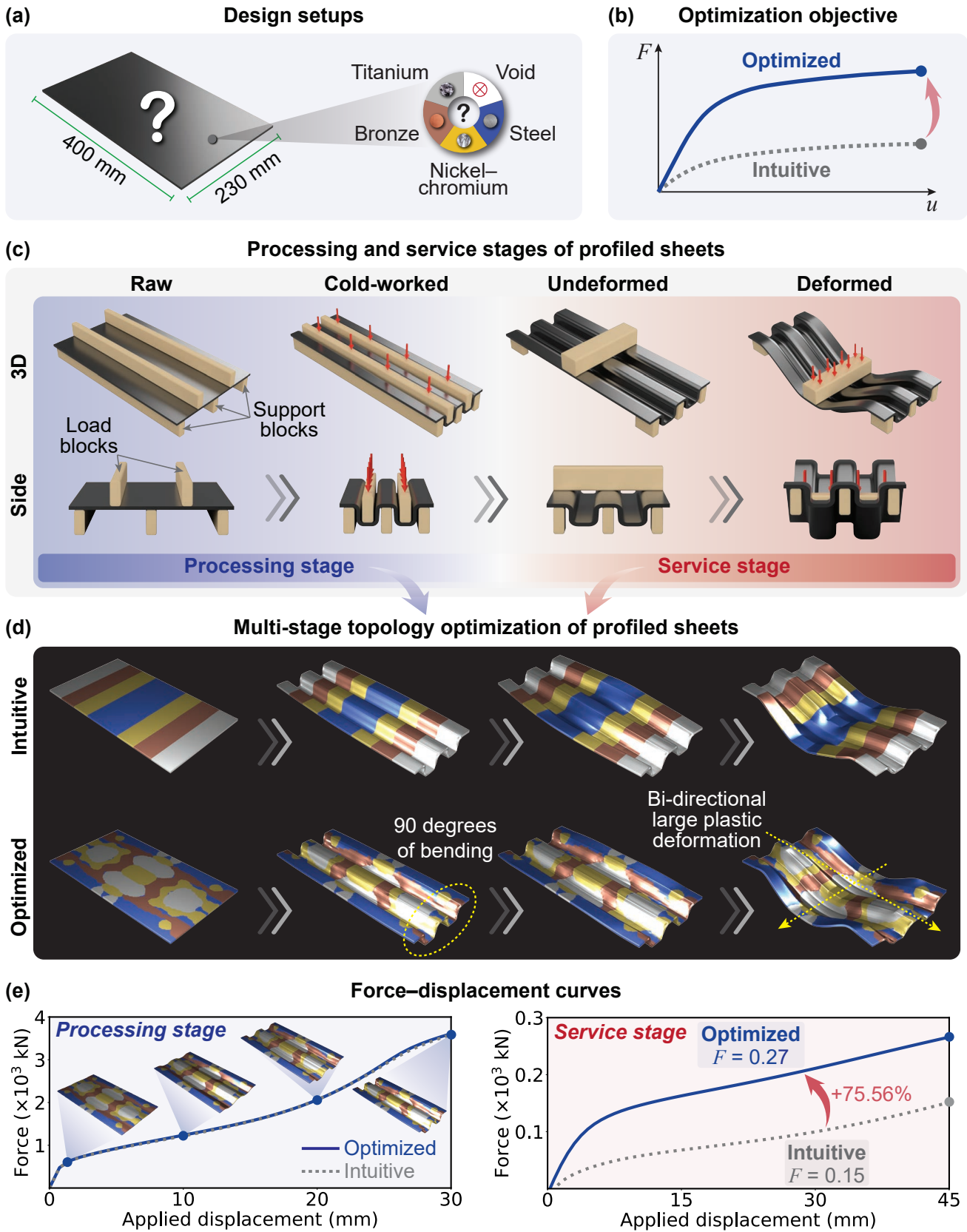


Figure 11: Design and optimization of profiled sheets. (a) Design setups: the design domain and candidate materials (titanium, bronze, nickel–chromium, steel, and void). (b) Optimization objective: maximizing the end force. The variables F and u are the reaction force and applied displacement, respectively. (c) Processing and service stages of profiled sheets. (d) Multi-stage topology optimization of profiled sheets. (e) Force–displacement (F – u) curves of the two stages.

and $g_{V_4} \leq 0$) imposed on the optimized design in Fig. 12(d) with practical constraints on price ($g_P \leq 0$), mass density ($g_M \leq 0$), and CO₂ footprint ($g_C \leq 0$). These constraints are defined with upper bounds set as the averages of the corresponding properties of the four candidate materials listed in Table 1: $\bar{P} = 17.31$ USD/kg, $\bar{M} = 7,340$ kg/m³, and $\bar{C} = 17.64$ kg/kg.

Under these updated constraints, we present the optimized profiled sheets in Fig. 12(a). Among the four optimized designs, Dsgs. 1–3 are constrained individually by price, mass density, and CO₂ footprint, respectively, while Dsg. 4 considers all three constraints simultaneously. These designs feature distinct material distributions (Fig. 12(a)) and usage patterns (Fig. 12(b)) as follows.

- The price-constrained design (Dsg. 1) primarily incorporates titanium and steel due to their superior initial-strength-to-price ratios of 34.96 and 34.24 MPa·kg/USD, respectively, compared to bronze (10.90 MPa·kg/USD) and nickel–chromium (17.86 MPa·kg/USD). A small amount of bronze appears sparingly, likely due to the strength enhancement achieved through linear isotropic hardening. On the other hand, nickel–chromium usage is minimized due to its highest absolute price.
- The weight-constrained design (Dsg. 2) is overwhelmingly dominated by titanium, a result of its optimal combination of the highest initial yield strength and the lowest mass density among the four materials.
- In contrast, the CO₂-constrained design (Dsg. 3) is largely composed of nickel–chromium. This material is favored because of its medium initial-strength-to-CO₂ ratio of 27.11 MPa·kg/kg, which lies between the ratios of titanium (21.11 MPa·kg/kg), bronze (24.17 MPa·kg/kg), and steel (30.54 MPa·kg/kg). Furthermore, with nonlinear isotropic hardening, the strength-to-CO₂ ratio of nickel–chromium improves to 43.07 MPa·kg/kg, making it a suitable option.
- Finally, the balanced design (Dsg. 4) leverages similar amounts of all four candidate materials. This distribution reflects the fact that the upper bounds for the price, mass density, and CO₂ footprint constraints are averages of the properties of all four materials. As a result, the design naturally balances the contributions of titanium, bronze, nickel–chromium, and steel.

Remark 6. In addition to the mechanical performance improvements demonstrated in Fig. 4, the incorporation of practical constraints also leads to the automatic inclusion of multiple materials in the optimized designs. This outcome further shows the necessity of a multimaterial topology optimization framework.

We assess the performance of these optimized designs in Fig. 12(c) and evaluate their performance metrics in Fig. 12(d). The load-carrying capacity is measured by the end force of the structures, while economic consideration, lightweight, and sustainability are quantified as the reciprocals of the price, mass density, and CO₂ footprint, respectively. All metrics are normalized on a 0–1 scale for comparative purposes.

Interestingly, all four designs achieve similar load-carrying capacities (Fig. 12(c)). This result highlights the non-convex nature of the design problem, where multiple local minima exist. Therefore, practical constraints can be incorporated to tailor the non-mechanical performance of designs without compromising mechanical performance, as illustrated in Fig. 12(d). With this final generalization of the proposed framework to practical constraints, we conclude all example demonstrations.

5. Conclusions

In this study, we introduced the theory, method, and application of a multimaterial topology optimization approach for programming elastoplastic responses of structures under large deformations. The framework simultaneously determines the optimal structural geometries and material phases, leveraging a mechanics-based finite strain elastoplasticity theory that rigorously ensures isochoric plastic flow. Furthermore, the framework integrates a comprehensive path-dependent sensitivity analysis using the reversed adjoint method and automatic differentiation, enabling gradient-based optimization of design variables.

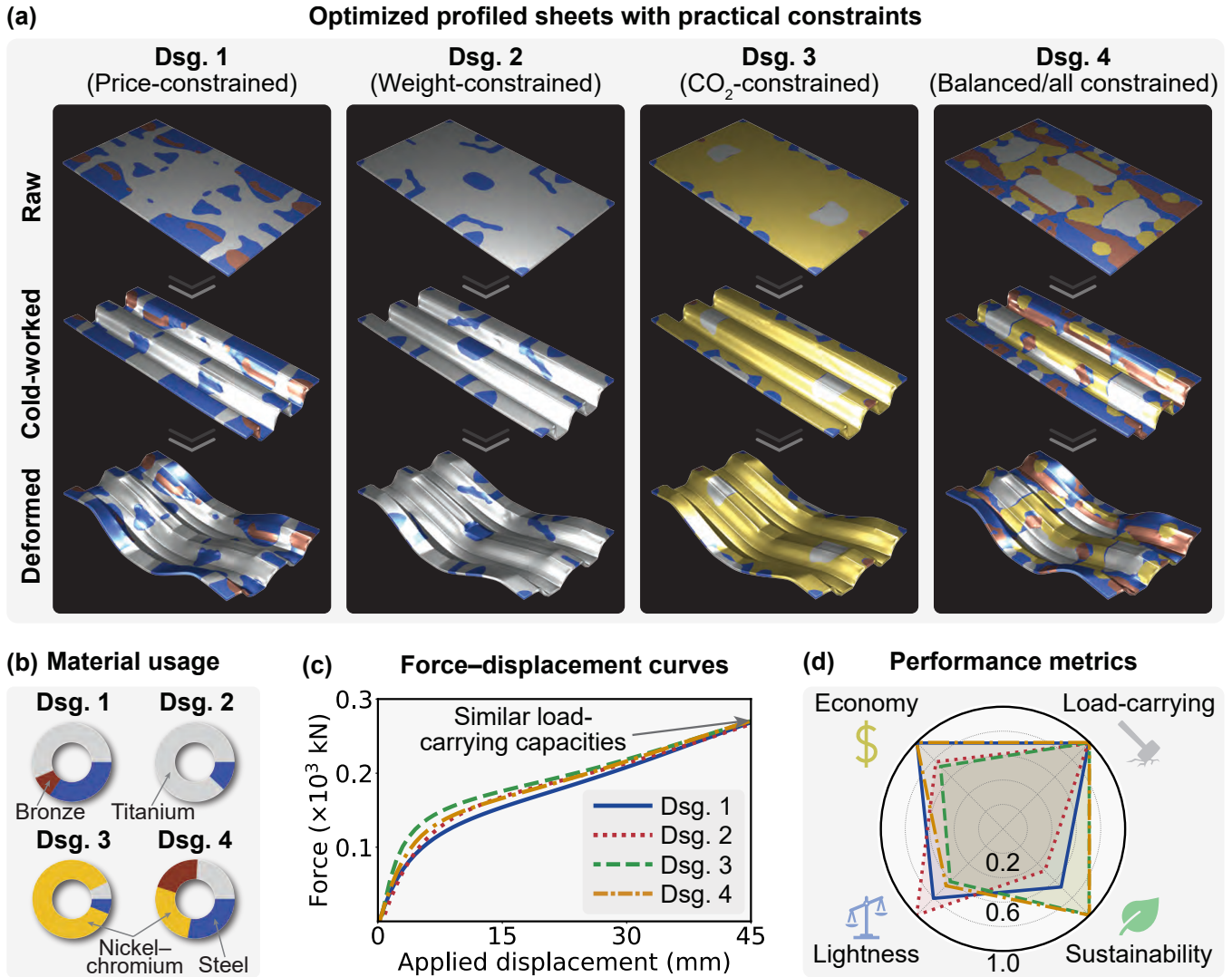


Figure 12: Multi-stage topology optimization of profiled sheets with practical constraints. (a) Optimized profiled sheets with various practical constraints. (b) Material usage of the four optimized profiled sheets. (c) Force-displacement ($F-u$) curves of the service stage. (d) Performance metrics of the optimized profiled sheets.

To demonstrate the effectiveness of the proposed framework, we presented four real-world application examples and uncovered the mechanisms to achieve target behaviors. First, we optimized energy-dissipating dampers, demonstrating the superior energy dissipation performance of the optimized designs compared to intuitive configurations under various loading conditions, including half-cycle, full-cycle, and multiple-cycle scenarios. This example also highlighted the transition from kinematic to isotropic hardening with increasing displacement amplitudes to maximize energy dissipation. Next, we explored the synergistic use of hyperelastic and elastoplastic materials for achieving diverse stiffness–strength interplays of double-clamped beams, showcasing the framework’s versatility in handling different material types — purely hyperelastic, purely elastoplastic, or mixed. In a further example, we extended the optimization to 3D by designing impact-resistant bumpers, while illustrating the capability to handle more than two candidate materials. Finally, we demonstrated multi-stage topology optimization for profiled sheets, focusing on maximizing load-carrying capacity under ultra-large deformations. This example also incorporated practical constraints, including cost, lightweight, and sustainability, bridging the gap between elastoplastic design and real-world considerations.

Across these examples, the proposed framework demonstrated its ability to optimize stiffness, strength, and effective structural toughness for elastoplastic structures in 2D and 3D across various spatial geometries, material types, hardening behaviors, and candidate material combinations. By fully exploiting the potential of elastoplasticity, this framework represents a step forward in designing the next generation of engineering structures. Looking ahead, we aspire to further generalize this framework to account for rate dependence and pressure dependence, which remain an ongoing focus of our research.

CRedit authorship contribution statement

Yingqi Jia: Conceptualization, Methodology, Software, Validation, Formal analysis, Investigation, Data curation, Writing–original draft, Writing–review & editing, Visualization. **Xiaojia Shelly Zhang:** Conceptualization, Methodology, Investigation, Resources, Writing–original draft, Writing–review & editing, Supervision, Project administration, Funding acquisition.

Declaration of competing interest

The authors declare that they have no known competing financial interests or personal relationships that could have appeared to influence the work reported in this paper.

Acknowledgments

Authors X.S.Z. and Y.J. are grateful for the support from the U.S. Defense Advanced Research Projects Agency (DARPA) Award HR0011-24-2-0333. The information provided in this paper is the sole opinion of the authors and does not necessarily reflect the view of the sponsoring agencies.

Distribution statement

Approved for public release; distribution is unlimited.

Data availability

Data will be made available on request.

Appendix A. Updating formulae of $\bar{\mathbf{b}}_{n+1}^e$ that enforce the isochoric plastic flow

In this section, we introduce the updating formulae of \mathbf{b}_{n+1}^e in (17) that enforce the isochoric plastic flow ($J_{n+1}^p = 1$). We recall the definitions of \mathbf{b}_{n+1}^e in (2) and \mathbf{C}_{n+1}^p in (3) and derive

$$\mathbf{b}_{n+1}^e = \mathbf{F}_{n+1}(\mathbf{C}_{n+1}^p)^{-1}\mathbf{F}_{n+1}^\top.$$

The isochoric plastic flow then requires

$$J_{n+1}^p = 1 \iff \det(\mathbf{b}_{n+1}^e) = J_{n+1}^2 \iff \det\left(J_{n+1}^{-2/3}\mathbf{b}_{n+1}^e\right) = 1 \iff \det\left(\bar{\mathbf{b}}_{n+1}^e\right) = 1. \quad (\text{A.1})$$

Additionally, we rewrite (14)₁ as

$$\bar{\mathbf{b}}_{n+1}^e = \bar{\mathbf{b}}_{n+1}^{e, \text{tr}} - \frac{2\bar{\mu}_{n+1}^{\text{tr}}}{\mu}\hat{\gamma}_{n+1}\mathbf{n}_{n+1}$$

based on Proposition 1. This relationship determines the deviatoric part of $\bar{\mathbf{b}}_{n+1}^e$ as

$$\text{dev}\left(\bar{\mathbf{b}}_{n+1}^e\right) = \text{dev}\left(\bar{\mathbf{b}}_{n+1}^{e, \text{tr}}\right) - \frac{2\bar{\mu}_{n+1}^{\text{tr}}}{\mu}\hat{\gamma}_{n+1}\mathbf{n}_{n+1} \quad (\text{A.2})$$

where we remark \mathbf{n}_{n+1} is deviatoric based on its definition in (14)₆. Based on (A.1) and (A.2), the enforcement of the isochoric plastic flow amounts to identifying the volumetric part of $\bar{\mathbf{b}}_{n+1}^e$ — or more specifically, its first invariant, $\mathcal{I}_1 = \text{tr}(\bar{\mathbf{b}}_{n+1}^e)$ — such that $\mathcal{I}_3 = \det(\bar{\mathbf{b}}_{n+1}^e) = 1$ for given $\text{dev}(\bar{\mathbf{b}}_{n+1}^e)$. We now determine \mathcal{I}_1 by extending the analysis in Simo and Miehe (1992).

Note that the invariants \mathcal{I}_1 , \mathcal{I}_3 , \mathcal{J}_2 , and \mathcal{J}_3 of a symmetric second-order tensor satisfy

$$\frac{\mathcal{I}_1^3}{27} - \frac{\mathcal{I}_1\mathcal{J}_2}{3} + \mathcal{J}_3 - \mathcal{I}_3 = 0$$

where \mathcal{J}_2 and \mathcal{J}_3 are defined as

$$\mathcal{J}_2 = \frac{1}{2}\left\|\text{dev}\left(\bar{\mathbf{b}}_{n+1}^e\right)\right\|^2 \quad \text{and} \quad \mathcal{J}_3 = \det\left[\text{dev}\left(\bar{\mathbf{b}}_{n+1}^e\right)\right].$$

Consequently, a necessary condition of $\mathcal{I}_3 = \det(\bar{\mathbf{b}}_{n+1}^e) = 1$ reads as

$$t^3 + \mathcal{P}t + \mathcal{Q} = 0 \quad (\text{A.3})$$

where

$$t = \frac{\mathcal{I}_1}{3} > 0, \quad \mathcal{P} = -\mathcal{J}_2 \leq 0, \quad \text{and} \quad \mathcal{Q} = \mathcal{J}_3 - 1.$$

Our objective then boils down to compute the positive real root from the depressed cubic equation in (A.3).

Following a standard procedure, we compute the discriminant of (A.3) as

$$\Delta = -\left(\frac{\mathcal{P}^3}{27} + \frac{\mathcal{Q}^2}{4}\right)$$

and discuss the solutions of (A.3) based on the sign of Δ as follows.

- The case of $\Delta < 0$. The equation in (A.3) has one positive real root and two non-real complex conjugate roots. We should take the real root as

$$t_1 = \left(-\frac{\mathcal{Q}}{2} + \sqrt{-\Delta}\right)^{1/3} + \left(-\frac{\mathcal{Q}}{2} - \sqrt{-\Delta}\right)^{1/3}.$$

- The case of $\Delta = 0$. The equation in (A.3) has a triple root of zero (when $\mathcal{P} = 0$) or the combination of a simple root of $3\mathcal{Q}/\mathcal{P}$ and a double root of $-3\mathcal{Q}/2\mathcal{P}$ (when $\mathcal{P} < 0$). We should take the only positive real root as

$$t_2 = \max \left\{ \frac{3\mathcal{Q}}{\mathcal{P}}, -\frac{3\mathcal{Q}}{2\mathcal{P}} \right\}.$$

- The case of $\Delta > 0$. The equation in (A.3) has three distinct real roots expressed in trigonometric forms as shown in (18). Based on Descartes' rule of signs, only one solution among r_1 , r_2 , and r_3 is positive when $\mathcal{Q} \leq 0$, and we should set the solution to (A.3) as

$$t_3 = \max\{r_1, r_2, r_3\}.$$

Otherwise ($\mathcal{Q} > 0$), two solutions among r_1 , r_2 , and r_3 are positive, and we should select the solution such that $\bar{\mathbf{b}}_{n+1}^e$ is positive definite by ensuring

$$\left(\bar{\mathbf{b}}_{n+1}^e \right)_{11} > 0 \quad \text{and} \quad \left(\bar{\mathbf{b}}_{n+1}^e \right)_{11} \left(\bar{\mathbf{b}}_{n+1}^e \right)_{22} - \left(\bar{\mathbf{b}}_{n+1}^e \right)_{12} \left(\bar{\mathbf{b}}_{n+1}^e \right)_{21} > 0$$

based on the Sylvester's criterion.

Finally, combining the solutions from all scenarios ($\Delta < 0$, $\Delta = 0$, and $\Delta > 0$), we derive the updating formulae of $\bar{\mathbf{b}}_{n+1}^e$ in (17). We remark that [Simo and Miehe \(1992\)](#) only consider the scenario of $\Delta < 0$ by assuming $\mathcal{J}_2 \ll |1 - \mathcal{J}_3|$. Here we remove this assumption and incorporate the scenarios of $\Delta = 0$ and $\Delta > 0$ to account for a broader type of material responses.

Appendix B. Derivation of the second elastoplastic moduli

This section derives the second elastoplastic moduli in (28). Taking the derivative of the second Piola–Kirchhoff stress (\mathbf{S}_{n+1}) in (25) with respect to the Lagrangian strain tensor (\mathbf{E}_{n+1}) in (1) yields

$$\begin{aligned} \mathbb{C}_{n+1}^{\text{ep}} = \frac{\partial \mathbf{S}_{n+1}}{\partial \mathbf{E}_{n+1}} = 2 \frac{\partial \mathbf{S}_{n+1}}{\partial \mathbf{C}_{n+1}} = & 2 \frac{\partial \varphi^*(\boldsymbol{\tau}_{n+1}^{\text{vol}})}{\partial \mathbf{C}_{n+1}} + 2 \frac{\partial \varphi^*(\mathbf{s}_{n+1}^{\text{tr}})}{\partial \mathbf{C}_{n+1}} - 4 \hat{\gamma}_{n+1} \varphi^*(\mathbf{n}_{n+1}) \otimes \frac{\overline{\partial \mu}_{n+1}^{\text{tr}}}{\partial \mathbf{C}_{n+1}} \\ & - 4 \overline{\mu}_{n+1}^{\text{tr}} \varphi^*(\mathbf{n}_{n+1}) \otimes \frac{\partial \hat{\gamma}_{n+1}}{\partial \mathbf{C}_{n+1}} - 4 \overline{\mu}_{n+1}^{\text{tr}} \hat{\gamma}_{n+1} \frac{\partial \varphi^*(\mathbf{n}_{n+1})}{\partial \mathbf{C}_{n+1}}. \end{aligned} \quad (\text{B.1})$$

One immediate next step is to compute the partial derivatives involved in $\mathbb{C}_{n+1}^{\text{ep}}$, which are laid out below.

Appendix B.1. The computation of $\partial \varphi^*(\boldsymbol{\tau}_{n+1}^{\text{vol}})/\partial \mathbf{C}_{n+1}$

Note that

$$\frac{\partial \varphi^*(\boldsymbol{\tau}_{n+1}^{\text{vol}})}{\partial \mathbf{C}_{n+1}} = \frac{\partial (J_{n+1} U'_{n+1} \mathbf{C}_{n+1}^{-1})}{\partial \mathbf{C}_{n+1}} = \mathbf{C}_{n+1}^{-1} \otimes \frac{\partial (J_{n+1} U'_{n+1})}{\partial \mathbf{C}_{n+1}} + (J_{n+1} U'_{n+1}) \frac{\partial \mathbf{C}_{n+1}^{-1}}{\partial \mathbf{C}_{n+1}}. \quad (\text{B.2})$$

Substituting

$$\frac{\partial (J_{n+1} U'_{n+1})}{\partial \mathbf{C}_{n+1}} = \frac{\partial (J_{n+1} U'_{n+1})}{\partial J_{n+1}} \frac{\partial J_{n+1}}{\partial \mathbf{C}_{n+1}} = (J_{n+1} U'_{n+1})' \left(\frac{1}{2} J_{n+1} \mathbf{C}_{n+1}^{-1} \right)$$

and

$$\frac{\partial \mathbf{C}_{n+1}^{-1}}{\partial \mathbf{C}_{n+1}} = -\mathbb{I}_{\mathbf{C}_{n+1}^{-1}} \quad \text{with} \quad \left(\mathbb{I}_{\mathbf{C}_{n+1}^{-1}} \right)_{ijkl} = \frac{1}{2} \left[(C_{n+1}^{-1})_{ik} (C_{n+1}^{-1})_{jl} + (C_{n+1}^{-1})_{il} (C_{n+1}^{-1})_{jk} \right]$$

into (B.2) renders

$$\frac{\partial \varphi^*(\boldsymbol{\tau}_{n+1}^{\text{vol}})}{\partial \mathbf{C}_{n+1}} = \frac{1}{2} J_{n+1} (J_{n+1} U'_{n+1})' \mathbf{C}_{n+1}^{-1} \otimes \mathbf{C}_{n+1}^{-1} - J_{n+1} U'_{n+1} \mathbb{I}_{\mathbf{C}_{n+1}^{-1}}. \quad (\text{B.3})$$

Appendix B.2. The computation of $\partial\varphi^*(\mathbf{s}_{n+1}^{\text{tr}})/\partial\mathbf{C}_{n+1}$

Note that

$$\begin{aligned}\bar{\mathbf{b}}_{n+1}^{\text{e, tr}} &= \bar{\mathbf{f}}_{n+1} \bar{\mathbf{b}}_n^{\text{e}} \bar{\mathbf{f}}_{n+1}^\top = \left[\left(J_{n+1}^f \right)^{-1/3} \mathbf{f}_{n+1} \right] \left[\left(J_n^{\text{e}} \right)^{-2/3} \mathbf{b}_n^{\text{e}} \right] \left[\left(J_{n+1}^f \right)^{-1/3} \mathbf{f}_{n+1}^\top \right] \\ &= \left(\frac{J_{n+1} J_n^{\text{e}}}{J_n} \right)^{-2/3} (\mathbf{F}_{n+1} \mathbf{F}_n^{-1}) (\mathbf{F}_n^{\text{e}} (\mathbf{F}_n^{\text{e}})^\top) (\mathbf{F}_n^{-\top} \mathbf{F}_{n+1}^\top) \\ &= J_{n+1}^{-2/3} \mathbf{F}_{n+1} (\mathbf{F}_n^{\text{p}})^{-1} (\mathbf{F}_n^{\text{p}})^{-\top} \mathbf{F}_{n+1}^\top = J_{n+1}^{-2/3} \mathbf{F}_{n+1} (\mathbf{C}_n^{\text{p}})^{-1} \mathbf{F}_{n+1}^\top\end{aligned}\tag{B.4}$$

due to $J_n = J_n^{\text{e}}$ (assuming isochoric plastic flow) and $J_{n+1} = J_{n+1}^f J_n$. We recall

$$\begin{aligned}\mathbf{s}_{n+1}^{\text{tr}} &= \mu \operatorname{dev} \left(\bar{\mathbf{b}}_{n+1}^{\text{e, tr}} \right) = \mu J_{n+1}^{-2/3} \operatorname{dev} \left[\mathbf{F}_{n+1} (\mathbf{C}_n^{\text{p}})^{-1} \mathbf{F}_{n+1}^\top \right] \\ &= \mu J_{n+1}^{-2/3} \left\{ \mathbf{F}_{n+1} (\mathbf{C}_n^{\text{p}})^{-1} \mathbf{F}_{n+1}^\top - \frac{1}{3} \operatorname{tr} \left[\mathbf{F}_{n+1} (\mathbf{C}_n^{\text{p}})^{-1} \mathbf{F}_{n+1}^\top \right] \mathbf{I} \right\} \\ &= \mu J_{n+1}^{-2/3} \left\{ \mathbf{F}_{n+1} (\mathbf{C}_n^{\text{p}})^{-1} \mathbf{F}_{n+1}^\top - \frac{1}{3} \left[(\mathbf{C}_n^{\text{p}})^{-1} : \mathbf{C}_{n+1} \right] \mathbf{I} \right\}\end{aligned}$$

and derive

$$\varphi^*(\mathbf{s}_{n+1}^{\text{tr}}) = \mathbf{F}_{n+1}^{-1} \mathbf{s}_{n+1}^{\text{tr}} \mathbf{F}_{n+1}^{-\top} = \mu J_{n+1}^{-2/3} \left\{ (\mathbf{C}_n^{\text{p}})^{-1} - \frac{1}{3} \left[(\mathbf{C}_n^{\text{p}})^{-1} : \mathbf{C}_{n+1} \right] \mathbf{C}_{n+1}^{-1} \right\}.$$

Next, we compute

$$\frac{\partial\varphi^*(\mathbf{s}_{n+1}^{\text{tr}})}{\partial\mathbf{C}_{n+1}} = \mu \left\{ (\mathbf{C}_n^{\text{p}})^{-1} - \frac{1}{3} \left[(\mathbf{C}_n^{\text{p}})^{-1} : \mathbf{C}_{n+1} \right] \mathbf{C}_{n+1}^{-1} \right\} \frac{\partial J_{n+1}^{-2/3}}{\partial\mathbf{C}_{n+1}} - \frac{\mu}{3} J_{n+1}^{-2/3} \frac{\partial}{\partial\mathbf{C}_{n+1}} \left\{ \left[(\mathbf{C}_n^{\text{p}})^{-1} : \mathbf{C}_{n+1} \right] \mathbf{C}_{n+1}^{-1} \right\}.\tag{B.5}$$

Substituting

$$\frac{\partial J_{n+1}^{-2/3}}{\partial\mathbf{C}_{n+1}} = -\frac{2}{3} J_{n+1}^{-5/3} \frac{\partial J_{n+1}}{\partial\mathbf{C}_{n+1}} = -\frac{2}{3} J_{n+1}^{-5/3} \left(\frac{1}{2} J_{n+1} \mathbf{C}_{n+1}^{-1} \right) = -\frac{1}{3} J_{n+1}^{-2/3} \mathbf{C}_{n+1}^{-1}\tag{B.6}$$

and

$$\begin{aligned}\frac{\partial}{\partial\mathbf{C}_{n+1}} \left\{ \left[(\mathbf{C}_n^{\text{p}})^{-1} : \mathbf{C}_{n+1} \right] \mathbf{C}_{n+1}^{-1} \right\} &= \mathbf{C}_{n+1}^{-1} \otimes \frac{\partial \left[(\mathbf{C}_n^{\text{p}})^{-1} : \mathbf{C}_{n+1} \right]}{\partial\mathbf{C}_{n+1}} + \left[(\mathbf{C}_n^{\text{p}})^{-1} : \mathbf{C}_{n+1} \right] \frac{\partial\mathbf{C}_{n+1}^{-1}}{\partial\mathbf{C}_{n+1}} \\ &= \mathbf{C}_{n+1}^{-1} \otimes (\mathbf{C}_n^{\text{p}})^{-1} - \left[(\mathbf{C}_n^{\text{p}})^{-1} : \mathbf{C}_{n+1} \right] \mathbb{I}_{\mathbf{C}_{n+1}^{-1}}\end{aligned}$$

into (B.5) renders

$$\begin{aligned}\frac{\partial\varphi^*(\mathbf{s}_{n+1}^{\text{tr}})}{\partial\mathbf{C}_{n+1}} &= -\frac{\mu}{3} J_{n+1}^{-2/3} \left\{ (\mathbf{C}_n^{\text{p}})^{-1} - \frac{1}{3} \left[(\mathbf{C}_n^{\text{p}})^{-1} : \mathbf{C}_{n+1} \right] \mathbf{C}_{n+1}^{-1} \right\} \otimes \mathbf{C}_{n+1}^{-1} \\ &\quad - \frac{\mu}{3} J_{n+1}^{-2/3} \left\{ \mathbf{C}_{n+1}^{-1} \otimes (\mathbf{C}_n^{\text{p}})^{-1} - \left[(\mathbf{C}_n^{\text{p}})^{-1} : \mathbf{C}_{n+1} \right] \mathbb{I}_{\mathbf{C}_{n+1}^{-1}} \right\}.\end{aligned}$$

Regrouping terms yields

$$\frac{\partial\varphi^*(\mathbf{s}_{n+1}^{\text{tr}})}{\partial\mathbf{C}_{n+1}} = -\frac{\mu}{3} J_{n+1}^{-2/3} \left\{ (\mathbf{C}_n^{\text{p}})^{-1} \otimes \mathbf{C}_{n+1}^{-1} + \mathbf{C}_{n+1}^{-1} \otimes (\mathbf{C}_n^{\text{p}})^{-1} - \left[(\mathbf{C}_n^{\text{p}})^{-1} : \mathbf{C}_{n+1} \right] \left(\mathbb{I}_{\mathbf{C}_{n+1}^{-1}} + \frac{1}{3} \mathbf{C}_{n+1}^{-1} \otimes \mathbf{C}_{n+1}^{-1} \right) \right\}.\tag{B.7}$$

Based on (B.4), we derive $J_{n+1}^{-2/3} (\mathbf{C}_n^{\text{p}})^{-1} = \varphi^*(\bar{\mathbf{b}}_{n+1}^{\text{tr}})$ and further compute

$$\begin{cases} \mu\varphi^*(\bar{\mathbf{b}}_{n+1}^{\text{tr}}) \otimes \mathbf{C}_{n+1}^{-1} = \varphi^*(\mathbf{s}_{n+1}^{\text{tr}}) \otimes \mathbf{C}_{n+1}^{-1} + \bar{\mu}_{n+1}^{\text{tr}} \mathbf{C}_{n+1}^{-1} \otimes \mathbf{C}_{n+1}^{-1}, \\ \mu\mathbf{C}_{n+1}^{-1} \otimes \varphi^*(\bar{\mathbf{b}}_{n+1}^{\text{tr}}) = \mathbf{C}_{n+1}^{-1} \otimes \varphi^*(\mathbf{s}_{n+1}^{\text{tr}}) + \bar{\mu}_{n+1}^{\text{tr}} \mathbf{C}_{n+1}^{-1} \otimes \mathbf{C}_{n+1}^{-1}, \\ \frac{\mu}{3}\varphi^*(\bar{\mathbf{b}}_{n+1}^{\text{tr}}) : \mathbf{C}_{n+1} = \frac{\mu}{3} \operatorname{tr}(\bar{\mathbf{b}}_{n+1}^{\text{tr}}) = \bar{\mu}_{n+1}^{\text{tr}}. \end{cases}$$

We then reduce (B.7) to

$$\frac{\partial \varphi^*(\mathbf{s}_{n+1}^{\text{tr}})}{\partial \mathbf{C}_{n+1}} = \bar{\mu}_{n+1}^{\text{tr}} \left(\mathbb{I}_{\mathbf{C}_{n+1}^{-1}} - \frac{1}{3} \mathbf{C}_{n+1}^{-1} \otimes \mathbf{C}_{n+1}^{-1} \right) - \frac{1}{3} \left[\varphi^*(\mathbf{s}_{n+1}^{\text{tr}}) \otimes \mathbf{C}_{n+1}^{-1} + \mathbf{C}_{n+1}^{-1} \otimes \varphi^*(\mathbf{s}_{n+1}^{\text{tr}}) \right]. \quad (\text{B.8})$$

Appendix B.3. The computation of $\partial \bar{\mu}_{n+1}^{\text{tr}} / \partial \mathbf{C}_{n+1}$

Note that

$$\frac{\partial \bar{\mu}_{n+1}^{\text{tr}}}{\partial \mathbf{C}_{n+1}} = \frac{\partial \bar{\mu}_{n+1}^{\text{tr}}}{\partial \mathbf{C}_{n+1}} - \frac{1}{3} \frac{\partial}{\partial \mathbf{C}_{n+1}} \text{tr} \left(\bar{\mathbf{f}}_{n+1} \bar{\boldsymbol{\beta}}_n \bar{\mathbf{f}}_{n+1}^\top \right). \quad (\text{B.9})$$

According to (B.4), we derive

$$\bar{\mu}_{n+1}^{\text{tr}} = \frac{\mu}{3} \text{tr} \left(\bar{\mathbf{b}}_{n+1}^{\text{e, tr}} \right) = \frac{\mu}{3} J_{n+1}^{-2/3} \text{tr} \left(\mathbf{F}_{n+1} (\mathbf{C}_n^{\text{p}})^{-1} \mathbf{F}_{n+1}^\top \right) = \frac{\mu}{3} J_{n+1}^{-2/3} (\mathbf{C}_n^{\text{p}})^{-1} : \mathbf{C}_{n+1}.$$

Taking the derivative of $\bar{\mu}_{n+1}^{\text{tr}}$ yields

$$\begin{aligned} \frac{\partial \bar{\mu}_{n+1}^{\text{tr}}}{\partial \mathbf{C}_{n+1}} &= \frac{\mu}{3} \left[(\mathbf{C}_n^{\text{p}})^{-1} : \mathbf{C}_{n+1} \right] \frac{\partial J_{n+1}^{-2/3}}{\partial \mathbf{C}_{n+1}} + \frac{\mu}{3} J_{n+1}^{-2/3} \frac{\partial}{\partial \mathbf{C}_{n+1}} \left[(\mathbf{C}_n^{\text{p}})^{-1} : \mathbf{C}_{n+1} \right] \\ &= \frac{\mu}{3} \left[(\mathbf{C}_n^{\text{p}})^{-1} : \mathbf{C}_{n+1} \right] \left(-\frac{1}{3} J_{n+1}^{-2/3} \mathbf{C}_{n+1}^{-1} \right) + \frac{\mu}{3} J_{n+1}^{-2/3} (\mathbf{C}_n^{\text{p}})^{-1} \\ &= \frac{\mu}{3} J_{n+1}^{-2/3} \left\{ (\mathbf{C}_n^{\text{p}})^{-1} - \frac{1}{3} \left[(\mathbf{C}_n^{\text{p}})^{-1} : \mathbf{C}_{n+1} \right] \mathbf{C}_{n+1}^{-1} \right\} \end{aligned} \quad (\text{B.10})$$

based on (B.6).

Additionally, we rewrite

$$\begin{aligned} \bar{\mathbf{f}}_{n+1} \bar{\boldsymbol{\beta}}_n \bar{\mathbf{f}}_{n+1}^\top &= \left[(J_{n+1}^f)^{-1/3} \mathbf{f}_{n+1} \right] (J_n^{-2/3} \boldsymbol{\beta}_n) \left[(J_{n+1}^f)^{-1/3} \mathbf{f}_{n+1}^\top \right] \\ &= J_{n+1}^{-2/3} (\mathbf{F}_{n+1} \mathbf{F}_n^{-1}) \boldsymbol{\beta}_n (\mathbf{F}_n^{-\top} \mathbf{F}_{n+1}^\top) = J_{n+1}^{-2/3} \mathbf{F}_{n+1} \boldsymbol{\Gamma}_n \mathbf{F}_{n+1}^\top \end{aligned} \quad (\text{B.11})$$

where we define $\boldsymbol{\Gamma}_n = \mathbf{F}_n^{-1} \boldsymbol{\beta}_n \mathbf{F}_n^{-\top}$. Next, we derive

$$\text{tr} \left(\bar{\mathbf{f}}_{n+1} \bar{\boldsymbol{\beta}}_n \bar{\mathbf{f}}_{n+1}^\top \right) = J_{n+1}^{-2/3} \boldsymbol{\Gamma}_n : \mathbf{C}_{n+1}$$

and

$$\frac{\partial}{\partial \mathbf{C}_{n+1}} \text{tr} \left(\bar{\mathbf{f}}_{n+1} \bar{\boldsymbol{\beta}}_n \bar{\mathbf{f}}_{n+1}^\top \right) = J_{n+1}^{-2/3} \left[\boldsymbol{\Gamma}_n - \frac{1}{3} (\boldsymbol{\Gamma}_n : \mathbf{C}_{n+1}) \mathbf{C}_{n+1}^{-1} \right] \quad (\text{B.12})$$

in a similar vein as (B.10). Substituting (B.10) and (B.12) into (B.9) renders

$$\frac{\partial \bar{\mu}_{n+1}^{\text{tr}}}{\partial \mathbf{C}_{n+1}} = \frac{\mu}{3} J_{n+1}^{-2/3} \left\{ (\mathbf{C}_n^{\text{p}})^{-1} - \frac{1}{3} \left[(\mathbf{C}_n^{\text{p}})^{-1} : \mathbf{C}_{n+1} \right] \mathbf{C}_{n+1}^{-1} \right\} - \frac{1}{3} J_{n+1}^{-2/3} \left[\boldsymbol{\Gamma}_n - \frac{1}{3} (\boldsymbol{\Gamma}_n : \mathbf{C}_{n+1}) \mathbf{C}_{n+1}^{-1} \right].$$

For simplification, we further apply the push-forward operator (φ_*) and compute

$$\begin{aligned} \varphi_* \left(\frac{\partial \bar{\mu}_{n+1}^{\text{tr}}}{\partial \mathbf{C}_{n+1}} \right) &= \frac{\mu}{3} \left[\bar{\mathbf{f}}_{n+1} \bar{\mathbf{b}}_n^{\text{e, tr}} \bar{\mathbf{f}}_{n+1}^\top - \frac{1}{3} \text{tr} \left(\bar{\mathbf{f}}_{n+1} \bar{\mathbf{b}}_n^{\text{e, tr}} \bar{\mathbf{f}}_{n+1}^\top \right) \mathbf{I} \right] - \frac{1}{3} \left[\bar{\mathbf{f}}_{n+1} \bar{\boldsymbol{\beta}}_n \bar{\mathbf{f}}_{n+1}^\top - \frac{1}{3} \text{tr} \left(\bar{\mathbf{f}}_{n+1} \bar{\boldsymbol{\beta}}_n \bar{\mathbf{f}}_{n+1}^\top \right) \mathbf{I} \right] \\ &= \frac{\mu}{3} \text{dev} \left(\bar{\mathbf{f}}_{n+1} \bar{\mathbf{b}}_n^{\text{e, tr}} \bar{\mathbf{f}}_{n+1}^\top \right) - \frac{1}{3} \text{dev} \left(\bar{\mathbf{f}}_{n+1} \bar{\boldsymbol{\beta}}_n \bar{\mathbf{f}}_{n+1}^\top \right) = \frac{\mu}{3} \text{dev} \left(\bar{\mathbf{b}}_{n+1}^{\text{e, tr}} \right) - \frac{1}{3} \text{dev} \left(\bar{\boldsymbol{\beta}}_{n+1}^{\text{tr}} \right) \\ &= \frac{1}{3} \left[\mathbf{s}_{n+1}^{\text{tr}} - \text{dev} \left(\bar{\boldsymbol{\beta}}_{n+1}^{\text{tr}} \right) \right] = \frac{1}{3} \boldsymbol{\xi}_{n+1}^{\text{tr}} \end{aligned}$$

by using (B.4) and (B.11). Finally, we derive

$$\frac{\partial \bar{\mu}_{n+1}^{\text{tr}}}{\partial \mathbf{C}_{n+1}} = \frac{1}{3} \varphi^* \left(\boldsymbol{\xi}_{n+1}^{\text{tr}} \right). \quad (\text{B.13})$$

Appendix B.4. The computation of $\partial\hat{\gamma}_{n+1}/\partial\mathbf{C}_{n+1}$

Recall the consistency parameter, $\hat{\gamma}_{n+1}$, is governed by the algebraic equation, $\mathcal{G}(\hat{\gamma}_{n+1}) = 0$ in (21). Taking the derivatives on (21) yields

$$\frac{\partial\|\boldsymbol{\xi}_{n+1}^{\text{tr}}\|}{\partial\mathbf{C}_{n+1}} - 2\left(1 + \frac{h}{3\mu}\right)\hat{\gamma}_{n+1}\frac{\partial\bar{\mu}_{n+1}^{\text{tr}}}{\partial\mathbf{C}_{n+1}} - 2\bar{\mu}_{n+1}^{\text{tr}}\left(1 + \frac{h}{3\mu}\right)\frac{\partial\hat{\gamma}_{n+1}}{\partial\mathbf{C}_{n+1}} - \frac{2k'}{3}\frac{\partial\hat{\gamma}_{n+1}}{\partial\mathbf{C}_{n+1}} = 0, \quad (\text{B.14})$$

and one apparent next step is to compute $\partial\|\boldsymbol{\xi}_{n+1}^{\text{tr}}\|/\partial\mathbf{C}_{n+1}$. To this end, we consider

$$\|\boldsymbol{\xi}_{n+1}^{\text{tr}}\|^2 = \boldsymbol{\xi}_{n+1}^{\text{tr}} : \boldsymbol{\xi}_{n+1}^{\text{tr}} = \varphi_* [\varphi^*(\boldsymbol{\xi}_{n+1}^{\text{tr}})] : \varphi_* [\varphi^*(\boldsymbol{\xi}_{n+1}^{\text{tr}})] = [\mathbf{C}_{n+1}\varphi^*(\boldsymbol{\xi}_{n+1}^{\text{tr}})] : [\mathbf{C}_{n+1}\varphi^*(\boldsymbol{\xi}_{n+1}^{\text{tr}})]$$

and derive

$$\frac{\partial\|\boldsymbol{\xi}_{n+1}^{\text{tr}}\|^2}{\partial\mathbf{C}_{n+1}} = 2[\mathbf{C}_{n+1}\varphi^*(\boldsymbol{\xi}_{n+1}^{\text{tr}})\mathbf{C}_{n+1}] : \frac{\partial\varphi^*(\boldsymbol{\xi}_{n+1}^{\text{tr}})}{\partial\mathbf{C}_{n+1}} + 2\varphi^*(\boldsymbol{\xi}_{n+1}^{\text{tr}})\mathbf{C}_{n+1}\varphi^*(\boldsymbol{\xi}_{n+1}^{\text{tr}}). \quad (\text{B.15})$$

Following the derivation of $\partial\varphi^*(\mathbf{s}_{n+1}^{\text{tr}})/\partial\mathbf{C}_{n+1}$ from (B.8), we compute

$$\frac{\partial\varphi^*(\bar{\boldsymbol{\beta}}_{n+1}^{\text{tr}})}{\partial\mathbf{C}_{n+1}} = \frac{1}{3}\text{tr}\left(\bar{\mathbf{f}}_{n+1}\bar{\boldsymbol{\beta}}_n\bar{\mathbf{f}}_{n+1}^\top\right)\left(\mathbb{I}_{\mathbf{C}_{n+1}^{-1}} - \frac{1}{3}\mathbf{C}_{n+1}^{-1} \otimes \mathbf{C}_{n+1}^{-1}\right) - \frac{1}{3}\left[\varphi^*(\bar{\boldsymbol{\beta}}_{n+1}^{\text{tr}}) \otimes \mathbf{C}_{n+1}^{-1} + \mathbf{C}_{n+1}^{-1} \otimes \varphi^*(\bar{\boldsymbol{\beta}}_{n+1}^{\text{tr}})\right]$$

and further derive

$$\begin{aligned} \frac{\partial\varphi^*(\boldsymbol{\xi}_{n+1}^{\text{tr}})}{\partial\mathbf{C}_{n+1}} &= \frac{\partial\varphi^*(\mathbf{s}_{n+1}^{\text{tr}})}{\partial\mathbf{C}_{n+1}} - \frac{\partial\varphi^*(\bar{\boldsymbol{\beta}}_{n+1}^{\text{tr}})}{\partial\mathbf{C}_{n+1}} \\ &= \bar{\mu}_{n+1}^{\text{tr}}\left(\mathbb{I}_{\mathbf{C}_{n+1}^{-1}} - \frac{1}{3}\mathbf{C}_{n+1}^{-1} \otimes \mathbf{C}_{n+1}^{-1}\right) - \frac{1}{3}\left[\varphi^*(\boldsymbol{\xi}_{n+1}^{\text{tr}}) \otimes \mathbf{C}_{n+1}^{-1} + \mathbf{C}_{n+1}^{-1} \otimes \varphi^*(\boldsymbol{\xi}_{n+1}^{\text{tr}})\right]. \end{aligned} \quad (\text{B.16})$$

Substituting (B.16) into (B.15) and applying the push-forward operator (φ_*) yield

$$\varphi_*\left(\frac{\partial\|\boldsymbol{\xi}_{n+1}^{\text{tr}}\|^2}{\partial\mathbf{C}_{n+1}}\right) = 2\bar{\mu}_{n+1}^{\text{tr}}\boldsymbol{\xi}_{n+1}^{\text{tr}} - \frac{2}{3}\|\boldsymbol{\xi}_{n+1}^{\text{tr}}\|^2\mathbf{I} + 2(\boldsymbol{\xi}_{n+1}^{\text{tr}})^2.$$

Considering

$$\frac{\partial\|\boldsymbol{\xi}_{n+1}^{\text{tr}}\|^2}{\partial\mathbf{C}_{n+1}} = \frac{\partial\|\boldsymbol{\xi}_{n+1}^{\text{tr}}\|^2}{\partial\|\boldsymbol{\xi}_{n+1}^{\text{tr}}\|} \frac{\partial\|\boldsymbol{\xi}_{n+1}^{\text{tr}}\|}{\partial\mathbf{C}_{n+1}} = 2\|\boldsymbol{\xi}_{n+1}^{\text{tr}}\| \frac{\partial\|\boldsymbol{\xi}_{n+1}^{\text{tr}}\|}{\partial\mathbf{C}_{n+1}} \quad \Rightarrow \quad \frac{\partial\|\boldsymbol{\xi}_{n+1}^{\text{tr}}\|}{\partial\mathbf{C}_{n+1}} = \frac{1}{2\|\boldsymbol{\xi}_{n+1}^{\text{tr}}\|} \frac{\partial\|\boldsymbol{\xi}_{n+1}^{\text{tr}}\|^2}{\partial\mathbf{C}_{n+1}},$$

we derive

$$\varphi_*\left(\frac{\partial\|\boldsymbol{\xi}_{n+1}^{\text{tr}}\|}{\partial\mathbf{C}_{n+1}}\right) = \bar{\mu}_{n+1}^{\text{tr}}\mathbf{n}_{n+1} - \frac{1}{3}\|\boldsymbol{\xi}_{n+1}^{\text{tr}}\|(\mathbf{n}_{n+1} : \mathbf{n}_{n+1})\mathbf{I} + \|\boldsymbol{\xi}_{n+1}^{\text{tr}}\|\mathbf{n}_{n+1}^2.$$

We remark that the term $\varphi_*(\partial\|\boldsymbol{\xi}_{n+1}^{\text{tr}}\|/\partial\mathbf{C}_{n+1})$ is deviatoric by noticing

$$\text{tr}\left[\varphi_*\left(\frac{\partial\|\boldsymbol{\xi}_{n+1}^{\text{tr}}\|}{\partial\mathbf{C}_{n+1}}\right)\right] = \bar{\mu}_{n+1}^{\text{tr}}\text{tr}(\mathbf{n}_{n+1}) - \frac{1}{3}\|\boldsymbol{\xi}_{n+1}^{\text{tr}}\|\mathbf{n}_{n+1} : \mathbf{n}_{n+1}\text{tr}(\mathbf{I}) + \|\boldsymbol{\xi}_{n+1}^{\text{tr}}\|\text{tr}(\mathbf{n}_{n+1}^2) = 0.$$

Consequently, we can rewrite

$$\varphi_*\left(\frac{\partial\|\boldsymbol{\xi}_{n+1}^{\text{tr}}\|}{\partial\mathbf{C}_{n+1}}\right) = \text{dev}\left[\varphi_*\left(\frac{\partial\|\boldsymbol{\xi}_{n+1}^{\text{tr}}\|}{\partial\mathbf{C}_{n+1}}\right)\right] = \bar{\mu}_{n+1}^{\text{tr}}\mathbf{n}_{n+1} + \|\boldsymbol{\xi}_{n+1}^{\text{tr}}\|\text{dev}(\mathbf{n}_{n+1}^2),$$

which renders

$$\frac{\partial\|\boldsymbol{\xi}_{n+1}^{\text{tr}}\|}{\partial\mathbf{C}_{n+1}} = \varphi_*\left[\bar{\mu}_{n+1}^{\text{tr}}\mathbf{n}_{n+1} + \|\boldsymbol{\xi}_{n+1}^{\text{tr}}\|\text{dev}(\mathbf{n}_{n+1}^2)\right] = \bar{\mu}_{n+1}^{\text{tr}}\varphi^*(\mathbf{n}_{n+1}) + \|\boldsymbol{\xi}_{n+1}^{\text{tr}}\|\varphi^*[\text{dev}(\mathbf{n}_{n+1}^2)]. \quad (\text{B.17})$$

Finally, substituting (B.13) and (B.17) into (B.14) yields

$$\begin{aligned}
\frac{\partial \hat{\gamma}_{n+1}}{\partial \mathbf{C}_{n+1}} &= \frac{1}{2c_0 \bar{\mu}_{n+1}^{\text{tr}}} \left[\frac{\partial \|\boldsymbol{\xi}_{n+1}^{\text{tr}}\|}{\partial \mathbf{C}_{n+1}} - 2 \left(1 + \frac{h}{3\mu} \right) \hat{\gamma}_{n+1} \frac{\partial \bar{\mu}_{n+1}^{\text{tr}}}{\partial \mathbf{C}_{n+1}} \right] \\
&= \frac{1}{2c_0 \bar{\mu}_{n+1}^{\text{tr}}} \left\{ \bar{\mu}_{n+1}^{\text{tr}} \varphi^*(\mathbf{n}_{n+1}) + \|\boldsymbol{\xi}_{n+1}^{\text{tr}}\| \varphi^* [\text{dev}(\mathbf{n}_{n+1}^2)] - 2 \left(1 + \frac{h}{3\mu} \right) \hat{\gamma}_{n+1} \left[\frac{1}{3} \varphi^*(\boldsymbol{\xi}_{n+1}^{\text{tr}}) \right] \right\} \\
&= \frac{1}{2c_0 \bar{\mu}_{n+1}^{\text{tr}}} \left\{ \left[\bar{\mu}_{n+1}^{\text{tr}} - \frac{2}{3} \left(1 + \frac{h}{3\mu} \right) \hat{\gamma}_{n+1} \|\boldsymbol{\xi}_{n+1}^{\text{tr}}\| \right] \varphi^*(\mathbf{n}_{n+1}) + \|\boldsymbol{\xi}_{n+1}^{\text{tr}}\| \varphi^* [\text{dev}(\mathbf{n}_{n+1}^2)] \right\}
\end{aligned} \tag{B.18}$$

where we define

$$c_0 = 1 + \frac{h}{3\mu} + \frac{k'}{3\bar{\mu}_{n+1}^{\text{tr}}}.$$

Appendix B.5. The computation of $\partial \varphi^*(\mathbf{n}_{n+1})/\partial \mathbf{C}_{n+1}$

Based on the chain rules, we write out

$$\frac{\partial \varphi^*(\mathbf{n}_{n+1})}{\partial \mathbf{C}_{n+1}} = \frac{\partial}{\partial \mathbf{C}_{n+1}} \left[\frac{\varphi^*(\boldsymbol{\xi}_{n+1}^{\text{tr}})}{\|\boldsymbol{\xi}_{n+1}^{\text{tr}}\|} \right] = \frac{1}{\|\boldsymbol{\xi}_{n+1}^{\text{tr}}\|^2} \left[\|\boldsymbol{\xi}_{n+1}^{\text{tr}}\| \frac{\partial \varphi^*(\boldsymbol{\xi}_{n+1}^{\text{tr}})}{\partial \mathbf{C}_{n+1}} - \varphi^*(\boldsymbol{\xi}_{n+1}^{\text{tr}}) \otimes \frac{\partial \|\boldsymbol{\xi}_{n+1}^{\text{tr}}\|}{\partial \mathbf{C}_{n+1}} \right]. \tag{B.19}$$

Substituting (B.17) and (B.16) into (B.19) renders

$$\begin{aligned}
\frac{\partial \varphi^*(\mathbf{n}_{n+1})}{\partial \mathbf{C}_{n+1}} &= \frac{\bar{\mu}_{n+1}^{\text{tr}}}{\|\boldsymbol{\xi}_{n+1}^{\text{tr}}\|} \left(\mathbb{I}_{\mathbf{C}_{n+1}^{-1}} - \frac{1}{3} \mathbf{C}_{n+1}^{-1} \otimes \mathbf{C}_{n+1}^{-1} \right) - \frac{1}{3} [\varphi^*(\mathbf{n}_{n+1}) \otimes \mathbf{C}_{n+1}^{-1} + \mathbf{C}_{n+1}^{-1} \otimes \varphi^*(\mathbf{n}_{n+1})] \\
&\quad - \frac{\bar{\mu}_{n+1}^{\text{tr}}}{\|\boldsymbol{\xi}_{n+1}^{\text{tr}}\|} \varphi^*(\mathbf{n}_{n+1}) \otimes \varphi^*(\mathbf{n}_{n+1}) - \varphi^*(\mathbf{n}_{n+1}) \otimes \varphi^* [\text{dev}(\mathbf{n}_{n+1}^2)].
\end{aligned} \tag{B.20}$$

Appendix B.6. Complete expression of the second elastoplastic moduli

Substituting $\partial \varphi^*(\boldsymbol{\tau}_{n+1}^{\text{vol}})/\partial \mathbf{C}_{n+1}$ from (B.3), $\partial \varphi^*(\mathbf{s}_{n+1}^{\text{tr}})/\partial \mathbf{C}_{n+1}$ from (B.8), $\partial \bar{\mu}_{n+1}^{\text{tr}}/\partial \mathbf{C}_{n+1}$ from (B.13), $\partial \hat{\gamma}_{n+1}/\partial \mathbf{C}_{n+1}$ from (B.18), and $\partial \varphi^*(\mathbf{n}_{n+1})/\partial \mathbf{C}_{n+1}$ from (B.20) into (B.1), we finally derive

$$\begin{aligned}
\mathbb{C}_{n+1}^{\text{ep}} &= J_{n+1} (J_{n+1} U'_{n+1})' \mathbf{C}_{n+1}^{-1} \otimes \mathbf{C}_{n+1}^{-1} - 2 J_{n+1} U'_{n+1} \mathbb{I}_{\mathbf{C}_{n+1}^{-1}} \\
&\quad + 2 \bar{\mu}_{n+1}^{\text{tr}} \left(\mathbb{I}_{\mathbf{C}_{n+1}^{-1}} - \frac{1}{3} \mathbf{C}_{n+1}^{-1} \otimes \mathbf{C}_{n+1}^{-1} \right) - \frac{2}{3} [\varphi^*(\mathbf{s}_{n+1}^{\text{tr}}) \otimes \mathbf{C}_{n+1}^{-1} + \mathbf{C}_{n+1}^{-1} \otimes \varphi^*(\mathbf{s}_{n+1}^{\text{tr}})] \\
&\quad - \frac{4}{3} \hat{\gamma}_{n+1} \|\boldsymbol{\xi}_{n+1}^{\text{tr}}\| \varphi^*(\mathbf{n}_{n+1}) \otimes \varphi^*(\mathbf{n}_{n+1}) \\
&\quad - \frac{2}{c_0} \varphi^*(\mathbf{n}_{n+1}) \otimes \left\{ \left[\bar{\mu}_{n+1}^{\text{tr}} - \frac{2}{3} \left(1 + \frac{h}{3\mu} \right) \hat{\gamma}_{n+1} \|\boldsymbol{\xi}_{n+1}^{\text{tr}}\| \right] \varphi^*(\mathbf{n}_{n+1}) + \|\boldsymbol{\xi}_{n+1}^{\text{tr}}\| \varphi^* [\text{dev}(\mathbf{n}_{n+1}^2)] \right\} \\
&\quad - \frac{4 \left(\bar{\mu}_{n+1}^{\text{tr}} \right)^2 \hat{\gamma}_{n+1}}{\|\boldsymbol{\xi}_{n+1}^{\text{tr}}\|} \left(\mathbb{I}_{\mathbf{C}_{n+1}^{-1}} - \frac{1}{3} \mathbf{C}_{n+1}^{-1} \otimes \mathbf{C}_{n+1}^{-1} \right) \\
&\quad + \frac{4 \bar{\mu}_{n+1}^{\text{tr}} \hat{\gamma}_{n+1}}{3} [\varphi^*(\mathbf{n}_{n+1}) \otimes \mathbf{C}_{n+1}^{-1} + \mathbf{C}_{n+1}^{-1} \otimes \varphi^*(\mathbf{n}_{n+1})] \\
&\quad + \frac{4 \left(\bar{\mu}_{n+1}^{\text{tr}} \right)^2 \hat{\gamma}_{n+1}}{\|\boldsymbol{\xi}_{n+1}^{\text{tr}}\|} \varphi^*(\mathbf{n}_{n+1}) \otimes \varphi^*(\mathbf{n}_{n+1}) + 4 \bar{\mu}_{n+1}^{\text{tr}} \hat{\gamma}_{n+1} \varphi^*(\mathbf{n}_{n+1}) \otimes \varphi^* [\text{dev}(\mathbf{n}_{n+1}^2)].
\end{aligned}$$

Regrouping terms renders

$$\begin{aligned} \mathbf{C}_{n+1}^{\text{ep}} = & \left(2\bar{\mu}_{n+1}^{\text{tr}} - 2c_1\bar{\mu}_{n+1}^{\text{tr}} - 2J_{n+1}U'_{n+1} \right) \mathbb{I}_{\mathbf{C}_{n+1}^{-1}} + \left[J_{n+1}(J_{n+1}U'_{n+1})' - \frac{2\bar{\mu}_{n+1}^{\text{tr}}}{3} + \frac{2c_1\bar{\mu}_{n+1}^{\text{tr}}}{3} \right] \mathbf{C}_{n+1}^{-1} \otimes \mathbf{C}_{n+1}^{-1} \\ & - \frac{2}{3} [\varphi^*(\mathbf{s}_{n+1}^{\text{tr}}) \otimes \mathbf{C}_{n+1}^{-1} + \mathbf{C}_{n+1}^{-1} \otimes \varphi^*(\mathbf{s}_{n+1}^{\text{tr}})] + \frac{2c_1}{3} [\varphi^*(\boldsymbol{\xi}_{n+1}^{\text{tr}}) \otimes \mathbf{C}_{n+1}^{-1} + \mathbf{C}_{n+1}^{-1} \otimes \varphi^*(\boldsymbol{\xi}_{n+1}^{\text{tr}})] \\ & - c_3\varphi^*(\mathbf{n}_{n+1}) \otimes \varphi^*(\mathbf{n}_{n+1}) - c_4\varphi^*(\mathbf{n}_{n+1}) \otimes \varphi^*[\text{dev}(\mathbf{n}_{n+1}^2)]. \end{aligned}$$

with c_1 , c_3 , and c_4 defined in (29). To ensure the major symmetry of $\mathbf{C}_{n+1}^{\text{ep}}$ for computational benefits, we manually symmetrize its last term by following Simo (1988b) and derive the expression in (28).

Appendix C. Verification of FEA implementation for finite strain elastoplasticity

In this section, we compare the FEA and semi-analytical solutions for a 3D column under uniaxial cyclic loadings. Through this comparison, we aim to demonstrate that the proposed formulae for updating $\bar{\mathbf{b}}^e$ in (17) ensure the isochoric plastic flow ($J^P = 1$), and consequently, the FEA solution matches the semi-analytical solution exactly.

Appendix C.1. Construction of the semi-analytical solution

For the simplicity of the semi-analytical solution, we assume no hardening occurs ($k(\alpha) \equiv \sigma_y$ and $h = 0$) when the material yields. At any time, the deformation gradients can be expressed as

$$\mathbf{F} = \begin{bmatrix} \lambda & & \\ & \lambda^1 & \\ & & \lambda^1 \end{bmatrix}, \quad \mathbf{F}^P = \begin{bmatrix} \lambda^P & & \\ & \frac{1}{\sqrt{\lambda^P}} & \\ & & \frac{1}{\sqrt{\lambda^P}} \end{bmatrix}, \quad \text{and} \quad \mathbf{F}^e = \begin{bmatrix} \frac{\lambda}{\lambda^P} & & \\ & \lambda^1\sqrt{\lambda^P} & \\ & & \lambda^1\sqrt{\lambda^P} \end{bmatrix}.$$

Here, the variables λ , λ^1 , and λ^P represent the total applied stretch, total lateral stretch, and plastic stretch (Fig. C.13(a)), respectively. Note that the above deformation gradients satisfy the requirements of $\mathbf{F} = \mathbf{F}^e\mathbf{F}^P$ and $\det(\mathbf{F}^P) = 1$. Based on the elastic deformation gradient (\mathbf{F}^e), we compute

$$\text{dev}(\bar{\mathbf{b}}^e) = \frac{1}{3} \left[\lambda^P \left(\frac{\lambda^1}{\lambda} \right)^{2/3} - \frac{1}{(\lambda^P)^2} \left(\frac{\lambda}{\lambda^1} \right)^{4/3} \right] \begin{bmatrix} -2 & & \\ & 1 & \\ & & 1 \end{bmatrix}$$

and derive the components of the Kirchhoff stress tensor ($\boldsymbol{\tau}$) as

$$\begin{cases} \tau_{11} = JU'(J) - \frac{2\mu}{3} \left[\lambda^P \left(\frac{\lambda^1}{\lambda} \right)^{2/3} - \frac{1}{(\lambda^P)^2} \left(\frac{\lambda}{\lambda^1} \right)^{4/3} \right], \\ \tau_{22} = \tau_{33} = JU'(J) + \frac{\mu}{3} \left[\lambda^P \left(\frac{\lambda^1}{\lambda} \right)^{2/3} - \frac{1}{(\lambda^P)^2} \left(\frac{\lambda}{\lambda^1} \right)^{4/3} \right], \end{cases}$$

where $J = \lambda(\lambda^1)^2$ is the total volume change.

During the elastic loading/unloading process, the Kirchhoff stress conforms to $\tau_{22} = \tau_{33} = 0$ for given λ and λ_p . We can then solve λ_l from

$$\frac{\kappa}{2} [\lambda^2(\lambda^1)^4 - 1] + \frac{\mu}{3} \left[\lambda^P \left(\frac{\lambda^1}{\lambda} \right)^{2/3} - \frac{1}{(\lambda^P)^2} \left(\frac{\lambda}{\lambda^1} \right)^{4/3} \right] = 0 \quad (\text{C.1})$$

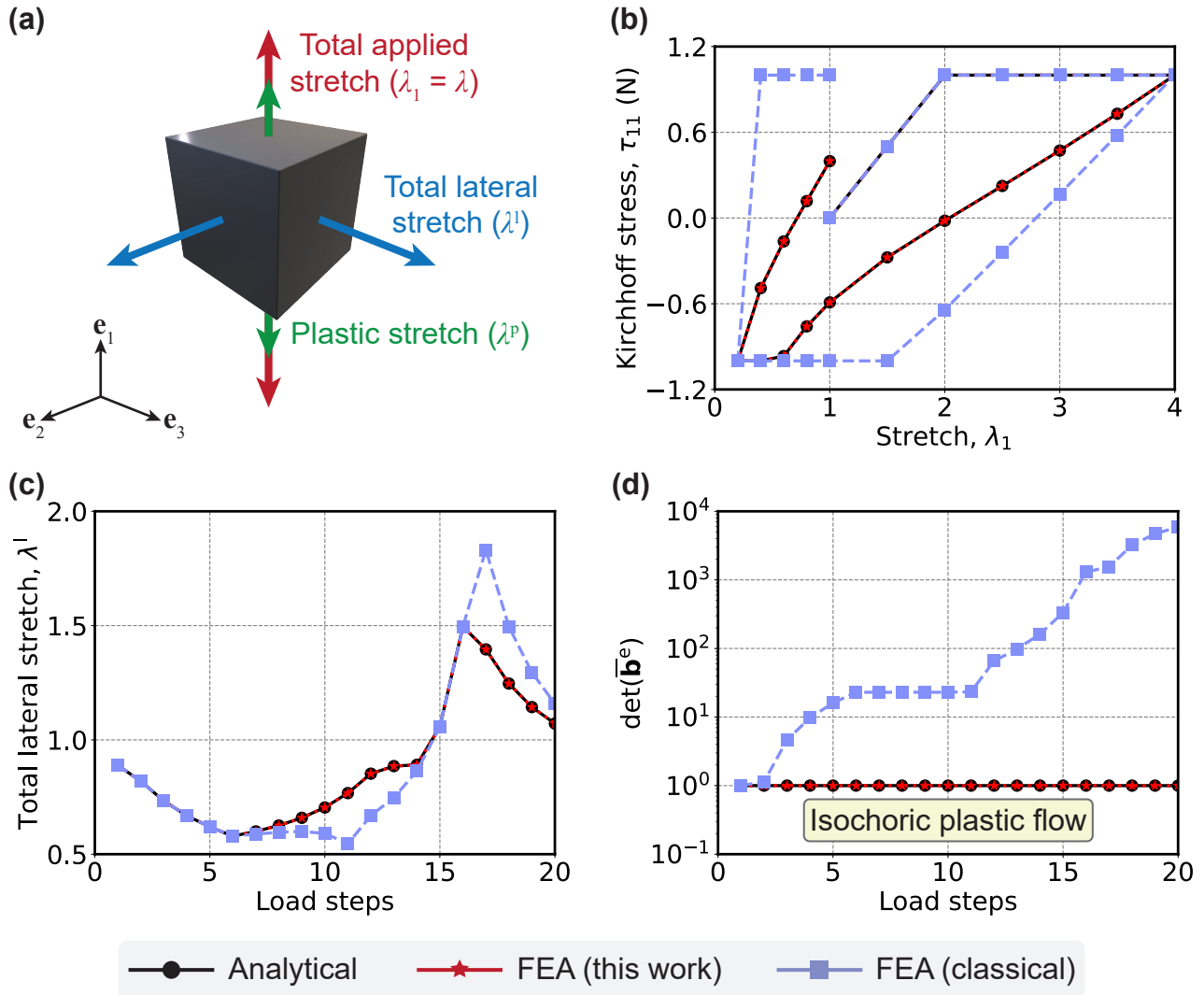


Figure C.13: Comparison between the FEA and semi-analytical solutions. (a) Tested mechanical setups. (b) Kirchoff stress–stretch (τ_{11} – λ_1) curves. (c) Evolution of the total lateral stretch (λ^l). (d) Evolution of the determinant of $\bar{\mathbf{b}}^e$.

with the choice of $U(J)$ in (5). When the material yields, the Kirchhoff stress satisfies $\tau_{11} = \pm\sigma_y$ (the sign depends on the loading direction) and $\tau_{22} = \tau_{33} = 0$ for given λ . We can then analytically compute λ^1 as

$$\lambda^1 = \frac{1}{\sqrt{\lambda}} \left(1 \pm \frac{2\sigma_y}{3\kappa} \right)^{1/4} \quad (\text{C.2})$$

and solve for λ^p from

$$\left(\frac{\lambda^1}{\lambda} \right)^{2/3} (\lambda^p)^3 \pm \frac{\sigma_y}{\mu} (\lambda^p)^2 - \left(\frac{\lambda}{\lambda^1} \right)^{4/3} = 0. \quad (\text{C.3})$$

Note that the expressions in (C.1), (C.2), and (C.3) construct the semi-analytical solutions for predicting the finite strain elastoplastic responses of materials under uniaxial cyclic loadings.

Appendix C.2. Comparison between the FEA and semi-analytical solutions

Next, we compare the semi-analytical solutions described above with the FEA predictions based on the theories in Section 2. As a reference, we also include FEA predictions derived from the classical theories in Simo (1988a,b) that utilize (14)₁ to update $\bar{\mathbf{b}}^e$. Without loss of generality, we adopt dummy material constants, $E = 1$ MPa, $\nu = 0.3$, and $\sigma_y = 0.2$ MPa, where E is the initial Young's modulus and ν is the initial Poisson's ratio.

The comparison results are shown in Figs. C.13(b)–(d), which illustrate the Kirchhoff stress component (τ_{11}), lateral stretch (λ^1), and the determinant of $\bar{\mathbf{b}}^e$, respectively. Based on the comparison, the FEA predictions in this work ensure isochoric plastic flow and demonstrate good agreement with the semi-analytical solutions, as evidenced by the small absolute 2-norm errors: 1.56×10^{-10} for τ_{11} , 7.76×10^{-11} for λ^1 , and 7.95×10^{-10} for $\det(\bar{\mathbf{b}}^e)$. Conversely, the classical FEA initially aligns well during the loading stage but fails to ensure isochoric plastic flow. It also leads to significant deviations from the analytical solutions after unloading occurs. This limitation renders the classical FEA unsuitable for structures experiencing non-monotonic loadings, such as the dampers under cyclic loadings discussed in Section 4.1.

Appendix D. Convergence, precision, and computational time of FEA

In this section, we examine the computational aspects of FEA, including convergence, precision, and computational time. Using the optimized damper under multiple-cycle loadings in Fig. 6 as an example, we present the required Newton iterations for convergence in Fig. D.14(a). For most load steps in FEA, whether during loading or unloading, convergence is achieved in fewer than 10 Newton iterations. However, at critical load steps corresponding to transitions between loading and unloading, it requires 10–25 iterations to converge.

To further illustrate the convergence and precision of FEA, we highlight four representative load steps in Fig. D.14(a) and show the evolution of the relative residual (right-hand side of (32)₁) at these steps in Fig. D.14(b). For most steps, such as steps 60 and 100, the residual converges quadratically due to the algorithmic elastoplastic moduli in (30) and the proposed interpolation schemes in (36) and (37). For transitional steps, like steps 66 and 156, a line search (Algorithm 3) is activated in the initial iterations to reduce the residual. Once the residual reduction trend is established, quadratic convergence resumes. Notably, as shown in Fig. D.14(b), the residuals for all load steps eventually converge to the prescribed tolerance (set to 10^{-8} here).

After discussing convergence and precision, we now focus on the computational time of FEA. For representativeness, we analyze the most complex design case in each example presented in Section 4. Computational performance is tested on a workstation equipped with an AMD Ryzen Threadripper PRO 3995WX CPU featuring 64 cores and 256 GB of memory. The results are summarized in Table D.2, where we provide the finite element, degree of freedom (DOF), and parallel process counts, along with the average computational time per Newton iteration in the final load step.

It is evident that the 2D designs (damper and beam) require less than 0.1 seconds per Newton iteration due to the parallel computing capabilities provided by FEniTop (Jia et al., 2024d). The profiled sheet takes

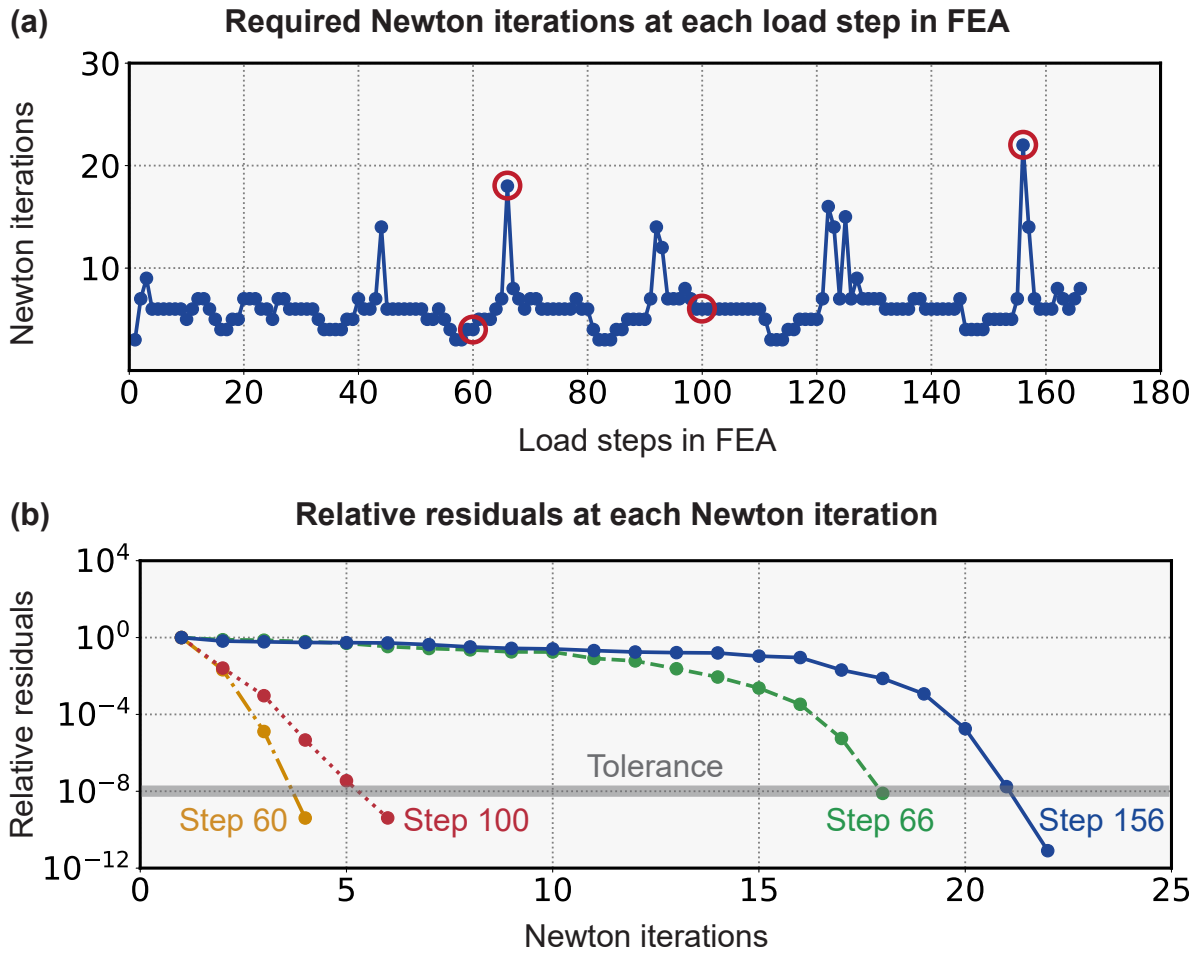


Figure D.14: Convergence and precision of FEA. (a) Required Newton iterations for convergence at each load step in FEA. (b) Evolution of the relative residuals at representative load steps marked in (a).

around 2 seconds per iteration, while the bumper design takes around 12 seconds per iteration due to a large DOF count. This high computational demand for the bumper can be reduced by exploiting symmetry and analyzing one quarter of the domain.

Table D.2: Computational time of FEA for representative design cases

| Optimized designs | Element counts | DOF counts | Process counts | Time per iteration |
|------------------------------------|----------------|------------|----------------|--------------------|
| Damper in Fig. 6 | 15,000 | 30,502 | 8 | 0.07 s |
| Beam (Dsg. 4) in Fig. 7 | 14,400 | 29,402 | 8 | 0.06 s |
| Bumper in Fig. 10 | 138,400 | 469,491 | 16 | 11.82 s |
| Profiled sheet (Dsg. 4) in Fig. 12 | 28,800 | 110,715 | 16 | 1.94 s |

Appendix E. History-dependent sensitivity analysis and verification

In this section, we present the sensitivity analysis for finite strain elastoplasticity. Following the blueprint provided in Jia et al. (2025), we begin by defining the global vectors for the design and state variables as well as the residuals. After that, we derive the sensitivity expressions with the reversed adjoint method and automatic differentiation. Finally, we verify the derived sensitivity expressions through a comparison with the forward finite difference scheme.

Appendix E.1. Global vectors of design variables, state variables, and residuals

In this subsection, we define the residual vectors used in the sensitivity analysis. Based on the local and global governing equations in Section 2, we identify five groups of independent state variables as $\bar{\mathbf{b}}_1^e, \dots, \bar{\mathbf{b}}_N^e$, $\bar{\boldsymbol{\beta}}_1, \dots, \bar{\boldsymbol{\beta}}_N$, $\alpha_1, \dots, \alpha_N$, $\hat{\gamma}_1, \dots, \hat{\gamma}_N$, and $\mathbf{u}_1, \dots, \mathbf{u}_N$. Correspondingly, we define five groups of residual expressions as

$$\left\{ \begin{array}{l} \mathbf{r}_{n+1}^{\bar{\mathbf{b}}^e}(\{\bar{\zeta}\}, \bar{\mathbf{b}}_{n+1}^e, \hat{\gamma}_{n+1}, \mathbf{u}_{n+1}, \bar{\mathbf{b}}_n^e, \bar{\boldsymbol{\beta}}_n, \mathbf{u}_n) = \bar{\mathbf{b}}_{n+1}^e - \text{dev}(\bar{\mathbf{b}}_{n+1}^{e, \text{tr}}) + \frac{2\bar{\mu}_{n+1}^{\text{tr}}}{\mu} \hat{\gamma}_{n+1} \mathbf{n}_{n+1} - \frac{1}{3} \mathcal{I}_1 \mathbf{I} = \mathbf{0}, \\ \mathbf{r}_{n+1}^{\bar{\boldsymbol{\beta}}}(\{\bar{\zeta}\}, \bar{\boldsymbol{\beta}}_{n+1}, \hat{\gamma}_{n+1}, \mathbf{u}_{n+1}, \bar{\mathbf{b}}_n^e, \bar{\boldsymbol{\beta}}_n, \mathbf{u}_n) = \bar{\boldsymbol{\beta}}_{n+1} - \bar{\boldsymbol{\beta}}_{n+1}^{\text{tr}} - \frac{2h\bar{\mu}_{n+1}^{\text{tr}}}{3\mu} \hat{\gamma}_{n+1} \mathbf{n}_{n+1} = \mathbf{0}, \\ r_{n+1}^\alpha(\alpha_{n+1}, \hat{\gamma}_{n+1}, \alpha_n) = \alpha_{n+1} - \alpha_{n+1}^{\text{tr}} - \sqrt{\frac{2}{3}} \hat{\gamma}_{n+1} = 0, \\ r_{n+1}^{\hat{\gamma}}(\{\bar{\zeta}\}, \hat{\gamma}_{n+1}, \mathbf{u}_{n+1}, \bar{\mathbf{b}}_n^e, \bar{\boldsymbol{\beta}}_n, \alpha_n, \mathbf{u}_n) \\ = \hat{\gamma}_{n+1} \mathcal{G}(\hat{\gamma}_{n+1}) = \hat{\gamma}_{n+1} \left[\|\boldsymbol{\xi}_{n+1}^{\text{tr}}\| - 2\bar{\mu}_{n+1}^{\text{tr}} \left(1 + \frac{h}{3\mu}\right) \hat{\gamma}_{n+1} - \sqrt{\frac{2}{3}} k \left(\alpha_{n+1}^{\text{tr}} + \sqrt{\frac{2}{3}} \hat{\gamma}_{n+1}\right) \right] = 0, \\ r_{n+1}^{\mathbf{u}}(\{\bar{\zeta}\}, \hat{\gamma}_{n+1}, \mathbf{u}_{n+1}, \bar{\mathbf{b}}_n^e, \bar{\boldsymbol{\beta}}_n, \mathbf{u}_n) = \int_{\Omega_0} \mathbf{P}_{n+1} : \nabla \mathbf{v} \, d\mathbf{X} - \int_{\Omega_0} \bar{\mathbf{q}}_{n+1} \cdot \mathbf{v} \, d\mathbf{X} - \int_{\partial\Omega_0^N} \bar{\mathbf{t}}_{n+1} \cdot \mathbf{v} \, d\mathbf{X} = 0, \end{array} \right. \quad (\text{E.1})$$

where $\{\bar{\zeta}\} = \{\bar{\rho}, \bar{\xi}_1, \dots, \bar{\xi}_{N^{\text{mat}}}\}$ is a collection of the physical design variables. We remark that, in contrast to Jia et al. (2025), here we treat $\hat{\gamma}_1, \dots, \hat{\gamma}_N$ as independent state variables and incorporate its residual in (E.1)₄. This treatment allows us to consider nonlinear isotropic hardening laws such as (13) where $\hat{\gamma}_1, \dots, \hat{\gamma}_N$ typically have no analytical expressions.

In the context of FEA, we reformulate (E.1) into global residual vectors expressed as

$$\begin{cases} \mathbf{R}_{n+1}^{\bar{\mathbf{b}}^e}(\{\bar{\boldsymbol{\zeta}}\}, \mathbf{V}_{n+1}^{\bar{\mathbf{b}}^e}, \mathbf{V}_{n+1}^{\hat{\boldsymbol{\gamma}}}, \mathbf{U}_{n+1}, \mathbf{V}_n^{\bar{\mathbf{b}}^e}, \mathbf{V}_n^{\bar{\boldsymbol{\beta}}}, \mathbf{U}_n) = \mathbf{0}, \\ \mathbf{R}_{n+1}^{\bar{\boldsymbol{\beta}}}(\{\bar{\boldsymbol{\zeta}}\}, \mathbf{V}_{n+1}^{\bar{\boldsymbol{\beta}}}, \mathbf{V}_{n+1}^{\hat{\boldsymbol{\gamma}}}, \mathbf{U}_{n+1}, \mathbf{V}_n^{\bar{\mathbf{b}}^e}, \mathbf{V}_n^{\bar{\boldsymbol{\beta}}}, \mathbf{U}_n) = \mathbf{0}, \\ \mathbf{R}_{n+1}^{\alpha}(\mathbf{V}_{n+1}^{\alpha}, \mathbf{V}_{n+1}^{\hat{\boldsymbol{\gamma}}}, \mathbf{V}_n^{\alpha}) = \mathbf{0}, \\ \mathbf{R}_{n+1}^{\hat{\boldsymbol{\gamma}}}(\{\bar{\boldsymbol{\zeta}}\}, \mathbf{V}_{n+1}^{\hat{\boldsymbol{\gamma}}}, \mathbf{U}_{n+1}, \mathbf{V}_n^{\bar{\mathbf{b}}^e}, \mathbf{V}_n^{\bar{\boldsymbol{\beta}}}, \mathbf{V}_n^{\alpha}, \mathbf{U}_n) = \mathbf{0}, \\ \mathbf{R}_{n+1}^{\mathbf{u}}(\{\bar{\boldsymbol{\zeta}}\}, \mathbf{V}_{n+1}^{\hat{\boldsymbol{\gamma}}}, \mathbf{U}_{n+1}, \mathbf{V}_n^{\bar{\mathbf{b}}^e}, \mathbf{V}_n^{\bar{\boldsymbol{\beta}}}, \mathbf{U}_n) = \mathbf{0}. \end{cases}$$

In these expressions, we define $\{\bar{\boldsymbol{\zeta}}\} = \{\bar{\boldsymbol{\rho}}, \bar{\boldsymbol{\xi}}_1, \dots, \bar{\boldsymbol{\xi}}_{N^{\text{mat}}}\}$ as a collection of global vectors of physical design variables, where $\bar{\zeta}_e$ is the physical design variable of finite element e . Additionally, the variable $\mathbf{V}_n^{\bar{\mathbf{b}}^e}$ for $n = 1, \dots, N$ is the global vector of $\bar{\mathbf{b}}_n^e$ defined as

$$\mathbf{V}_n^{\bar{\mathbf{b}}^e} = \left[\left(\bar{\mathbf{b}}_{n,1}^{\mathbf{e},\mathbf{v}} \right)^\top, \dots, \left(\bar{\mathbf{b}}_{n,N^{\text{pt}}}^{\mathbf{e},\mathbf{v}} \right)^\top \right]^\top$$

where $\bar{\mathbf{b}}_{n,i}^{\mathbf{e},\mathbf{v}}$ for $i = 1, \dots, N^{\text{pt}}$ is the vector form of $\bar{\mathbf{b}}_{n,i}^e$ expressed as

$$\bar{\mathbf{b}}_{n,i}^{\mathbf{e},\mathbf{v}} = \left[\left(\bar{\mathbf{b}}_{n,i}^e \right)_{11}, \left(\bar{\mathbf{b}}_{n,i}^e \right)_{12}, \left(\bar{\mathbf{b}}_{n,i}^e \right)_{13}, \left(\bar{\mathbf{b}}_{n,i}^e \right)_{22}, \left(\bar{\mathbf{b}}_{n,i}^e \right)_{23}, \left(\bar{\mathbf{b}}_{n,i}^e \right)_{33} \right]^\top.$$

Here, subscript i is the count of integration points used in FEA, and N^{pt} is the number of all integration points. Similarly, the variable $\mathbf{V}_n^{\bar{\boldsymbol{\beta}}}$ for $n = 1, \dots, N$ is the global vector of $\bar{\boldsymbol{\beta}}_n$ defined as

$$\mathbf{V}_n^{\bar{\boldsymbol{\beta}}} = \left[\left(\bar{\boldsymbol{\beta}}_{n,1}^{\mathbf{v}} \right)^\top, \dots, \left(\bar{\boldsymbol{\beta}}_{n,N^{\text{pt}}}^{\mathbf{v}} \right)^\top \right]^\top$$

where $\bar{\boldsymbol{\beta}}_{n,i}^{\mathbf{v}}$ for $i = 1, \dots, N^{\text{pt}}$ is the vector form of $\bar{\boldsymbol{\beta}}_{n,i}$ expressed as

$$\bar{\boldsymbol{\beta}}_{n,i}^{\mathbf{v}} = \left[\left(\bar{\boldsymbol{\beta}}_{n,i} \right)_{11}, \left(\bar{\boldsymbol{\beta}}_{n,i} \right)_{12}, \left(\bar{\boldsymbol{\beta}}_{n,i} \right)_{13}, \left(\bar{\boldsymbol{\beta}}_{n,i} \right)_{22}, \left(\bar{\boldsymbol{\beta}}_{n,i} \right)_{23}, \left(\bar{\boldsymbol{\beta}}_{n,i} \right)_{33} \right]^\top.$$

The variables \mathbf{V}_n^{α} and $\mathbf{V}_n^{\hat{\boldsymbol{\gamma}}}$ for $n = 1, \dots, N$ are the global vectors of α_n and $\hat{\boldsymbol{\gamma}}_n$, respectively, which are defined as

$$\mathbf{V}_n^{\alpha} = [\alpha_{n,1}, \dots, \alpha_{n,N^{\text{pt}}}]^\top \quad \text{and} \quad \mathbf{V}_n^{\hat{\boldsymbol{\gamma}}} = [\hat{\gamma}_{n,1}, \dots, \hat{\gamma}_{n,N^{\text{pt}}}]^\top.$$

Finally, the variable \mathbf{U}_n for $n = 1, \dots, N$ is the global vector of \mathbf{u}_n defined as

$$\mathbf{U}_n = [(\mathbf{u}_n)_{1,x}, (\mathbf{u}_n)_{1,y}, (\mathbf{u}_n)_{1,z}, \dots, (\mathbf{u}_n)_{N^{\text{node}},x}, (\mathbf{u}_n)_{N^{\text{node}},y}, (\mathbf{u}_n)_{N^{\text{node}},z}]^\top$$

where subscripts x , y , and z represent the three components of $(\mathbf{u}_n)_j$ for $j = 1, \dots, N^{\text{node}}$, and N^{node} is the number of nodes in FEA.

Appendix E.2. Sensitivity analysis

After defining the global vectors of design variables ($\bar{\boldsymbol{\rho}}$ and $\bar{\boldsymbol{\xi}}_1, \dots, \bar{\boldsymbol{\xi}}_{N^{\text{mat}}}$), state variables ($\mathbf{V}_n^{\bar{\mathbf{b}}^e}$, $\mathbf{V}_n^{\bar{\boldsymbol{\beta}}}$, \mathbf{V}_n^{α} , $\mathbf{V}_n^{\hat{\boldsymbol{\gamma}}}$, and \mathbf{U}_n), and residuals ($\mathbf{R}_{n+1}^{\bar{\mathbf{b}}^e}$, $\mathbf{R}_{n+1}^{\bar{\boldsymbol{\beta}}}$, $\mathbf{R}_{n+1}^{\alpha}$, $\mathbf{R}_{n+1}^{\hat{\boldsymbol{\gamma}}}$, and $\mathbf{R}_{n+1}^{\mathbf{u}}$), we proceed with the sensitivity analysis for finite strain elastoplasticity. We consider a general function

$$\mathcal{F}(\bar{\boldsymbol{\rho}}, \bar{\boldsymbol{\xi}}_1, \dots, \bar{\boldsymbol{\xi}}_{N^{\text{mat}}}; \mathbf{V}_1^{\bar{\mathbf{b}}^e}, \dots, \mathbf{V}_N^{\bar{\mathbf{b}}^e}; \mathbf{V}_1^{\bar{\boldsymbol{\beta}}}, \dots, \mathbf{V}_N^{\bar{\boldsymbol{\beta}}}; \mathbf{V}_1^{\alpha}, \dots, \mathbf{V}_N^{\alpha}; \mathbf{V}_1^{\hat{\boldsymbol{\gamma}}}, \dots, \mathbf{V}_N^{\hat{\boldsymbol{\gamma}}}; \mathbf{U}_1, \dots, \mathbf{U}_N)$$

and write out its Lagrangian expression as

$$\hat{\mathcal{F}} = \mathcal{F} + \sum_{n=1}^N \left(\boldsymbol{\lambda}_n^{\bar{\mathbf{b}}^e} \cdot \mathbf{R}_n^{\bar{\mathbf{b}}^e} + \boldsymbol{\lambda}_n^{\bar{\beta}} \cdot \mathbf{R}_n^{\bar{\beta}} + \boldsymbol{\lambda}_n^{\alpha} \cdot \mathbf{R}_n^{\alpha} + \boldsymbol{\lambda}_n^{\hat{\gamma}} \cdot \mathbf{R}_n^{\hat{\gamma}} + \boldsymbol{\lambda}_n^{\mathbf{u}} \cdot \mathbf{R}_n^{\mathbf{u}} \right) = \mathcal{F} + \sum_{n=1}^N \boldsymbol{\lambda}_n \cdot \mathbf{R}_n,$$

where we define

$$\boldsymbol{\lambda}_n = \left[\left(\boldsymbol{\lambda}_n^{\bar{\mathbf{b}}^e} \right)^\top, \left(\boldsymbol{\lambda}_n^{\bar{\beta}} \right)^\top, \left(\boldsymbol{\lambda}_n^{\alpha} \right)^\top, \left(\boldsymbol{\lambda}_n^{\hat{\gamma}} \right)^\top, \left(\boldsymbol{\lambda}_n^{\mathbf{u}} \right)^\top \right]^\top \quad \text{for } n = 1, \dots, N$$

and

$$\mathbf{R}_n = \left[\left(\mathbf{R}_n^{\bar{\mathbf{b}}^e} \right)^\top, \left(\mathbf{R}_n^{\bar{\beta}} \right)^\top, \left(\mathbf{R}_n^{\alpha} \right)^\top, \left(\mathbf{R}_n^{\hat{\gamma}} \right)^\top, \left(\mathbf{R}_n^{\mathbf{u}} \right)^\top \right]^\top \quad \text{for } n = 1, \dots, N.$$

The variables $\boldsymbol{\lambda}_n^{\bar{\mathbf{b}}^e}$, $\boldsymbol{\lambda}_n^{\bar{\beta}}$, $\boldsymbol{\lambda}_n^{\alpha}$, $\boldsymbol{\lambda}_n^{\hat{\gamma}}$, and $\boldsymbol{\lambda}_n^{\mathbf{u}}$ for $n = 1, \dots, N$ are the adjoint vectors that take arbitrary real values for now.

Taking the derivative of $\hat{\mathcal{F}}$ with respect to $\bar{\boldsymbol{\zeta}} \in \{\bar{\rho}, \bar{\boldsymbol{\xi}}_1, \dots, \bar{\boldsymbol{\xi}}_{N^{\text{mat}}}\}$ derives

$$\frac{d\hat{\mathcal{F}}}{d\bar{\boldsymbol{\zeta}}} = \frac{\partial \mathcal{F}}{\partial \bar{\boldsymbol{\zeta}}} + \sum_{n=1}^N \left(\frac{\partial \mathbf{V}_n}{\partial \bar{\boldsymbol{\zeta}}} \right)^\top \frac{\partial \mathcal{F}}{\partial \mathbf{V}_n} + \sum_{n=1}^N \left[\left(\frac{\partial \mathbf{R}_n}{\partial \bar{\boldsymbol{\zeta}}} \right)^\top + \left(\frac{\partial \mathbf{V}_{n-1}}{\partial \bar{\boldsymbol{\zeta}}} \right)^\top \left(\frac{\partial \mathbf{R}_n}{\partial \mathbf{V}_{n-1}} \right)^\top + \left(\frac{\partial \mathbf{V}_n}{\partial \bar{\boldsymbol{\zeta}}} \right)^\top \left(\frac{\partial \mathbf{R}_n}{\partial \mathbf{V}_n} \right)^\top \right] \boldsymbol{\lambda}_n.$$

Here we define

$$\mathbf{V}_n = \left[\left(\mathbf{V}_n^{\bar{\mathbf{b}}^e} \right)^\top, \left(\mathbf{V}_n^{\bar{\beta}} \right)^\top, \left(\mathbf{V}_n^{\alpha} \right)^\top, \left(\mathbf{V}_n^{\hat{\gamma}} \right)^\top, \left(\mathbf{U}_n \right)^\top \right]^\top \quad \text{for } n = 0, \dots, N,$$

and note that \mathbf{V}_0 represents the initial conditions.

Regrouping the terms in $d\hat{\mathcal{F}}/d\bar{\boldsymbol{\zeta}}$ renders

$$\begin{aligned} \frac{d\hat{\mathcal{F}}}{d\bar{\boldsymbol{\zeta}}} &= \frac{\partial \mathcal{F}}{\partial \bar{\boldsymbol{\zeta}}} + \sum_{n=1}^N \left(\frac{\partial \mathbf{R}_n}{\partial \bar{\boldsymbol{\zeta}}} \right)^\top \boldsymbol{\lambda}_n + \sum_{n=1}^{N-1} \left(\frac{\partial \mathbf{V}_n}{\partial \bar{\boldsymbol{\zeta}}} \right)^\top \left[\left(\frac{\partial \mathbf{R}_n}{\partial \mathbf{V}_n} \right)^\top \boldsymbol{\lambda}_n + \left(\frac{\partial \mathbf{R}_{n+1}}{\partial \mathbf{V}_n} \right)^\top \boldsymbol{\lambda}_{n+1} + \frac{\partial \mathcal{F}}{\partial \mathbf{V}_n} \right] \\ &\quad + \left(\frac{\partial \mathbf{V}_N}{\partial \bar{\boldsymbol{\zeta}}} \right)^\top \left[\left(\frac{\partial \mathbf{R}_N}{\partial \mathbf{V}_N} \right)^\top \boldsymbol{\lambda}_N + \frac{\partial \mathcal{F}}{\partial \mathbf{V}_N} \right], \end{aligned} \quad (\text{E.2})$$

where we use $\partial \mathbf{V}_0 / \partial \bar{\boldsymbol{\zeta}} = \mathbf{0}$. Note again that $\boldsymbol{\lambda}_1, \dots, \boldsymbol{\lambda}_N$ are arbitrary, and we select their values to eliminate computationally expensive term, $\partial \mathbf{V}_n / \partial \bar{\boldsymbol{\zeta}} = \mathbf{0}$ for $n = 1, \dots, N$. This step leads to the adjoint equations expressed as

$$\begin{cases} \left(\frac{\partial \mathbf{R}_n}{\partial \mathbf{V}_n} \right)^\top \boldsymbol{\lambda}_n + \left(\frac{\partial \mathbf{R}_{n+1}}{\partial \mathbf{V}_n} \right)^\top \boldsymbol{\lambda}_{n+1} = -\frac{\partial \mathcal{F}}{\partial \mathbf{V}_n} & \text{for } n = 1, \dots, N-1, \\ \left(\frac{\partial \mathbf{R}_N}{\partial \mathbf{V}_N} \right)^\top \boldsymbol{\lambda}_N = -\frac{\partial \mathcal{F}}{\partial \mathbf{V}_N}, \end{cases} \quad (\text{E.3})$$

where

$$\frac{\partial \mathbf{R}_n}{\partial \mathbf{V}_n} = \begin{bmatrix} \mathbf{I} & \mathbf{0} & \mathbf{0} & \frac{\partial \mathbf{R}_n^{\bar{\mathbf{b}}^e}}{\partial \mathbf{V}_n^{\hat{\gamma}}} & \frac{\partial \mathbf{R}_n^{\bar{\mathbf{b}}^e}}{\partial \mathbf{U}_n} \\ \mathbf{0} & \mathbf{I} & \mathbf{0} & \frac{\partial \mathbf{R}_n^{\bar{\beta}}}{\partial \mathbf{V}_n^{\hat{\gamma}}} & \frac{\partial \mathbf{R}_n^{\bar{\beta}}}{\partial \mathbf{U}_n} \\ \mathbf{0} & \mathbf{0} & \mathbf{I} & \frac{\partial \mathbf{R}_n^{\alpha}}{\partial \mathbf{V}_n^{\hat{\gamma}}} & \mathbf{0} \\ \mathbf{0} & \mathbf{0} & \mathbf{0} & \frac{\partial \mathbf{R}_n^{\hat{\gamma}}}{\partial \mathbf{V}_n^{\hat{\gamma}}} & \frac{\partial \mathbf{R}_n^{\hat{\gamma}}}{\partial \mathbf{U}_n} \\ \mathbf{0} & \mathbf{0} & \mathbf{0} & \frac{\partial \mathbf{R}_n^{\mathbf{u}}}{\partial \mathbf{V}_n^{\hat{\gamma}}} & \frac{\partial \mathbf{R}_n^{\mathbf{u}}}{\partial \mathbf{U}_n} \end{bmatrix} \quad \text{and} \quad \frac{\partial \mathbf{R}_{n+1}}{\partial \mathbf{V}_n} = \begin{bmatrix} \frac{\partial \mathbf{R}_{n+1}^{\bar{\mathbf{b}}^e}}{\partial \mathbf{V}_n^{\bar{\mathbf{b}}^e}} & \frac{\partial \mathbf{R}_{n+1}^{\bar{\mathbf{b}}^e}}{\partial \mathbf{V}_n^{\bar{\beta}}} & \mathbf{0} & \mathbf{0} & \frac{\partial \mathbf{R}_{n+1}^{\bar{\mathbf{b}}^e}}{\partial \mathbf{U}_n} \\ \frac{\partial \mathbf{R}_{n+1}^{\bar{\beta}}}{\partial \mathbf{V}_n^{\bar{\mathbf{b}}^e}} & \frac{\partial \mathbf{R}_{n+1}^{\bar{\beta}}}{\partial \mathbf{V}_n^{\bar{\beta}}} & \mathbf{0} & \mathbf{0} & \frac{\partial \mathbf{R}_{n+1}^{\bar{\beta}}}{\partial \mathbf{U}_n} \\ \mathbf{0} & \mathbf{0} & \frac{\partial \mathbf{R}_{n+1}^{\alpha}}{\partial \mathbf{V}_n^{\alpha}} & \mathbf{0} & \mathbf{0} \\ \frac{\partial \mathbf{R}_{n+1}^{\hat{\gamma}}}{\partial \mathbf{V}_n^{\bar{\mathbf{b}}^e}} & \frac{\partial \mathbf{R}_{n+1}^{\hat{\gamma}}}{\partial \mathbf{V}_n^{\bar{\beta}}} & \frac{\partial \mathbf{R}_{n+1}^{\hat{\gamma}}}{\partial \mathbf{V}_n^{\alpha}} & \mathbf{0} & \frac{\partial \mathbf{R}_{n+1}^{\hat{\gamma}}}{\partial \mathbf{U}_n} \\ \frac{\partial \mathbf{R}_{n+1}^{\mathbf{u}}}{\partial \mathbf{V}_n^{\bar{\mathbf{b}}^e}} & \frac{\partial \mathbf{R}_{n+1}^{\mathbf{u}}}{\partial \mathbf{V}_n^{\bar{\beta}}} & \mathbf{0} & \mathbf{0} & \frac{\partial \mathbf{R}_{n+1}^{\mathbf{u}}}{\partial \mathbf{U}_n} \end{bmatrix}.$$

Based on (E.3), we compute the adjoint variables $(\boldsymbol{\lambda}_n^{\bar{\mathbf{b}}^e}, \boldsymbol{\lambda}_n^{\bar{\boldsymbol{\beta}}}, \boldsymbol{\lambda}_n^\alpha, \boldsymbol{\lambda}_n^{\hat{\boldsymbol{\gamma}}},$ and $\boldsymbol{\lambda}_n^{\mathbf{u}}$ for $n = 1, \dots, N)$ in a reversed order as follows. At load step N , we directly write out $\boldsymbol{\lambda}_N^{\bar{\mathbf{b}}^e}, \boldsymbol{\lambda}_N^{\bar{\boldsymbol{\beta}}},$ and $\boldsymbol{\lambda}_N^\alpha$ as

$$\boldsymbol{\lambda}_N^{\bar{\mathbf{b}}^e} = -\frac{\partial \mathcal{F}}{\partial \mathbf{V}_N^{\bar{\mathbf{b}}^e}}, \quad \boldsymbol{\lambda}_N^{\bar{\boldsymbol{\beta}}} = -\frac{\partial \mathcal{F}}{\partial \mathbf{V}_N^{\bar{\boldsymbol{\beta}}}}, \quad \text{and} \quad \boldsymbol{\lambda}_N^\alpha = -\frac{\partial \mathcal{F}}{\partial \mathbf{V}_N^\alpha}.$$

We then solve for $\boldsymbol{\lambda}_N^{\hat{\boldsymbol{\gamma}}}$ and $\boldsymbol{\lambda}_N^{\mathbf{u}}$ from

$$\begin{bmatrix} \left(\frac{\partial \mathbf{R}_N^{\hat{\boldsymbol{\gamma}}}}{\partial \mathbf{V}_N^{\hat{\boldsymbol{\gamma}}}} \right)^\top & \left(\frac{\partial \mathbf{R}_N^{\mathbf{u}}}{\partial \mathbf{V}_N^{\hat{\boldsymbol{\gamma}}}} \right)^\top \\ \left(\frac{\partial \mathbf{R}_N^{\hat{\boldsymbol{\gamma}}}}{\partial \mathbf{U}_N} \right)^\top & \left(\frac{\partial \mathbf{R}_N^{\mathbf{u}}}{\partial \mathbf{U}_N} \right)^\top \end{bmatrix} \begin{bmatrix} \boldsymbol{\lambda}_N^{\hat{\boldsymbol{\gamma}}} \\ \boldsymbol{\lambda}_N^{\mathbf{u}} \end{bmatrix} = - \begin{bmatrix} \frac{\partial \mathcal{F}}{\partial \mathbf{V}_N^{\hat{\boldsymbol{\gamma}}}} + \left(\frac{\partial \mathbf{R}_N^{\bar{\mathbf{b}}^e}}{\partial \mathbf{V}_N^{\hat{\boldsymbol{\gamma}}}} \right)^\top \boldsymbol{\lambda}_N^{\bar{\mathbf{b}}^e} + \left(\frac{\partial \mathbf{R}_N^{\bar{\boldsymbol{\beta}}}}{\partial \mathbf{V}_N^{\hat{\boldsymbol{\gamma}}}} \right)^\top \boldsymbol{\lambda}_N^{\bar{\boldsymbol{\beta}}} + \left(\frac{\partial \mathbf{R}_N^\alpha}{\partial \mathbf{V}_N^{\hat{\boldsymbol{\gamma}}}} \right)^\top \boldsymbol{\lambda}_N^\alpha \\ \frac{\partial \mathcal{F}}{\partial \mathbf{U}_N} + \left(\frac{\partial \mathbf{R}_N^{\bar{\mathbf{b}}^e}}{\partial \mathbf{U}_N} \right)^\top \boldsymbol{\lambda}_N^{\bar{\mathbf{b}}^e} + \left(\frac{\partial \mathbf{R}_N^{\bar{\boldsymbol{\beta}}}}{\partial \mathbf{U}_N} \right)^\top \boldsymbol{\lambda}_N^{\bar{\boldsymbol{\beta}}} \end{bmatrix}. \quad (\text{E.4})$$

At the remaining load steps, $n = N - 1, \dots, 1$, we write out $\boldsymbol{\lambda}_n^{\bar{\mathbf{b}}^e}, \boldsymbol{\lambda}_n^{\bar{\boldsymbol{\beta}}},$ and $\boldsymbol{\lambda}_n^\alpha$ as

$$\begin{cases} \boldsymbol{\lambda}_n^{\bar{\mathbf{b}}^e} = - \left[\frac{\partial \mathcal{F}}{\partial \mathbf{V}_n^{\bar{\mathbf{b}}^e}} + \left(\frac{\partial \mathbf{R}_{n+1}^{\bar{\mathbf{b}}^e}}{\partial \mathbf{V}_n^{\bar{\mathbf{b}}^e}} \right)^\top \boldsymbol{\lambda}_{n+1}^{\bar{\mathbf{b}}^e} + \left(\frac{\partial \mathbf{R}_{n+1}^{\bar{\boldsymbol{\beta}}}}{\partial \mathbf{V}_n^{\bar{\mathbf{b}}^e}} \right)^\top \boldsymbol{\lambda}_{n+1}^{\bar{\boldsymbol{\beta}}} + \left(\frac{\partial \mathbf{R}_{n+1}^{\hat{\boldsymbol{\gamma}}}}{\partial \mathbf{V}_n^{\bar{\mathbf{b}}^e}} \right)^\top \boldsymbol{\lambda}_{n+1}^{\hat{\boldsymbol{\gamma}}} + \left(\frac{\partial \mathbf{R}_{n+1}^{\mathbf{u}}}{\partial \mathbf{V}_n^{\bar{\mathbf{b}}^e}} \right)^\top \boldsymbol{\lambda}_{n+1}^{\mathbf{u}} \right], \\ \boldsymbol{\lambda}_n^{\bar{\boldsymbol{\beta}}} = - \left[\frac{\partial \mathcal{F}}{\partial \mathbf{V}_n^{\bar{\boldsymbol{\beta}}}} + \left(\frac{\partial \mathbf{R}_{n+1}^{\bar{\mathbf{b}}^e}}{\partial \mathbf{V}_n^{\bar{\boldsymbol{\beta}}}} \right)^\top \boldsymbol{\lambda}_{n+1}^{\bar{\mathbf{b}}^e} + \left(\frac{\partial \mathbf{R}_{n+1}^{\bar{\boldsymbol{\beta}}}}{\partial \mathbf{V}_n^{\bar{\boldsymbol{\beta}}}} \right)^\top \boldsymbol{\lambda}_{n+1}^{\bar{\boldsymbol{\beta}}} + \left(\frac{\partial \mathbf{R}_{n+1}^{\hat{\boldsymbol{\gamma}}}}{\partial \mathbf{V}_n^{\bar{\boldsymbol{\beta}}}} \right)^\top \boldsymbol{\lambda}_{n+1}^{\hat{\boldsymbol{\gamma}}} + \left(\frac{\partial \mathbf{R}_{n+1}^{\mathbf{u}}}{\partial \mathbf{V}_n^{\bar{\boldsymbol{\beta}}}} \right)^\top \boldsymbol{\lambda}_{n+1}^{\mathbf{u}} \right], \\ \boldsymbol{\lambda}_n^\alpha = - \left[\frac{\partial \mathcal{F}}{\partial \mathbf{V}_n^\alpha} + \left(\frac{\partial \mathbf{R}_{n+1}^\alpha}{\partial \mathbf{V}_n^\alpha} \right)^\top \boldsymbol{\lambda}_{n+1}^\alpha + \left(\frac{\partial \mathbf{R}_{n+1}^{\hat{\boldsymbol{\gamma}}}}{\partial \mathbf{V}_n^\alpha} \right)^\top \boldsymbol{\lambda}_{n+1}^{\hat{\boldsymbol{\gamma}}} \right], \end{cases}$$

and then solve for $\boldsymbol{\lambda}_n^{\hat{\boldsymbol{\gamma}}}$ and $\boldsymbol{\lambda}_n^{\mathbf{u}}$ from

$$\begin{bmatrix} \left(\frac{\partial \mathbf{R}_n^{\hat{\boldsymbol{\gamma}}}}{\partial \mathbf{V}_n^{\hat{\boldsymbol{\gamma}}}} \right)^\top & \left(\frac{\partial \mathbf{R}_n^{\mathbf{u}}}{\partial \mathbf{V}_n^{\hat{\boldsymbol{\gamma}}}} \right)^\top \\ \left(\frac{\partial \mathbf{R}_n^{\hat{\boldsymbol{\gamma}}}}{\partial \mathbf{U}_n} \right)^\top & \left(\frac{\partial \mathbf{R}_n^{\mathbf{u}}}{\partial \mathbf{U}_n} \right)^\top \end{bmatrix} \begin{bmatrix} \boldsymbol{\lambda}_n^{\hat{\boldsymbol{\gamma}}} \\ \boldsymbol{\lambda}_n^{\mathbf{u}} \end{bmatrix} = - \begin{bmatrix} \frac{\partial \mathcal{F}}{\partial \mathbf{V}_n^{\hat{\boldsymbol{\gamma}}}} + \left(\frac{\partial \mathbf{R}_n^{\bar{\mathbf{b}}^e}}{\partial \mathbf{V}_n^{\hat{\boldsymbol{\gamma}}}} \right)^\top \boldsymbol{\lambda}_n^{\bar{\mathbf{b}}^e} + \left(\frac{\partial \mathbf{R}_n^{\bar{\boldsymbol{\beta}}}}{\partial \mathbf{V}_n^{\hat{\boldsymbol{\gamma}}}} \right)^\top \boldsymbol{\lambda}_n^{\bar{\boldsymbol{\beta}}} + \left(\frac{\partial \mathbf{R}_n^\alpha}{\partial \mathbf{V}_n^{\hat{\boldsymbol{\gamma}}}} \right)^\top \boldsymbol{\lambda}_n^\alpha \\ \frac{\partial \mathcal{F}}{\partial \mathbf{U}_n} + \frac{\partial \check{\mathcal{F}}}{\partial \mathbf{U}_n} + \left(\frac{\partial \mathbf{R}_n^{\bar{\mathbf{b}}^e}}{\partial \mathbf{U}_n} \right)^\top \boldsymbol{\lambda}_n^{\bar{\mathbf{b}}^e} + \left(\frac{\partial \mathbf{R}_n^{\bar{\boldsymbol{\beta}}}}{\partial \mathbf{U}_n} \right)^\top \boldsymbol{\lambda}_n^{\bar{\boldsymbol{\beta}}} \end{bmatrix} \quad (\text{E.5})$$

where

$$\frac{\partial \check{\mathcal{F}}}{\partial \mathbf{U}_n} := \left(\frac{\partial \mathbf{R}_{n+1}^{\bar{\mathbf{b}}^e}}{\partial \mathbf{U}_n} \right)^\top \boldsymbol{\lambda}_{n+1}^{\bar{\mathbf{b}}^e} + \left(\frac{\partial \mathbf{R}_{n+1}^{\bar{\boldsymbol{\beta}}}}{\partial \mathbf{U}_n} \right)^\top \boldsymbol{\lambda}_{n+1}^{\bar{\boldsymbol{\beta}}} + \left(\frac{\partial \mathbf{R}_{n+1}^{\hat{\boldsymbol{\gamma}}}}{\partial \mathbf{U}_n} \right)^\top \boldsymbol{\lambda}_{n+1}^{\hat{\boldsymbol{\gamma}}} + \left(\frac{\partial \mathbf{R}_{n+1}^{\mathbf{u}}}{\partial \mathbf{U}_n} \right)^\top \boldsymbol{\lambda}_{n+1}^{\mathbf{u}}.$$

After solving for the adjoint variables, we substitute them into (E.2) and derive the sensitivity expression as

$$\frac{d\mathcal{F}}{d\bar{\boldsymbol{\zeta}}} = \frac{\partial \mathcal{F}}{\partial \bar{\boldsymbol{\zeta}}} + \sum_{n=1}^N \left[\left(\frac{\partial \mathbf{R}_n^{\bar{\mathbf{b}}^e}}{\partial \bar{\boldsymbol{\zeta}}} \right)^\top \boldsymbol{\lambda}_n^{\bar{\mathbf{b}}^e} + \left(\frac{\partial \mathbf{R}_n^{\bar{\boldsymbol{\beta}}}}{\partial \bar{\boldsymbol{\zeta}}} \right)^\top \boldsymbol{\lambda}_n^{\bar{\boldsymbol{\beta}}} + \left(\frac{\partial \mathbf{R}_n^{\hat{\boldsymbol{\gamma}}}}{\partial \bar{\boldsymbol{\zeta}}} \right)^\top \boldsymbol{\lambda}_n^{\hat{\boldsymbol{\gamma}}} + \left(\frac{\partial \mathbf{R}_n^{\mathbf{u}}}{\partial \bar{\boldsymbol{\zeta}}} \right)^\top \boldsymbol{\lambda}_n^{\mathbf{u}} \right],$$

where we use $\partial \mathbf{R}_n^\alpha / \partial \bar{\boldsymbol{\zeta}} = \mathbf{0}$ and $d\mathcal{F}/d\bar{\boldsymbol{\zeta}} = d\hat{\mathcal{F}}/d\bar{\boldsymbol{\zeta}}$ by noticing

$$\boldsymbol{\lambda}_n^{\bar{\mathbf{b}}^e} \cdot \mathbf{R}_n^{\bar{\mathbf{b}}^e} = \boldsymbol{\lambda}_n^{\bar{\boldsymbol{\beta}}} \cdot \mathbf{R}_n^{\bar{\boldsymbol{\beta}}} = \boldsymbol{\lambda}_n^\alpha \cdot \mathbf{R}_n^\alpha = \boldsymbol{\lambda}_n^{\hat{\boldsymbol{\gamma}}} \cdot \mathbf{R}_n^{\hat{\boldsymbol{\gamma}}} = \boldsymbol{\lambda}_n^{\mathbf{u}} \cdot \mathbf{R}_n^{\mathbf{u}} = 0. \quad (\text{E.6})$$

We remark that, by using the modern computer method of automatic differentiation, one can effortlessly compute all the above partial derivatives without deriving their explicit (and typically complex) expressions.

Appendix E.3. Sensitivity verification

In this subsection, we verify the accuracy of the sensitivity analysis described in Appendix E.2 by comparing it against the forward finite difference method. Using the finite difference scheme, the sensitivity of any function \mathcal{F} with respect to the physical design variable $\bar{\zeta}_e$ of element e for $\bar{\zeta} \in \{\bar{\rho}, \bar{\xi}_1, \dots, \bar{\xi}_{N\epsilon}\}$ is computed as

$$\frac{d\mathcal{F}}{d\bar{\zeta}_e} = \frac{\mathcal{F}(\bar{\zeta}_e + \varepsilon) - \mathcal{F}(\bar{\zeta}_e)}{\varepsilon}$$

where $\varepsilon \in [10^{-6}, 10^{-4}]$ is a small perturbation parameter.

According to this formula, we compare the sensitivities of all objective functions (J_{stiff} , J_{force} , and J_{energy}) and constraint functions (g_{V0} , g_{V1} , g_{V2} , g_{V3} , g_{V4} , g_P , g_M , and g_C) employed in Section 4. For representativeness, the comparisons are focused on the most complex cases: J_{energy} for the optimized damper in Fig. 6; J_{stiff} and g_{V0} for Dsg. 4 in Fig. 7; g_{V1} , g_{V2} , g_{V3} , and g_{V4} for the optimized bumper in Fig. 10; and J_{force} , g_P , g_M , and g_C for Dsg. 4 in Fig. 12.

To perform the comparison, we use stratified sampling of all design variables and present the results in Fig. E.15. The proposed sensitivity analysis in Appendix E.2 shows good agreement with the finite difference scheme. The observed absolute errors (e_{abs}) are in the range of $[10^{-11}, 10^{-6}]$, while the relative errors (e_{rel}) are in the range of $[10^{-8}, 10^{-4}]$. This verification demonstrates the reliability of the proposed sensitivity analysis, irrespective of the complexity introduced by the history dependence of finite strain elastoplasticity.

Appendix F. Comparisons among various mesh and element combinations

In this section, we compare the elastoplastic responses of structures defined with various meshes and elements. The proposed topology optimization framework favors a voxel-based mesh, where the grid in the undeformed configurations of structures is fixed during optimization, and solid and void elements coexist. However, for practical manufacturing purposes, a body-fitted mesh is more suitable for generating printable files (e.g., the STereoLithography format), as the mesh boundaries closely align with structural geometries and only contain solid elements.

To evaluate the accuracy loss when converting optimized designs from voxel-based to body-fitted meshes, we take Dsg. 5 in Fig. 7 as an example and compare the elastoplastic responses in Fig. F.16 and Table F.3. The results show that, compared to the design defined on a voxel-based mesh with quadrilateral elements, the structure defined on the body-fitted mesh with the same elements exhibits negligible relative errors: 4.59% in initial stiffness, 1.20% in end force, and 0.84% in total energy. These results justify the use of voxel-based meshes in the proposed framework.

Table F.3: Comparisons of the performance metrics among various meshes and elements

| Meshes | Elements | Usage | Initial stiffness (N/mm) | End force (N) | Total energy (N·mm) |
|---------------------------|---------------|-----------------------|-----------------------------|------------------|------------------------|
| Voxel-based, structured | Quadrilateral | Topology optimization | 10.25 | 10.03 | 14.31 |
| Body-fitted, unstructured | Quadrilateral | Manufacturing | 10.72 (4.59%) | 10.15 (1.20%) | 14.43 (0.84%) |
| Voxel-based, structured | Triangular | Checking stiffening | 9.88 (-3.61%) | 9.26 (-7.68%) | 13.39 (-6.43%) |

In the context of finite strain elastoplasticity, we also need to examine the element types, as certain mesh and element combinations may exhibit over-stiffening behaviors in structures (Sloan and Randolph, 1982; Wells et al., 2002) due to the isochoric plastic flow, despite the limited compressibility from elasticity. To mitigate these over-stiffening behaviors, higher-order and crossed linear triangular elements (Wells et al., 2002) have been identified as simple and effective strategies. However, both strategies are computationally expensive.

In this study, we opt for first-order quadrilateral and hexahedral elements to reduce computational time. As shown in Fig. F.16 and Table F.3, the performance metrics of the current setup remain close to the “golden setup” of crossed linear triangular elements for plasticity (Wells et al., 2002), with relative errors

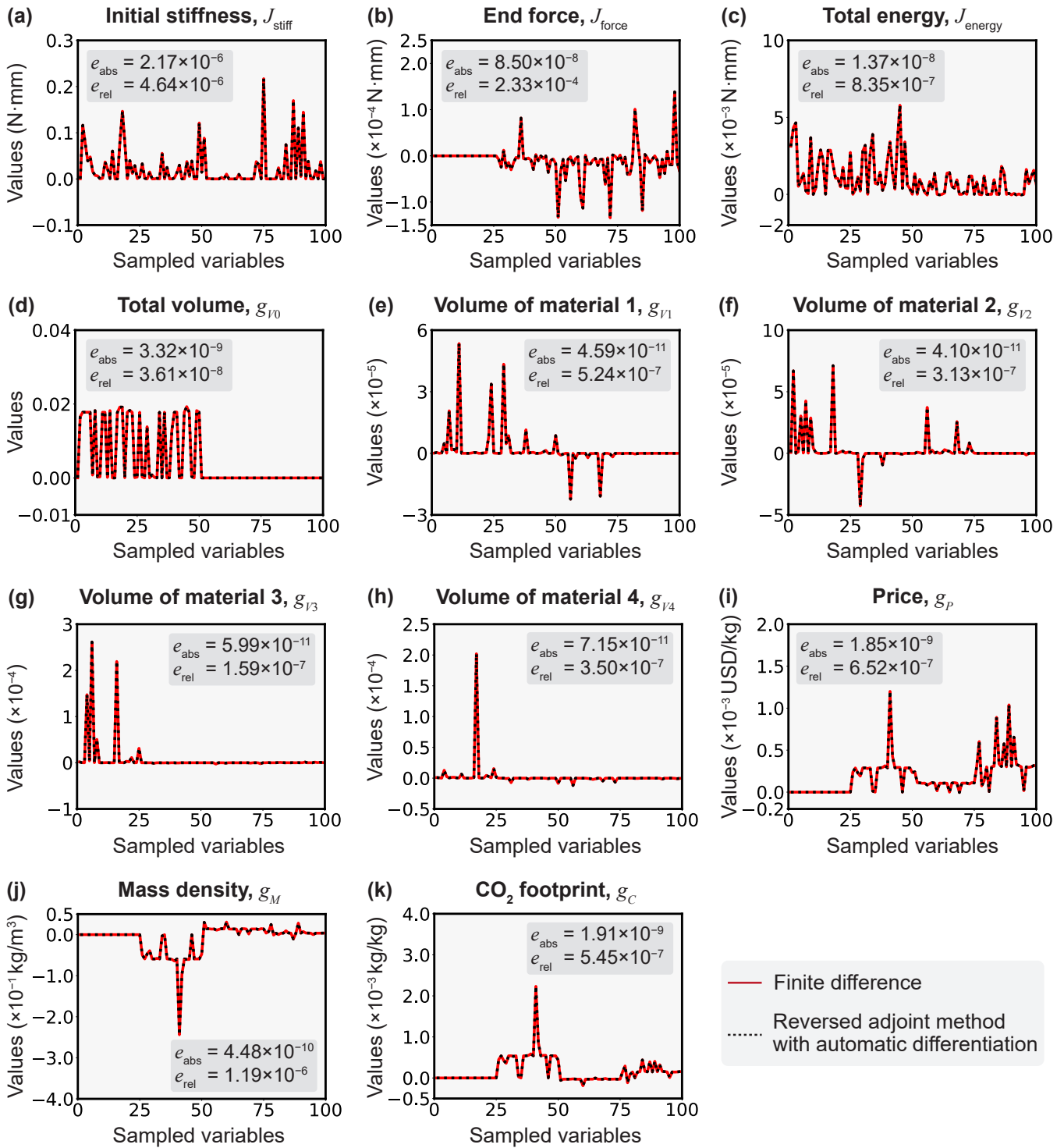


Figure E.15: Sensitivity verification for various functions used in Section 4. (a) Initial energy of Dsg. 4 in Fig. 7. (b) End compliance of Dsg. 4 in Fig. 12. (c) Total energy of the optimized damper in Fig. 6. (d) Total material volume of Dsg. 4 in Fig. 7. (e)–(h) Volumes of materials 1–4 of the optimized bumper in Fig. 10. (i)–(k) Price, mass density, and CO₂ footprint of Dsg. 4 in Fig. 12.

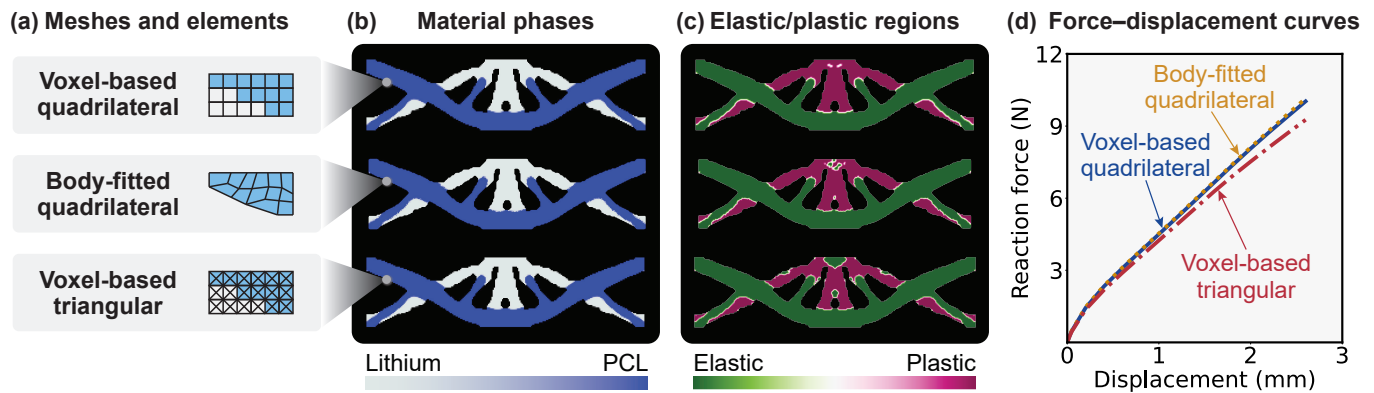


Figure F.16: Comparisons among various meshes and elements. (a) Compared meshes and the associated finite elements. (b) Material phases. (c) Elastic/plastic regions. (d) Force–displacement (F – u) curves.

below 10%. Additionally, we emphasize that the proposed design framework is independent of mesh and element types, especially with the versatile implementation of FEniTop (Jia et al., 2024d). Users have the flexibility to balance solution accuracy and computational cost based on their specific requirements.

References

- Abueidda, D.W., Kang, Z., Koric, S., James, K.A., Jasiuk, I.M., 2021. Topology optimization for three-dimensional elastoplastic architected materials using a path-dependent adjoint method. *International Journal for Numerical Methods in Engineering* 122, 1889–1910. doi:[10.1002/nme.6604](https://doi.org/10.1002/nme.6604).
- Alberdi, R., Khandelwal, K., 2017. Topology optimization of pressure dependent elastoplastic energy absorbing structures with material damage constraints. *Finite Elements in Analysis and Design* 133, 42–61. doi:[10.1016/j.finel.2017.05.004](https://doi.org/10.1016/j.finel.2017.05.004).
- Alberdi, R., Khandelwal, K., 2019a. Bi-material topology optimization for energy dissipation with inertia and material rate effects under finite deformations. *Finite Elements in Analysis and Design* 164, 18–41. doi:[10.1016/j.finel.2019.06.003](https://doi.org/10.1016/j.finel.2019.06.003).
- Alberdi, R., Khandelwal, K., 2019b. Design of periodic elastoplastic energy dissipating microstructures. *Structural and Multidisciplinary Optimization* 59, 461–483. doi:[10.1007/s00158-018-2076-2](https://doi.org/10.1007/s00158-018-2076-2).
- Alberdi, R., Zhang, G., Li, L., Khandelwal, K., 2018. A unified framework for nonlinear path-dependent sensitivity analysis in topology optimization. *International Journal for Numerical Methods in Engineering* 115, 1–56. doi:[10.1002/nme.5794](https://doi.org/10.1002/nme.5794).
- Amir, O., 2017. Stress-constrained continuum topology optimization: A new approach based on elasto-plasticity. *Structural and Multidisciplinary Optimization* 55, 1797–1818. doi:[10.1007/s00158-016-1618-8](https://doi.org/10.1007/s00158-016-1618-8).
- Bendsøe, M.P., Kikuchi, N., 1988. Generating optimal topologies in structural design using a homogenization method. *Computer Methods in Applied Mechanics and Engineering* 71, 197–224. doi:[10.1016/0045-7825\(88\)90086-2](https://doi.org/10.1016/0045-7825(88)90086-2).
- Bendsoe, M.P., Sigmund, O., 2003. *Topology Optimization: Theory, Methods, and Applications*. Springer Science & Business Media.
- Boissier, M., Deaton, J.D., Beran, P.A., Vermaak, N., 2021. Elastoplastic topology optimization of cyclically loaded structures via direct methods for shakedown. *Structural and Multidisciplinary Optimization* 64, 189–217. doi:[10.1007/s00158-021-02875-6](https://doi.org/10.1007/s00158-021-02875-6).

- Bourdin, B., 2001. Filters in topology optimization. *International Journal for Numerical Methods in Engineering* 50, 2143–2158. doi:[10.1002/nme.116](https://doi.org/10.1002/nme.116).
- Chaboche, J.L., 2008. A review of some plasticity and viscoplasticity constitutive theories. *International Journal of Plasticity* 24, 1642–1693. doi:[10.1016/j.ijplas.2008.03.009](https://doi.org/10.1016/j.ijplas.2008.03.009).
- Cvitanić, V., Vlak, F., Lozina, Ž., 2008. A finite element formulation based on non-associated plasticity for sheet metal forming. *International Journal of Plasticity* 24, 646–687. doi:[10.1016/j.ijplas.2007.07.003](https://doi.org/10.1016/j.ijplas.2007.07.003).
- Desai, J., Allaire, G., Jouve, F., Mang, C., 2021. Topology optimization in quasi-static plasticity with hardening using a level-set method. *Structural and Multidisciplinary Optimization* 64, 3163–3191. doi:[10.1007/s00158-021-03034-7](https://doi.org/10.1007/s00158-021-03034-7).
- Gearing, B.P., Moon, H.S., Anand, L., 2001. A plasticity model for interface friction: Application to sheet metal forming. *International Journal of Plasticity* 17, 237–271. doi:[10.1016/S0749-6419\(00\)00034-6](https://doi.org/10.1016/S0749-6419(00)00034-6).
- Han, J., Furuta, K., Kondoh, T., Nishiwaki, S., Terada, K., 2024. Topology optimization of finite strain elastoplastic materials using continuous adjoint method: Formulation, implementation, and applications. *Computer Methods in Applied Mechanics and Engineering* 429, 117181. doi:[10.1016/j.cma.2024.117181](https://doi.org/10.1016/j.cma.2024.117181).
- Ivarsson, N., Wallin, M., Amir, O., Tortorelli, D.A., 2021. Plastic work constrained elastoplastic topology optimization. *International Journal for Numerical Methods in Engineering* 122, 4354–4377. doi:[10.1002/nme.6706](https://doi.org/10.1002/nme.6706).
- Ivarsson, N., Wallin, M., Tortorelli, D., 2018. Topology optimization of finite strain viscoplastic systems under transient loads. *International Journal for Numerical Methods in Engineering* 114, 1351–1367. doi:[10.1002/nme.5789](https://doi.org/10.1002/nme.5789).
- Ivarsson, N., Wallin, M., Tortorelli, D.A., 2020. Topology optimization for designing periodic microstructures based on finite strain viscoplasticity. *Structural and Multidisciplinary Optimization* 61, 2501–2521. doi:[10.1007/s00158-020-02555-x](https://doi.org/10.1007/s00158-020-02555-x).
- Jia, Y., Li, L., Wang, C., Lu, Z., Zhang, R., 2019. A novel shape memory alloy damping inerter for vibration mitigation. *Smart Materials and Structures* 28, 115002. doi:[10.1088/1361-665X/ab3dc8](https://doi.org/10.1088/1361-665X/ab3dc8).
- Jia, Y., Li, W., Zhang, X.S., 2025. Multimaterial topology optimization of elastoplastic composite structures. *Journal of the Mechanics and Physics of Solids* 196, 106018. doi:[10.1016/j.jmps.2024.106018](https://doi.org/10.1016/j.jmps.2024.106018).
- Jia, Y., Liu, K., Zhang, X.S., 2024a. Modulate stress distribution with bio-inspired irregular architected materials towards optimal tissue support. *Nature Communications* 15, 4072. doi:[10.1038/s41467-024-47831-2](https://doi.org/10.1038/s41467-024-47831-2).
- Jia, Y., Liu, K., Zhang, X.S., 2024b. Topology optimization of irregular multiscale structures with tunable responses using a virtual growth rule. *Computer Methods in Applied Mechanics and Engineering* 425, 116864. doi:[10.1016/j.cma.2024.116864](https://doi.org/10.1016/j.cma.2024.116864).
- Jia, Y., Liu, K., Zhang, X.S., 2024c. Unstructured growth of irregular architectures for optimized metastructures. *Journal of the Mechanics and Physics of Solids* 192, 105787. doi:[10.1016/j.jmps.2024.105787](https://doi.org/10.1016/j.jmps.2024.105787).
- Jia, Y., Lopez-Pamies, O., Zhang, X.S., 2023. Controlling the fracture response of structures via topology optimization: From delaying fracture nucleation to maximizing toughness. *Journal of the Mechanics and Physics of Solids* 173, 105227. doi:[10.1016/j.jmps.2023.105227](https://doi.org/10.1016/j.jmps.2023.105227).

- Jia, Y., Wang, C., Zhang, X.S., 2024d. FEniTop: A simple FEniCSx implementation for 2D and 3D topology optimization supporting parallel computing. *Structural and Multidisciplinary Optimization* 67, 140. doi:[10.1007/s00158-024-03818-7](https://doi.org/10.1007/s00158-024-03818-7).
- Jia, Y.Q., Wang, C., Li, L.Z., Zhang, R.F., Lu, Z.D., 2022. Residual seismic performance of fire-damaged reinforced concrete frame structure with metallic yielding dampers. *Journal of Structural Engineering* 148, 04022003. doi:[10.1061/\(ASCE\)ST.1943-541X.0003284](https://doi.org/10.1061/(ASCE)ST.1943-541X.0003284).
- Jia, Y.Q., Wang, C., Zhang, R.F., Li, L.Z., Lu, Z.D., 2021. A double shape memory alloy damper for structural vibration control. *International Journal of Structural Stability and Dynamics* 21, 2150098. doi:[10.1142/S021945542150098X](https://doi.org/10.1142/S021945542150098X).
- Kim, S., Yun, G.J., 2020. Microstructure topology optimization by targeting prescribed nonlinear stress-strain relationships. *International Journal of Plasticity* 128, 102684. doi:[10.1016/j.ijplas.2020.102684](https://doi.org/10.1016/j.ijplas.2020.102684).
- Krieg, R.D., Krieg, D.B., 1977. Accuracies of Numerical Solution Methods for the Elastic-Perfectly Plastic Model. *Journal of Pressure Vessel Technology* 99, 510–515. doi:[10.1115/1.3454568](https://doi.org/10.1115/1.3454568).
- Kumar, A., Lopez-Pamies, O., 2020. The phase-field approach to self-healable fracture of elastomers: A model accounting for fracture nucleation at large, with application to a class of conspicuous experiments. *Theoretical and Applied Fracture Mechanics* 107, 102550. doi:[10.1016/j.tafmec.2020.102550](https://doi.org/10.1016/j.tafmec.2020.102550).
- Kundu, R.D., Zhang, X.S., 2025. Sustainability-oriented multimaterial topology optimization: designing efficient structures incorporating environmental effects. *Structural and Multidisciplinary Optimization* 68, 1–20.
- Li, L., Khandelwal, K., 2017. Design of fracture resistant energy absorbing structures using elastoplastic topology optimization. *Structural and Multidisciplinary Optimization* 56, 1447–1475. doi:[10.1007/s00158-017-1735-z](https://doi.org/10.1007/s00158-017-1735-z).
- Li, L., Zhang, G., Khandelwal, K., 2017a. Design of energy dissipating elastoplastic structures under cyclic loads using topology optimization. *Structural and Multidisciplinary Optimization* 56, 391–412. doi:[10.1007/s00158-017-1671-y](https://doi.org/10.1007/s00158-017-1671-y).
- Li, L., Zhang, G., Khandelwal, K., 2017b. Topology optimization of energy absorbing structures with maximum damage constraint. *International Journal for Numerical Methods in Engineering* 112, 737–775. doi:[10.1002/nme.5531](https://doi.org/10.1002/nme.5531).
- Li, M., Deng, Y., Zhang, H., Wong, S.H.F., Mohamed, A., Zheng, Y., Gao, J., Yuen, T.Y.P., Dong, B., Kuang, J.S., 2021. Topology optimization of multi-material structures with elastoplastic strain hardening model. *Structural and Multidisciplinary Optimization* 64, 1141–1160. doi:[10.1007/s00158-021-02905-3](https://doi.org/10.1007/s00158-021-02905-3).
- Li, W., Jia, Y., Wang, F., Sigmund, O., Zhang, X.S., 2023. Programming and physical realization of extreme three-dimensional responses of metastructures under large deformations. *International Journal of Engineering Science* 191, 103881. doi:[10.1016/j.ijengsci.2023.103881](https://doi.org/10.1016/j.ijengsci.2023.103881).
- Li, X., Zhang, X., Zhang, Y., 2024. Three-dimensional plasticity-based topology optimization with smoothed finite element analysis. *Computational Mechanics* 73, 533–548. doi:[10.1007/s00466-023-02378-9](https://doi.org/10.1007/s00466-023-02378-9).
- Maute, K., Schwarz, S., Ramm, E., 1998. Adaptive topology optimization of elastoplastic structures. *Structural optimization* 15, 81–91. doi:[10.1007/BF01278493](https://doi.org/10.1007/BF01278493).
- Miehe, C., 1996. Exponential map algorithm for stress updates in anisotropic multiplicative elastoplasticity for single crystals. *International Journal for Numerical Methods in Engineering* 39, 3367–3390. doi:[10.1002/\(SICI\)1097-0207\(19961015\)39:19<3367::AID-NME4>3.0.CO;2-7](https://doi.org/10.1002/(SICI)1097-0207(19961015)39:19<3367::AID-NME4>3.0.CO;2-7).

- Nakshatrala, P.B., Tortorelli, D.A., 2015. Topology optimization for effective energy propagation in rate-independent elastoplastic material systems. *Computer Methods in Applied Mechanics and Engineering* 295, 305–326. doi:[10.1016/j.cma.2015.05.004](https://doi.org/10.1016/j.cma.2015.05.004).
- Patel, N.M., Kang, B.S., Renaud, J.E., Tovar, A., 2009. Crashworthiness Design Using Topology Optimization. *Journal of Mechanical Design* 131, 061013. doi:[10.1115/1.3116256](https://doi.org/10.1115/1.3116256).
- Ren, C., Min, H., Ma, T., Wang, F., 2020. An effective topology optimization method for crashworthiness of thin-walled structures using the equivalent linear static loads. *Proceedings of the Institution of Mechanical Engineers, Part D: Journal of Automobile Engineering* 234, 3239–3255. doi:[10.1177/0954407020940138](https://doi.org/10.1177/0954407020940138).
- Simo, J.C., 1988a. A framework for finite strain elastoplasticity based on maximum plastic dissipation and the multiplicative decomposition: Part I. Continuum formulation. *Computer Methods in Applied Mechanics and Engineering* 66, 199–219. doi:[10.1016/0045-7825\(88\)90076-X](https://doi.org/10.1016/0045-7825(88)90076-X).
- Simo, J.C., 1988b. A framework for finite strain elastoplasticity based on maximum plastic dissipation and the multiplicative decomposition. Part II: Computational aspects. *Computer Methods in Applied Mechanics and Engineering* 68, 1–31. doi:[10.1016/0045-7825\(88\)90104-1](https://doi.org/10.1016/0045-7825(88)90104-1).
- Simo, J.C., 1992. Algorithms for static and dynamic multiplicative plasticity that preserve the classical return mapping schemes of the infinitesimal theory. *Computer Methods in Applied Mechanics and Engineering* 99, 61–112. doi:[10.1016/0045-7825\(92\)90123-2](https://doi.org/10.1016/0045-7825(92)90123-2).
- Simo, J.C., Hughes, T.J., 2006. *Computational Inelasticity*. volume 7. Springer Science & Business Media.
- Simo, J.C., Miehe, C., 1992. Associative coupled thermoplasticity at finite strains: Formulation, numerical analysis and implementation. *Computer Methods in Applied Mechanics and Engineering* 98, 41–104. doi:[10.1016/0045-7825\(92\)90170-0](https://doi.org/10.1016/0045-7825(92)90170-0).
- Sloan, S.W., Randolph, M.F., 1982. Numerical prediction of collapse loads using finite element methods. *International Journal for Numerical and Analytical Methods in Geomechanics* 6, 47–76. doi:[10.1002/nag.1610060105](https://doi.org/10.1002/nag.1610060105).
- Sun, G., Tian, J., Liu, T., Yan, X., Huang, X., 2018. Crashworthiness optimization of automotive parts with tailor rolled blank. *Engineering Structures* 169, 201–215. doi:[10.1016/j.engstruct.2018.05.050](https://doi.org/10.1016/j.engstruct.2018.05.050).
- Svanberg, K., 1987. The method of moving asymptotes—a new method for structural optimization. *International Journal for Numerical Methods in Engineering* 24, 359–373. doi:[10.1002/nme.1620240207](https://doi.org/10.1002/nme.1620240207).
- Wallin, M., Jönsson, V., Wingren, E., 2016. Topology optimization based on finite strain plasticity. *Structural and Multidisciplinary Optimization* 54, 783–793. doi:[10.1007/s00158-016-1435-0](https://doi.org/10.1007/s00158-016-1435-0).
- Wang, C., Wang, W., Zhao, W., Wang, Y., Zhou, G., 2018. Structure design and multi-objective optimization of a novel NPR bumper system. *Composites Part B: Engineering* 153, 78–96. doi:[10.1016/j.compositesb.2018.07.024](https://doi.org/10.1016/j.compositesb.2018.07.024).
- Wang, C., Zhao, Z., Zhou, M., Sigmund, O., Zhang, X.S., 2021. A comprehensive review of educational articles on structural and multidisciplinary optimization. *Structural and Multidisciplinary Optimization* 64, 2827–2880. doi:[10.1007/s00158-021-03050-7](https://doi.org/10.1007/s00158-021-03050-7).
- Wang, F., Lazarov, B.S., Sigmund, O., Jensen, J.S., 2014. Interpolation scheme for fictitious domain techniques and topology optimization of finite strain elastic problems. *Computer Methods in Applied Mechanics and Engineering* 276, 453–472. doi:[10.1016/j.cma.2014.03.021](https://doi.org/10.1016/j.cma.2014.03.021).
- Wang, H., Jiang, D.J., Zhang, L.Y., Liu, B., 2017. How to realize volume conservation during finite plastic deformation. *Journal of Applied Mechanics* 84, 111009. doi:[10.1115/1.4037882](https://doi.org/10.1115/1.4037882).

- Wang, H., Xie, H., 2020. Multi-objective optimization of crashworthiness of vehicle front longitudinal beam. *Structural and Multidisciplinary Optimization* 61, 2111–2123. doi:[10.1007/s00158-019-02459-5](https://doi.org/10.1007/s00158-019-02459-5).
- Weber, G., Anand, L., 1990. Finite deformation constitutive equations and a time integration procedure for isotropic, hyperelastic-viscoplastic solids. *Computer Methods in Applied Mechanics and Engineering* 79, 173–202. doi:[10.1016/0045-7825\(90\)90131-5](https://doi.org/10.1016/0045-7825(90)90131-5).
- Wei, C., Liu, L., Cao, H., Zhong, X., Xu, X., Gu, Y., Cheng, D., Huang, Y., Li, Z., Guo, W., Liu, Z., Li, L., 2022. Cu10Sn to Ti6Al4V bonding mechanisms in laser-based powder bed fusion multiple material additive manufacturing with different build strategies. *Additive Manufacturing* 51, 102588. doi:[10.1016/j.addma.2021.102588](https://doi.org/10.1016/j.addma.2021.102588).
- Wei, C., Zhang, Z., Cheng, D., Sun, Z., Zhu, M., Li, L., 2020. An overview of laser-based multiple metallic material additive manufacturing: From macro- to micro-scales. *International Journal of Extreme Manufacturing* 3, 012003. doi:[10.1088/2631-7990/abce04](https://doi.org/10.1088/2631-7990/abce04).
- Wells, G.N., Sluys, L.J., de Borst, R., 2002. A p -adaptive scheme for overcoming volumetric locking during plastic flow. *Computer Methods in Applied Mechanics and Engineering* 191, 3153–3164. doi:[10.1016/S0045-7825\(02\)00252-9](https://doi.org/10.1016/S0045-7825(02)00252-9).
- Wilkins, M.L., et al., 1969. Calculation of elastic-plastic flow. volume 7322. Lawrence Livermore Laboratory, University of California.
- Wright, H.D., Evans, H.R., Harding, P.W., 1987. The use of profiled steel sheeting in floor construction. *Journal of Constructional Steel Research* 7, 279–295. doi:[10.1016/0143-974X\(87\)90003-4](https://doi.org/10.1016/0143-974X(87)90003-4).
- Zhang, G., Li, L., Khandelwal, K., 2017. Topology optimization of structures with anisotropic plastic materials using enhanced assumed strain elements. *Structural and Multidisciplinary Optimization* 55, 1965–1988. doi:[10.1007/s00158-016-1612-1](https://doi.org/10.1007/s00158-016-1612-1).
- Zhang, R., Wang, C., Pan, C., Shen, H., Ge, Q., Zhang, L., 2018. Simplified design of elastoplastic structures with metallic yielding dampers based on the concept of uniform damping ratio. *Engineering Structures* 176, 734–745. doi:[10.1016/j.engstruct.2018.09.009](https://doi.org/10.1016/j.engstruct.2018.09.009).
- Zhang, X., Li, X., Zhang, Y., 2023. A framework for plasticity-based topology optimization of continuum structures. *International Journal for Numerical Methods in Engineering* 124, 1493–1509. doi:[10.1002/nme.7172](https://doi.org/10.1002/nme.7172).
- Zhou, Y., Nomura, T., Saitou, K., 2018. Multi-component topology and material orientation design of composite structures (MTO-C). *Computer Methods in Applied Mechanics and Engineering* 342, 438–457. doi:[10.1016/j.cma.2018.07.039](https://doi.org/10.1016/j.cma.2018.07.039).